POLITECNICO
MILANO 1863

SCUOLA DI INGEGNERIA INDUSTRIALE
E DELL'INFORMAZIONE

Executive Summary of the Thesis

Efficient numerical approximation of parametrized one-way coupled problems in cardiac electromechanics

Laurea Magistrale in Mathematical Engineering - Ingegneria Matematica

Author: Matteo Pierdomenico

Advisor: Prof. Andrea Manzoni

Co-advisor: Dr. Stefano Pagani

Academic year: 2020-2021

1. Introduction

Each heartbeat is an extremely complex multiphysical phenomenon, which combines several different aspects, such as fluid dynamics, biomechanics and electrophysiology [4]. In fact, the main driver of blood ejection in the circulatory system is given by the active ventricular contraction; the heart itself is able to produce the electrical impulse that determines this contraction, starting by a signal, in the form of an electric transmembrane potential, that propagates along all the cardiac muscle tissue. At the macroscopic level, this propagation is mathematically described by a nonlinear reaction-diffusion partial differential equation, suitably coupled to a system of ordinary differential equations. These latter model the ionic currents in the cells, depending on a set of ionic variables, that can be gating variables, indicating the activation of the currents, and/or ionic concentrations.
On the other hand, the contraction mechanism and, more in general, the deformation of the cardiac tissue is modeled by the equations of elastodynamics, with the myocardium usually considered as an orthotropic and hyperelastic material. The orthotropic passive properties of the cardiac tissue are described by strain energy functions of exponential laws, while the active properties depend on the cellular active tension; this latter directly depends on the intracellular calcium concentration released during the electrical propagation.
At the numerical level, the approximation and the simulation of the electrical and mechanical models and, in particular, of their coupling, is a very demanding task, because of nonlinear and multiphysics interactions as well as the different space and time scales of the two problems. Furthermore, when simulating cardiac models, several input data affect the problem under investigation, often varying within a broad range, increasing even more the computational complexity and making the use of high fidelity approximations, such as finite element methods, unfeasible.
In this work, we explore efficient and accurate reduced-order models (ROMs) for the numerical approximation of parametrized problems in cardiac electromechanics. Namely, we rely on reduced basis methods to develop an efficient one-way coupled parametrized electromechanical model, following a global ROM strategy. In particular, we explore several different reduced basis techiniques in the construction of the re-

duced order models, such as the gappy proper orthogonal decomposition (POD) method, able to attain a cost-effective evaluation of the ionic variables in the ROM for cardiac electrophysiology, which is of fundamental importance to to efficiently compute the intracellular calcium concentration and efficiently develop the coupling with the ROM for cardiac mechanics.

2. Core models for cardiac electromechanics

2.1. Cardiac electrophysiology

For cardiac electrophysiology, we consider a three-dimensional monodomain model coupled with the Bueno-Orovio ionic model. The latter is characterized by a system of three ordinary differential equations for the evolution of three different gating variable w_1, w_2, w_3, taking values in $[0,1]$, where the gating variable w_3 can be used as an indication of the intracellular calcium concentration. Let us consider the transmembrane potential $u = u(\mathbf{X},t)$ and the vector of ionic variables $\mathbf{w} = \mathbf{w}(\mathbf{X},t)$ in the reference undeformed domain $\Omega_0 \subset \mathbb{R}^3$ (which can be a portion of the myocardium or the whole left ventricle), the coupled cardiac electrophysiology model yields to the following initial-boundary value problem:

$$\begin{cases} C_m \dfrac{\partial u}{\partial t} - \nabla \cdot (\mathbf{D}\nabla u) + \\ \quad I_{ion}(u, w_1, w_2, w_3) = I_{app}, & in\, \Omega_0 \times (0,T) \\ \dfrac{\partial w_1}{\partial t} = F_{ion,1}(u, w_1), & in\, \Omega_0 \times (0,T) \\ \dfrac{\partial w_2}{\partial t} = F_{ion,2}(u, w_2), & in\, \Omega_0 \times (0,T) \\ \dfrac{\partial w_3}{\partial t} = F_{ion,3}(u, w_3), & in\, \Omega_0 \times (0,T) \\ \dfrac{\partial u}{\partial \mathbf{n}} = 0, & on\, \partial\Omega_0 \times (0,T) \\ u(0) = u_0, \;\; w_1(0) = w_1^0, \\ \quad w_2(0) = w_2^0, \;\; w_3(0) = w_3^0, & in\, \Omega_0 \times \{0\}, \end{cases}$$

where the parameter dependence is due mainly to the variation of the conductivity coefficients, along the principal directions, in the conductivity tensor $\mathbf{D} = \mathbf{D}(\boldsymbol{\mu})$, with $\boldsymbol{\mu} \in \mathcal{P}$; here $\mathcal{P} \subset \mathbb{R}^{N_p}$ denotes the parameters space.

2.2. Cardiac mechanics

In order to exploit the cardiac mechanics model, we consider, together to the reference configuration Ω_0, an actual configuration $\Omega(t)$ at the current time t and we introduce the body transformation map $\boldsymbol{\varphi} : \Omega_0 \to \Omega(t)$ from the reference to the actual configuration, such that $\mathbf{x} = \boldsymbol{\varphi}(\mathbf{X})$ for any $\mathbf{X} \in \Omega_0$, $\mathbf{x} \in \Omega(t)$. Denoting by $\mathbf{d} : \Omega_0 \to \Omega(t)$, $\mathbf{d}(\mathbf{X}) = \boldsymbol{\varphi}(\mathbf{X}) - \mathbf{X}$ the displacement field, the cardiac mechanical model considered yields the following initial-boundary value problem:

$$\begin{cases} \rho \dfrac{\partial^2 \mathbf{d}}{\partial t^2} - \nabla_0 \cdot \mathbf{P}(\mathbf{d}, T_a) = \mathbf{0}, & in\, \Omega_0 \times (0,T) \\ \mathbf{P}(\mathbf{d}, T_a)\mathbf{n} + \mathbf{K}^{epi}\mathbf{d} + \\ \quad \mathbf{C}^{epi} \dfrac{\partial \mathbf{d}}{\partial t} = \mathbf{0}, & on\, \Gamma_0^{epi} \times (0,T) \\ \mathbf{P}(\mathbf{d}, T_a)\mathbf{n} - \\ \quad p(t) J \mathbf{F}^{-T} \mathbf{n} = \mathbf{0}, & on\, \Gamma_0^{endo} \times (0,T) \\ \mathbf{P}(\mathbf{d}, T_a)\mathbf{n} - \\ \quad p(t) \left\| J \mathbf{F}^{-T} \mathbf{n} \right\| \mathbf{v}^{base} = \mathbf{0}, & on\, \Gamma_0^{base} \times (0,T) \\ \mathbf{d} = \mathbf{d}_0, \quad \dfrac{\partial \mathbf{d}}{\partial t} = \dot{\mathbf{d}}_0, & in\, \Omega_0 \times \{0\}, \end{cases}$$

where Γ_0^{epi} represents the epicardial boundary, Γ_0^{endo} the endocardial boundary and Γ_0^{base} the boundary on the truncated part of the cardiac tissue.

To model the Piola-Kirchhof tensor $\mathbf{P} = \mathbf{P}_p + \mathbf{P}_a$, we follow the *active stress* approach, where $\mathbf{P}_p$ is the passive contribute and $\mathbf{P}_a$ is the active contribute. Under the hyperelasticity assumption, the former is obtained from the Guccione strain energy function, while the latter depends on the active tension T_a, which determines the one-way coupling from cardiac electrophysiology to cardiac mechanics. In fact, the active tension solves an activation model that depends on the intracellular calcium concentration coming from the electrical activation. In this work, we consider a trivial activation model, which consists in the following ODE problem:

$$\begin{cases} \dfrac{\partial T_a}{\partial t} = \dfrac{1}{\tau}(T_a^{steady}(w_3, SL) - T_a), & in\, \Omega_0 \times (0,T) \\ T_a = T_{a,0}, & in\, \Omega_0 \times \{0\}, \end{cases}$$

where $T_a = T_a(w_3(\mathbf{X},t))$ evolves in time according to the value of the third ionic variable of the Bueno-Orovio model. In this way, the parameter dependence in the cardiac electromechanics can derive from parameter variations in both cardiac electrophysiology and cardiac

mechanics.
Finally, the pressure on the endocardial boundary, which depends on the blood circulation in the ventricle, is modeled coupling the mechanical problem to a lumped parameters model for closed-loop blood circulation, as in [5].

3. Reduced order modeling

In order to develop the reduced order models of the problems considered, we derived first the full order approximations, by means of a Galerkin finite element method, and then we applied the reduced basis (RB) method to attain more efficient numerical approximations. In fact, the basic idea of any RB method is to approximate the high-fidelity solution of a given problem by means of a (Petrov-)Galerkin projection onto a subspace of much smaller dimension than the one, N_h, of the original full order model (FOM) space. In this way, the resulting computational costs and the required memory storage are much smaller when dealing with a ROM, compared to the FOM.
A RB method can be divided in two phases: an *offline* phase, where the reduced basis functions are computed and stored and the reduced-order arrays are evaluated, and an *online* phase, where the solution of the ROM is determined for each new parameter instance. More specifically, the RB methods adopted in this work relies on proper orthogonal decomposition (POD) to generate a global lower dimensional subspace in which the solution of the ROM problem is sought. The reduced basis, whose vectors are also called POD *modes*, consists of the first $n \ll N_h$ right singular vectors of a snapshot matrix $\mathbf{S}$, which columns are snapshots of the solution of the FOM computed in time and for different parameters. By means of the stored reduced basis, a linear, low dimensional subspace is generated; then a Galerkin (or Petrov-Galerkin) projection is applied to generate the reduced order arrays and, ultimately, the RB problem.
Although the technique is performing extremely well for linear PDEs and in particular when dealing with affinely parametrized operators and data, it is no longer efficient when dealing with nonlinear problems, for which we rely on hyper-reduction techniques, such as the discrete empirical interpolation method (DEIM), to speed up the evaluation of nonlinear arrays in the *online* phase [2, 3, 7].
Moreover, in the *hyper*-ROM for cardiac electrophysiology, we exploit the gappy POD, in order to accurately reconstruct the ionic variables in the original FOM space, starting from their gappy form efficiently obtained in the *online* phase. This has been a fundamental achievement in the construction of the coupled electromechanical ROM, since we adopt the intracellular calcium reconstructed as an input to the activation model for the cardiac mechanics parametrized *hyper*-ROM.
The implementation of the models and the techniques presented in this work have been developed and have contribuited to the extension of the library `pyfe`^{X}, which is a python library binding a C++ high performance finite element library for cardiac simulations and clinical applications, `life`^{x}, developed in the framework of the iHEART project[1].

4. Main results

Here we report the principal results of this work, obtained by simulating the two core supbroblems of cardiac electromechanics on a patient-specific left ventricle, over the time interval $(0, T)$, with $T = 210ms$. This time interval is able to show the depolarization and a part of the repolarization of the transmembrane potential u, as well as the systole for cardiac mechanics, i.e. the contraction of the cardiac muscle in an heartbeat.
In figures 2, 3, 4, 5 we show the evolution in time of the transmembrane potential u and the ionic variables w_1, w_2 and w_3, respectively, comparing the solution obtained by the FOM and the one obtained by the *hyper*-ROM; this latter allows to reach a speedup of more than $3x$ of the latter with respect to the former. Then, in figures 6, 7, 8, 9, we show the main results of the electromechanical parametrized model. In the latter, the active contraction comes from the intracellular calcium concentration, efficiently computed and accurately reconstructed by the Gappy POD method, and we vary parameters affecting the cardiac contraction, comparing the FOM solution to the *hyper*-ROM one. In particular, from figure 6 to figure 9 we show snaphots of the calcium and the displacement under parameter variations at the time steps $35ms$, $70ms$, $140ms$

[1] https://iheart.polimi.it/

and 210ms, respectively. The overall maximum speedup obtained by simulating the electromechanical ROM, so both the electrical and the mechanical ROM subproblems consecutively, has been of almost $3x$ with respect to the FOM, which is a remarkable result in terms of efficiency considering the high-level of accuracy of the reduced order solutions, representing a first step towards the reduction of two-ways coupled problems in cardiac electromechanics.

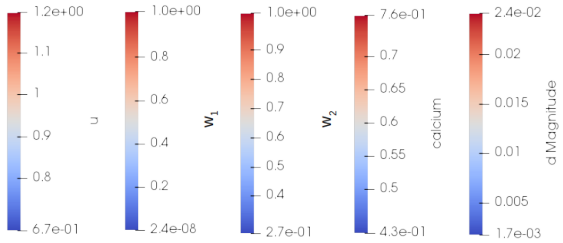

Figure 1: Colormaps for the values of the transmembrane potential, the ionic variables and the displacement field as a reference for the figures that follows.

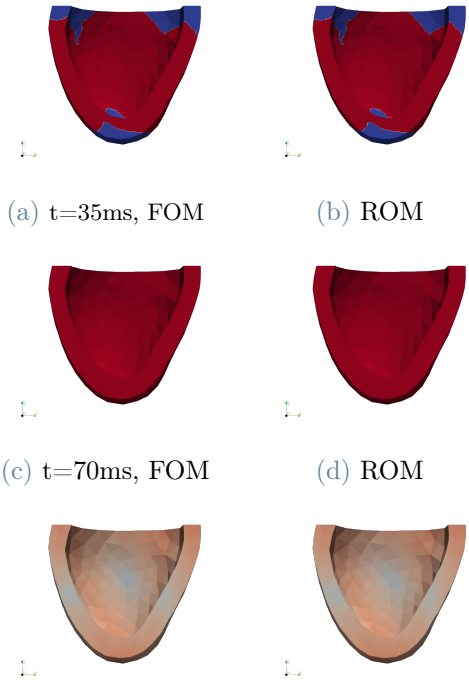

(a) t=35ms, FOM (b) ROM

(c) t=70ms, FOM (d) ROM

(e) t=210ms, FOM (f) ROM

Figure 2: Evolution of the transmembrane potential u in time; comparison between FOM and *online* ROM.

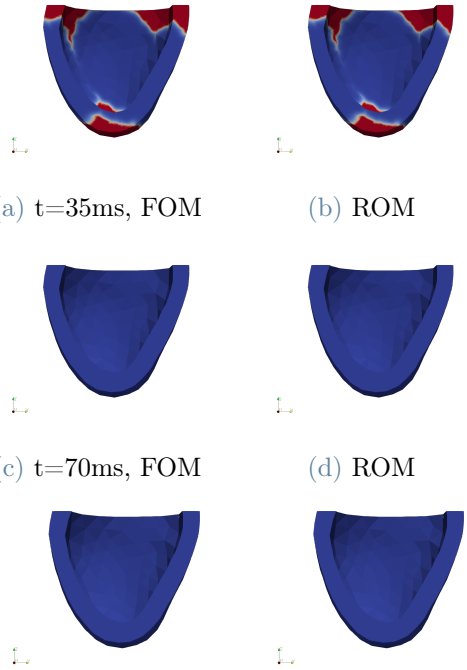

(a) t=35ms, FOM (b) ROM

(c) t=70ms, FOM (d) ROM

(e) t=210ms, FOM (f) ROM

Figure 3: Evolution of the variable w_1 in time; comparison between FOM and *online* ROM.

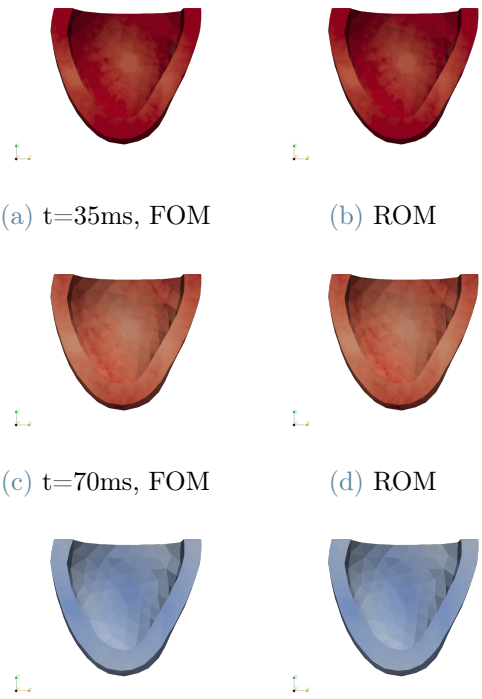

(a) t=35ms, FOM (b) ROM

(c) t=70ms, FOM (d) ROM

(e) t=210ms, FOM (f) ROM

Figure 4: Evolution of the variable w_2 in time; comparison between FOM and *online* ROM.

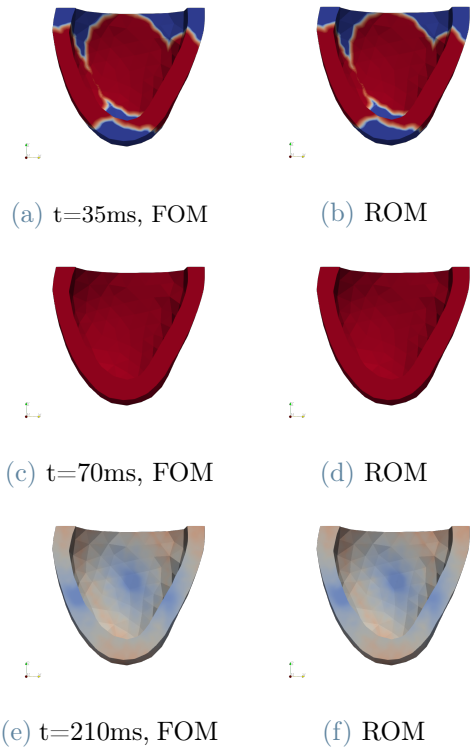

(a) t=35ms, FOM (b) ROM

(c) t=70ms, FOM (d) ROM

(e) t=210ms, FOM (f) ROM

Figure 5: Evolution of the intracellular calcium concentration w_3 in time; comparison between FOM and *online* ROM.

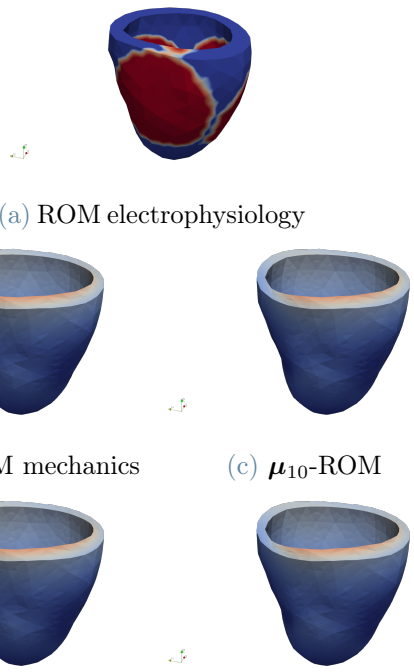

(a) ROM electrophysiology

(b) $\boldsymbol{\mu}_{10}$-FOM mechanics (c) $\boldsymbol{\mu}_{10}$-ROM

(d) $\boldsymbol{\mu}_{14}$-FOM mechanics (e) $\boldsymbol{\mu}_{14}$-ROM

Figure 6: Calcium activation (top) and consequent cardiac deformation at time 35ms. Comparison between FOM and *online* ROM.

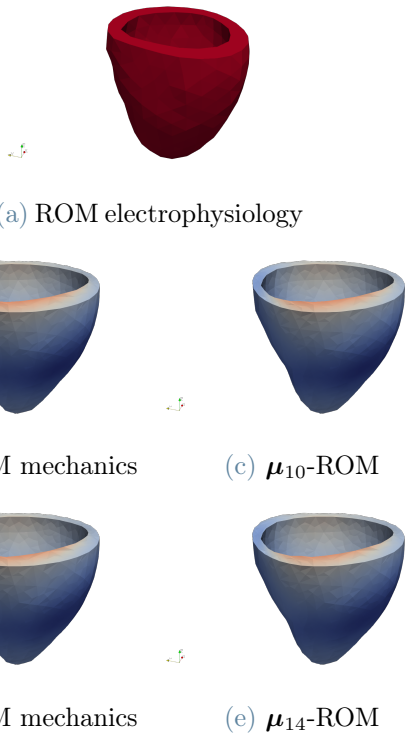

(a) ROM electrophysiology

(b) $\boldsymbol{\mu}_{10}$-FOM mechanics (c) $\boldsymbol{\mu}_{10}$-ROM

(d) $\boldsymbol{\mu}_{14}$-FOM mechanics (e) $\boldsymbol{\mu}_{14}$-ROM

Figure 7: Calcium activation (top) and consequent cardiac deformation at time 70ms. Comparison between FOM and *online* ROM.

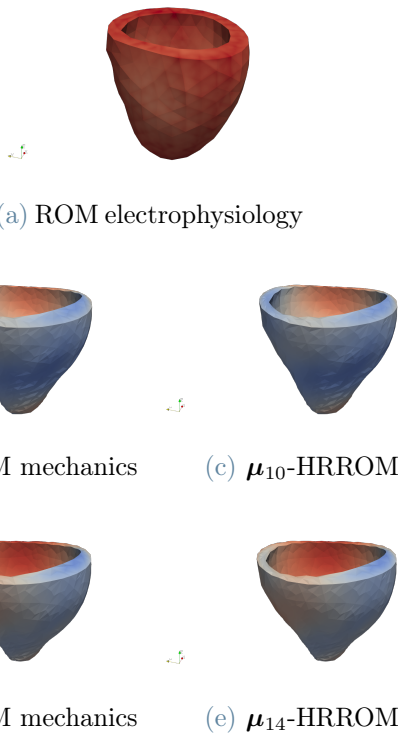

(a) ROM electrophysiology

(b) $\boldsymbol{\mu}_{10}$-FOM mechanics (c) $\boldsymbol{\mu}_{10}$-HRROM

(d) $\boldsymbol{\mu}_{14}$-FOM mechanics (e) $\boldsymbol{\mu}_{14}$-HRROM

Figure 8: Calcium activation (top) and consequent cardiac deformation at time 140ms. Comparison between FOM and *online* ROM.

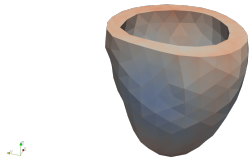

(a) ROM electrophysiology

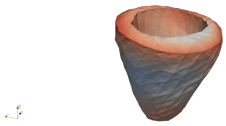

(b) $\boldsymbol{\mu}_{10}$-FOM mechanics

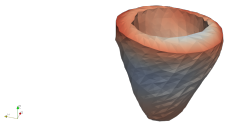

(c) $\boldsymbol{\mu}_{10}$-ROM

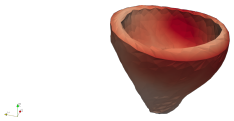

(d) $\boldsymbol{\mu}_{14}$-FOM mechanics

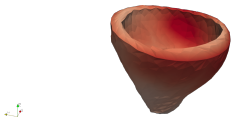

(e) $\boldsymbol{\mu}_{14}$-ROM

Figure 9: Calcium activation (top) and consequent cardiac deformation at time 140ms. Comparison between FOM and *online* ROM.

5. Conclusions

The main achievements of this work have been the exploitment of the gappy proper orthogonal decomposition method to efficiently evaluate the ionic variables in the electrophysiology monodomain problem, and the development of a one-way coupled parametrized electromechanical problem in a reduced order modeling framework, by means of a global ROM strategy. In fact, the cost-effective evaluation of the ionic variables involved in the electrophysiology model represents a fundamental task to couple the ROMs of the core subproblems in cardiac electromechanics, namely the electrical and the mechanical one. In particular, in the latter the active tension, which determines the active contraction of the cardiac muscle, directly depends on the intracellular calcium concentration. Thus, by means of the trivial activation model presented, we managed to couple the electrical propagation to the mechanical contraction. Moreover, the electromechanical model presented in this work is able to efficiently approximate the solutions of its core subproblems under parameters variations and such a result is potentially relevant in clinical applications, where we need to consider the inter-patient variability when modeling the cardiac functions. Possible further extensions of the work can be related to: the use of a local ROM strategy for a more efficient construction of the reduced order models, in particular for cardiac electrophysiology, where the propagating fronts in the solutions affects the efficiency of reduced order modeling when relying on a global ROM strategy; the inclusion of some *mechano-electrical feedbacks* to fully couple the two core subproblems; the generalization to more complete activation models, to reach an even more reliable electromechanical model for real life applications.

References

[1] Carlberg K., Bou-Mosleh C., Farhat C. (2011). *Efficient non-linear model reduction via a least-squares Petrov–Galerkin projection and compressive tensor approximations.* Int. J. Numer. Meth. Engng., 86: 155-181.

[2] Manzoni A., Bonomi D., Quarteroni A. (2018). *Reduced Order Modeling for Cardiac Electrophysiology and Mechanics: New Methodologies, Challenges and Perspectives.* In Mathematical and Numerical Modeling of the Cardiovascular System and Applications (pp. 115-166). Springer, Cham.

[3] Pagani S., Manzoni A., Quarteroni A. (2018). *Numerical approximation of parametrized problems in cardiac electrophysiology by a local reduced basis method.*

[4] Quarteroni A., Dede' L., Manzoni A., Vergara C. (2019). *Mathematical Modelling of the Human Cardiovascular System: Data, Numerical Approximation, Clinical Applications.* Cambridge: Cambridge University Press.

[5] Regazzoni F., Salvador M., Africa P.c., Fedele M., Dede' L., Quarteroni A. (2020). *A cardiac electromechanics model coupled with a lumped parameters model for closed-loop blood circulation. Part I: model derivation.* ArXiv preprint arXiv:2011.15040 Computer Methods in Applied Mechanics and Engineering, 340, 530-558.

[6] Colli Franzone P., Pavarino L.F., Scacchi S. (2015). *Parallel multilevel solvers for the cardiac electromechanical coupling.* Appl. Numer. Math. 95, 140–153.

[7] Quarteroni A, Manzoni A, Negri F. (2015) *Reduced basis methods for partial differential equations: an introduction.* Vol. 92. Springer.

POLITECNICO
MILANO 1863

SCUOLA DI INGEGNERIA INDUSTRIALE
E DELL'INFORMAZIONE

Efficient numerical approximation of parametrized one-way coupled problems in cardiac electromechanics

Tesi di Laurea Magistrale in
Mathematical Engineering - Ingegneria Matematica

Author: **Matteo Pierdomenico**

Student ID: 919958
Advisor: Prof. Andrea Manzoni
Co-advisors: Dr. Stefano Pagani
Academic Year: 2020-21

Abstract

Reduced-order modeling techniques are of fundamental importance when dealing with the numerical approximation of partial differential equations characterized by nonlinearity or high sensitivity to parameter variation, such as the ones arising from cardiac electromechanics. In this work, we present an efficient numerical approximation of both cardiac electrophysiology and cardiac mechanics, developing a one-way electromechanical coupling in the reduced-order model framework, where the electrical propagation activates cardiac contraction. In particular, we develop an efficient evaluation of the ionic variables in the cardiac electrophysiology monodomain model, exploiting the gappy proper orthogonal decomposition (POD) method, coupling the two core subproblems by means of a phenomenological activation model for cardiac mechanics, that takes as an input the efficiently computed intracellular calcium concentration to evaluate the active tension that determines the active cardiac concraction. In this way, the electromechanical reduced-order model presented is capable to approximate the solutions under parameter variations from both the cardiac electrophysiology subproblem and the cardiac mechanics subproblem. Moreover, a secondary achievement of this work consists in the investigation of the performance of a least-squares Petrov-Galerkin projection approach in terms of efficiency and accuracy of a reduced-order model for the cardiac electrophysiology problem. Numerical results assessing the accuracy and the efficiency of the proposed strategies deal with the simulation of electrophysiology and one-way coupled electromechanics problems on a patient-specific left ventricle geometry.

Keywords: Nonlinear PDEs; Cardiac electromechanics; Coupled problems; Reduced-order models; Proper orthogonal decomposition (POD); Gappy POD.

Estratto

Le tecniche di modellazione di ordine ridotto sono di fondamentale importanza quando si tratta l'approssimazione numerica di problemi caratterizzati da nonlinearità e sensibilità alla variazione dei parametri considerati, come quelli che riguardano l'elettromeccanica cardiaca. Nel seguente elaborato presentiamo un' approssimazione numerica efficiente dei problemi di elettrofisiologia e meccanica cardiaca, sviluppando, nel contesto dei modelli di ordine ridotto, un modello elettromeccanico accoppiato unidirezionalmente, nel quale la propagazione elettrica attiva la contrazione meccanica. In particolare, esploriamo il metodo gappy proper orthogonal decomposition (POD) per il calcolo efficiente delle variabili ioniche nel modello del monodominio per l'elettrofisiologia e sviluppiamo l'accoppiamento tramite un modello di attivazione fenomenologico per la meccanica cardiaca, in grado di ottenere la tensione che determina la contrazione attiva delle fibre del muscolo cardiaco attraverso il valore del calcio intracellulare, ottenuto dall'elettrofisiologia. In questo modo, il modello di ordine ridotto elettromeccanico presentato è in grado di ottenere approssimazioni accurate delle soluzioni, tenendo conto di variazioni dei parametri sia dal sottoproblema elettrofisiologico che da quello meccanico. Inoltre, come risultato secondario, in questo lavoro abbiamo investigato la performance dell'uso di una proiezione ai minimi quadrati Petrov-Galerkin in termini di accuratezza ed efficienza nella costruzione del modello di ordine ridotto relativo all'elettrofisiologia. I risultati numerici che valutano l'accuratezza e l'efficienza dei metodi proposti riguardano la simulazione dei problemi di elettrofisiologia e elettromeccanica accoppiata unidirezionalmente su una geometria di ventricolo sinistro che si attiene a quella reale.

Parole chiave: EDPi nonlineari; Elettromeccanica cardiaca; Problemi accoppiati; Modelli di ordine ridotto; Proper orthogonal decomposition (POD); Gappy POD.

Contents

Introduction

Each heartbeat is a very complex multiphysical phenomenon, which combines several different aspects, such as fluid dynamics, biomechanics and electrophysiology [35]. In fact, the main driver of blood ejection in the circulatory system is given by the active ventricular contraction. The heart itself is able to produce the electrical impulse that determines this contraction, starting by a signal, in the form of an electric transmembrane potential, that propagates along all the myocardium, the cardiac muscle tissue.
The evolution of the transmembrane potential is generated at the cell level by several ion channels that open and close repeatedly. This gives rise to currents passing through the cell membrane, that determine depolarization and repolarization phases characterizing each heartbeat. At the macroscopic level, this propagation is mathematically described by a nonlinear reaction-diffusion partial differential equation suitably coupled to a system of ordinary differential equations, which model the ionic currents in the cells, depending on a set of ionic variables, that can be gating variables, indicating the activation of the currents, and/or ionic concentrations.
The more commonly used models to study the transmembrane potential dynamic are the bidomain and the monodomain models [3, 36–38]. The former considers the cardiac tissue as a syncytium made by intracellular and extracellular domains coexisting at each point of the tissue. It is the most complete mathematical model for describing the electrical signal propagation in the heart, however it is the most computationally demanding. On the other hand, the latter is a simpler version, which considers intra and extracellular domains to have equal anisotropy ratios, reducing thus the number of partial differential equations considered with respect to the bidomain model and, as a consequence, reducing the computational costs. The monodomain model is not suitable for the description of a wide range of pathological situations as the former one, yet it is able to accurately describe the cardiac tissue in physiological situations. Since the aim of this work is the efficient evaluation of the ionic variables to develop an electromechanical coupling [3, 5] in the cardiac left ventricular tissue under physiological conditions, we will rely on the monodomain model.

Specifically, we will exploit a one-way electromechanical coupling, where the mechanical activation depends on the intracellular calcium concentration released during electrical activation. In fact, the intracellular calcium concentration is the main responsible of the

cardiac muscle contraction and couples the electrical and mechanical phenomena of the heartbeat, since it is an input of the active tension model, which describes the generation of active force within each myocyte [31, 34]. The deformation of the cardiac tissue is then modeled by the equations of elastodynamics, with the myocardium being an orthotropic and hyperelastic material. The orthotropic passive properties of the cardiac tissue are described by strain energy functions of exponential laws [17, 18, 30], while the active properties depend on the cellular active tension.
At the numerical level, the approximation and simulation of cardiac electromechanics is a very demanding and expensive task, because of the very different space and time scales associated with the electrical and mechanical models, as well as their nonlinear and multiphysics interactions. In fact, to correctly track the wave-front solution representing the propagation of the transmembrane potential in cardiac electrophysiology, fine computational grids are needed, thus leading to a very large-scale algebraic problem to be solved. Moreover, to describe the mechanics of the cardiac tissue we need to rely on complex constitutive laws, resulting in a complex highly nonlinear model. This turns into the need of assembling involved Jacobian matrices when relying, e.g., on the Newton method for the solution of nonlinear systems of equations.
Furthermore, when simulating cardiac models, several input data affect the problem under investigation, often varying within a broad range and possibly affected by uncertainty. Since it is of fundamental importance to address the impact of input variations on output quantities of interest, in order to obtain reliable results and calibrate the numerical solvers, several numerical simulations have to be carried out, increasing even more the computational complexity and making unfeasible the use of high fidelity approximations obtained by applying, e.g., finite element methods. The need of solving these problems efficiently calls for the development of efficient and accurate reduced-order modeling techniques in electromechanics.

Reduced basis (RB) methods and, more generally, reduced-order models (ROMs), have been extensively investigated in the last decades. The basic idea of any RB method is to approximate the high-fidelity solution of a given problem by means of a (Petrov-)Galerkin projection onto a subspace of much smaller dimension than the one, N_h, of the original FOM space. In this way, the resulting computational costs and the required memory storage are much smaller when dealing with a ROM, compared to the FOM. A RB method can be divided in two phases: an *offline* phase, where the reduced basis functions are computed and stored and the reduced-order arrays are evaluated, and an *online* phase, where the solution of the ROM is determined for each new parameter instance. More specifically, the RB method can rely on proper orthogonal decomposition (POD) to generate a global low dimensional subspace in which the solution of the ROM problem is sought. The reduced basis, whose vectors are also called POD *modes*, consists of the first

$n \ll N_h$ right singular vectors of a snapshot matrix $\mathbf{S}$ collecting the solution of the FOM computed following different criteria, such as time instants and/or different parameters for parametrized problems. By means of the stored reduced basis, a linear, low dimensional subspace is generated; then a Galerkin (or Petrov-Galerkin) projection is applied to generate the reduced-order arrays and, ultimately, the RB problem. Although the technique shows good performance in terms of efficiency for linear PDEs and, in particular, when dealing with affinely parametrized operators and data, it is no longer efficient when dealing with nonlinear problems, unless hyper-reduction techniques (such as the discrete empirical interpolation method (DEIM) or the gappy proper orthogonal decomposition) are applied to speed up the evaluation of nonlinear arrays in the *offline* phase, see [1, 3, 8].

In order to develop an efficient one way electromechanical coupling, in this work we exploit the gappy proper orthogonal composition to compute and extrapolate the evolution of the intracellular calcium, in each point of the domain, from the ROM for cardiac electrophysiology and we apply it in a simple, phenomenological activation model based on the solution of the Hill equation [33, 34], which consists in ordinary differential equation, solved at each point of the domain, to compute the evolution in time of the active tension responsible to the active ventricular tissue contraction in the cardiac mechanical reduced-order model.
The main achievements of this thesis are related with the efficient and accurate evaluation of ionic variables in a parametrized cardiac electrophysiology problem and the development of an efficient coupling between cardiac electrophysiology and cardiac mechanics. In particular, in the framework of reduced-order modeling, we built an efficient numerical approximation of the electromechanical problem, which is able to account the effects of parameter variations to the solutions. In fact, the model has been implemented in such a way it can consider variations of parameters in both cardiac electrophysiology and cardiac mechanics, to also understand how the former influences the latter. In this work, in particular, we show the results of the electromechanical coupling for a parametrization coming from the mechanical subproblem, where there are several parameters of interest in clinical applications such as, e.g., the Bulk modulus, that regulates the compressibility of the cardiac tissue.

The implementation of the models and the techniques presented in this thesis have been developed and have contribuited to the extension of the library `pyfe`^{X}, which is a python library for efficient numerical cardiac simulations and clinical applications, binding a C++ high performance finite element library, `life`^{x}, developed in the framework of the iHEART project[1].

[1] http://iheart.polimi.it

The structure of the thesis is as follows:

- in the first chapter we introduce the core mathematical models for cardiac electrophysiology and cardiac mechanics adopted in this work;
- in the second chapter we present the numerical approximation of the core models by full-order modeling, using a Galerkin-finite element method;
- in the third chapter we develop an efficient numerical approximation by reduced-order modeling of the parametrized problems considered, in particular we present the RB techniques applied to efficiently compute the ionic variables, the potential and the displacement field;
- in the fourth chapter we present the numerical results related to the ROM for cardiac electrophysiology, with a particular attention to the efficient computation of the ionic variable by the Gappy POD method and to the effects of parameter variations;
- in the fifth chapter we present the numerical results related to the electromechanical reduced-order model, looking at efficiency and accuracy under the variation of parameters involved in the cardiac mechanics.

1 | Mathematical Models for cardiac electromechanics

In this chapter we present an overview of the electromechanics mathematical models. We consider the monodomain model for cardiac electrophysiology, the so-called minimal Bueno-Orovio model as ionic model (to describe ionic concentrations, such as sodium and calcium), and the hyperelastic Guccione model for the passive ventricular mechanics, adopting an active-stress formulation to take into account active mechanics. This latter requires the introduction of a dynamical system which describes fibers shortening as a function of the calcium concentration.

1.1. Cardiac electrophysiology

To characterize the evolution of the transmembrane potential we rely on the monodomain model, which is a reduced version of the bidomain model. Both models have been widely used in the last decades to study cardiac electrophysiology [39, 40], arising from a homogenization process applied to the cardiac tissue. These continuous models describe the spreading of the signal in the heart tissue and are usually coupled to a ionic model which describes the evolution of ion concentrations and the ionic currents inside the cells. In this work, as ionic model we will consider the Bueno-Orovio ionic model and we couple it to the monodomain equation.

1.1.1. The monodomain model

Let us consider the transmembrane potential $u = u(\mathbf{X}, t)$ coupled with a ionic model depending on a set of ionic variables $\mathbf{w} = \mathbf{w}(\mathbf{X}, t)$, in a Lipschitz domain Ω_0 in $\mathbb{R}^3$, which can be a portion of the myocardium or the whole left ventricle, where $\mathbf{X} \in \Omega_0$ denotes a coordinate in the reference configuration.

The monodomain model yields the following initial-boundary value problem:

$$\begin{cases} C_m \dfrac{\partial u}{\partial t} - \nabla \cdot (\mathbf{D}\nabla u) + I_{ion}(u, \mathbf{w}) = I_{app}(\mathbf{X}; t), & \mathbf{X} \in \Omega_0, \quad t \in (0, T) \\ \dfrac{\partial \mathbf{w}}{\partial t} = \mathbf{F}_{ion}(u, \mathbf{w}), & \mathbf{X} \in \Omega_0, \quad t \in (0, T) \\ \dfrac{\partial u}{\partial \mathbf{n}} = 0, & \mathbf{X} \in \partial\Omega_0, \quad t \in (0, T) \\ u(\mathbf{X}, 0) = u_0 \quad \mathbf{w}(\mathbf{X}, 0) = \mathbf{w}_0, & \mathbf{X} \in \Omega_0, \end{cases} \tag{1.1}$$

where the Neumann boundary conditions express the fact that the cardiac tissue is electrically insulated. Here, C_m is the transmembrane capacitance, $I_{ion}(u, \mathbf{w})$ is the sum of the current densities through the membrane, $I_{app} = I_{app}(\mathbf{x}, t)$ is an external applied current density representing the initial activation of the tissue, $\mathbf{D}$ is the (positive definite) conductivity tensor, that depends on the fibers-sheet structure of the tissue, t is a rescaled time and $\mathbf{n}$ denotes the outward unit normal vector to the boundary $\partial\Omega_0$. Both I_{ion} and $\mathbf{F}_{ion}$ depend on u and $\mathbf{w}$, thus making the PDE and the ODEs two ways coupled.
The characterization of the functions I_{ion} and $\mathbf{F}_{ion}$, and the number of functions $\mathbf{F}_{ion}$, i.e. the number of ionic variables, depend on the considered ionic model. There exist several ionic models in order to accurately describe the evolution of the transmembrane potential and the regulation of the ionic fluxes thorugh the membrane. The ionic model adopted for this work is the Bueno-Orovio model, which is described in the next section.

1.1.2. Bueno-Orovio model

The Bueno-Orovio model, also called minimal model, is characterized by a system of three ordinary differential equations for the evolution of three different gating variable w_1, w_2, w_3, taking values in $[0, 1]$, where the first two gating variables represent the portion of open channels on the membrane, while the gating variable w_3, which also takes values in $[0, 1]$, can be used as an indication of the intracellular calcium concentration. The coupled monodomain Bueno-Orovio system reads as follows:

$$\begin{cases} C_m \dfrac{\partial u}{\partial t} - \nabla \cdot (\mathbf{D}\nabla u) + I_{ion}(u, w_1, w_2, w_3) = I_{app}, & in \ \ \Omega_0 \times (0, T) \\ \dfrac{\partial w_1}{\partial t} = F_{ion,1}(u, w_1), & in \ \ \Omega_0 \times (0, T) \\ \dfrac{\partial w_2}{\partial t} = F_{ion,2}(u, w_2), & in \ \ \Omega_0 \times (0, T) \\ \dfrac{\partial w_3}{\partial t} = F_{ion,3}(u, w_3), & in \ \ \Omega_0 \times (0, T) \\ \dfrac{\partial u}{\partial \mathbf{n}} = 0, & on \ \ \partial\Omega_0 \times (0, T) \\ u(0) = u_0, \quad w_1(0) = w_1^0, \quad w_2(0) = w_2^0, \quad w_3(0) = w_3^0, & in \ \ \Omega_0, \end{cases} \tag{1.2}$$

where

$$F_{ion,1}(u,w_1) = [1-H(u-\theta_{w_1})]\frac{w_{1,\infty}-w_1}{\tau^-_{w_1}} - H(u-\theta_{w_1})\frac{w_1}{\tau^+_{w_1}},$$
$$F_{ion,2}(u,w_2) = [1-H(u-\theta_{w_2})]\frac{w_{2,\infty}-w_2}{\tau^-_{w_2}} - H(u-\theta_{w_2})\frac{w_2}{\tau^+_{w_2}},$$
$$F_{ion,3}(u,w_3) = \frac{[1+tanh(k_{w_3}(u-u_{w_3}))]/2 - w_3}{\tau_{w_3}},$$

while $I_{ion}(u,w_1,w_2,w_3)$ is the sum of three currents, $I_{ion}(u,w_1,w_2,w_3) = I_{fi}(u,w_1) + I_{so}(u) + I_{si}(u,w_2,w_3)$, defined as follows:

$$I_{fi}(u,w_1) = w_1\frac{(u-\theta_{w_1})(c_u-u)H(u-\theta_{w_1})}{\tau_{fi}},$$
$$I_{so}(u) = \frac{(u-u_0)(1-H(u-\theta_{w_2}))}{\tau_0} + \frac{H(u-\theta_{w_2})}{\tau_{so}},$$
$$I_{si}(u,w_2,w_3) = w_2w_3\frac{H(u-\theta_{w_2})}{\tau_{si}},$$

which represent the fast inward, the overall slow outward and the slow inward currents, respectively. Here $H(\cdot)$ denotes the Heaviside function.
Some of the constants of the model are deduced by the following formulas:

$$\tau^-_{w_1} = (1-H(u-\theta^-_{w_1}))\tau^-_{w_1,1} + H(u-\theta^-_{w_1})\tau^-_{w_1,2},$$
$$\tau^-_{w_2} = \tau^-_{w_2,1} + (\tau^-_{w_2,2}-\tau^-_{w_2,1})(1+tanh(k^-_{w_2}(u-u^-_{w_2})))/2,$$
$$\tau_{so} = \tau_{so,1} + (\tau_{so,2}-\tau_{so,1})(1+tanh(k_{so}(u-u_{so})))/2,$$
$$\tau_{w_3} = (1-H(u-\theta_{w_2}))\tau_{w_3,1} + H(u-\theta_{w_2})\tau_{w_3,2},$$
$$\tau_0 = (1-H(u-\theta_0))\tau_{0,1} + H(u-\theta_0)\tau_{0,2},$$
$$w_{1,\infty} = 1-H(u-\theta^-_{w_1}),$$
$$w_{2,\infty} = (1-H(u-\theta_0))\Big(1-\frac{u}{\tau_{w_{2,\infty}}}\Big) + H(u-\theta_0)w^*_{2,\infty}.$$

The model parameters, see appendix A, allow to reproduce the action potential morphologies, see, e.g., [2], and can be fitted to replicate accurately the dynamics of more complex ionic models as well as experimental data, such as action potential duration and conduction velocity restitution curve, upstroke velocities, thresholds for excitation, minimum action-potential durations and diastolic intervals before reaching conduction block. For instance, the conductivity tensor $\mathbf{D} = \mathbf{D}(\mathbf{X}) \in \mathbb{R}^3$ models the anisotropy of the cardiac tissue, characterized by a higher conductivity in the fiber direction, and can be

expressed as:

$$\mathbf{D}(\mathbf{X}) = z\sigma_m^t \mathbf{I} + z(\sigma_m^l - \sigma_m^t)\mathbf{f}_0 \otimes \mathbf{f}_0 + (\sigma_m^n - \sigma_m^t)\mathbf{n}_0 \otimes \mathbf{n}_0,$$ [1]

where σ_m^l, σ_m^t and σ_m^n are electrical conductivity coefficients along the fibers, the transversal and the normal directions respectively. Namely, here, $\mathbf{f}_0$ is the fibers direction, $\mathbf{n}_0$ is the normal direction and $\mathbf{I}$ is the identity matrix. As input parameters, then, we consider the conductivity coefficients described above and the parameters which describe the external applied current I_{app}. Finally, the initial data for the ionic variable are $w_1^0 = 1$, $w_2^0 = 1$, $w_3^0 = 0$, while the initial potential is $u_0 = 0$.

1.2. Cardiac mechanics

The description of cardiac mechanics involves both a passive and an active contribution. In fact, the active contraction of the muscular fibers has to be included in the force balance when modeling the systolic part of the cardiac cycle.

In order to exploit the cardiac mechanics model, we consider a reference configuration Ω_0 and an actual configuration $\Omega(t)$ at the current time t. We denote by $\mathbf{X}$ the spatial variable in Ω_0 and by $\mathbf{x}$ the spatial variable in $\Omega(t)$. It is possible to introduce the body transformation as the map $\boldsymbol{\varphi} : \Omega_0 \to \Omega(t)$ from the reference to the actual configuration, such that $\mathbf{x} = \boldsymbol{\varphi}(\mathbf{X})$ for any $\mathbf{X} \in \Omega_0$, $\mathbf{x} \in \Omega(t)$. The deformation gradient tensor F is defined as:

$$\mathbf{F} = \frac{\partial \boldsymbol{\varphi}}{\partial \mathbf{X}}, \qquad [F_{i,j}] = \frac{\partial \varphi_i}{\partial X_j}, \quad i, j = 1, 2, 3. \tag{1.3}$$

By denoting $\mathbf{d} : \Omega_0 \to \Omega(t)$, $\mathbf{d}(\mathbf{X}) = \boldsymbol{\varphi}(\mathbf{X}) - \mathbf{X}$ the displacement field, the deformation gradient tensor $\mathbf{F}$ can be written as $\mathbf{F} = \mathbf{I} + \mathbf{d}$. Moreover, we denote by $J = det(\mathbf{F})$ the determinant of the deformation gradient tensor $\mathbf{F}$ and by $\mathbf{C} = \mathbf{F}^T\mathbf{F}$ the left Cauchy-Green strain tensor.

In order to model the active mechanics, the two paradigms commonly used are the *active stress* and the *active strain* approaches, see [3, 20] . Both strategies allow to couple electrophysiology and mechanics, defining a modified first Piola-Kirchhoff tensor $\mathbf{P}$ which involves a passive and an active component. The former describes the stress required to obtain a given deformation of the passive myocardium; the latter is responisble of the tension generated by the depolarization of the propagating electrical signal, that provides internal active forces responsible for the contraction. In this work, the *active*

[1] The parameter z is a specific parameter set in order to simulate ischemic regions. However, in the physiological case, as the one considered, it is set to $z = 1$.

stress approach has been considered, namely we write the first Piola-Kirchhof tensor as follows:

$$\mathbf{P} = \mathbf{P}_p + \mathbf{P}_a, \tag{1.4}$$

where $\mathbf{P}_p$ is the passive contribute and $\mathbf{P}_a$ is the active contribute to the Piola-Kirchhoff tensor.

1.2.1. Passive mechanics

The cardiac mechanical response, similarly to the the electrical propagation, is highly dependent on the presence of fibers and sheets. For this reason, the passive myocardium is modeled as an orthotropic, hyperelastic material.
The equations of motion for the cardiac tissue express the balance of linear momentum in material coordinates, which reads as

$$\rho \frac{\partial^2 \mathbf{d}}{\partial t^2} - \nabla_0 \cdot \mathbf{P}_p(\mathbf{d}) = \mathbf{b}_0, \tag{1.5}$$

where ρ is the tissue density and $\mathbf{b}_0$ are the body forces. Here, $\mathbf{P}_p$ is the first (passive) Piola-Kirchhoff tensor, which is related to the surface tractions on the reference configutation.
We impose Neumann boundary conditions on the endocardium ($\Gamma_N = \Gamma^{endo}$) to model the effect of blood pressure, and Robin boundary conditions on the epicardium and on the base ($\Gamma_R = \Gamma^{epi} \cup \Gamma^{base}$). We also neglect the body forces $\mathbf{b}_0$ because their contribution is negligible [29]. Finally, in a Lagrangian framework, the cardiac deformation under passive mechanics written in the reference configuration solve the following initial-boundary value problem:

$$\begin{cases} \rho \dfrac{\partial^2 \mathbf{d}}{\partial t^2} - \nabla_0 \cdot \mathbf{P}_p(\mathbf{d}) = \mathbf{0}, & in \quad \Omega_0 \times (0,T) \\ \mathbf{P}_p(\mathbf{d})\mathbf{n} + \mathbf{K}^{epi}\mathbf{d} + \mathbf{C}^{epi}\dfrac{\partial \mathbf{d}}{\partial t} = \mathbf{0}, & on \quad \Gamma_0^{epi} \times (0,T) \\ \mathbf{P}_p(\mathbf{d})\mathbf{n} - p(t) J\mathbf{F}^{-T}\mathbf{n} = \mathbf{0}, & on \quad \Gamma_0^{endo} \times (0,T) \\ \mathbf{P}_p(\mathbf{d})\mathbf{n} - p(t) \left\| J\mathbf{F}^{-T}\mathbf{n} \right\| \mathbf{v}^{base} = \mathbf{0}, & on \quad \Gamma_0^{base} \times (0,T) \\ \mathbf{d} = \mathbf{d}_0, \quad \dfrac{\partial \mathbf{d}}{\partial t} = \dot{\mathbf{d}}_0, & in \quad \Omega_0 \times \{0\}, \end{cases} \tag{1.6}$$

where $\mathbf{n}$ is the outward normal to Ω_0 and the initial conditions are set to $\mathbf{d}_0 = 0$ and $\dot{\mathbf{d}}_0 = 0$. Under the hyperelasticity assumption, once the strain energy function $\mathcal{W} : \Omega_0 \to \mathbb{R}$ is introduced, the passive part of the Piola-Kirchhoff tensor reads as

$$\mathbf{P}_p = \frac{\partial \mathcal{W}}{\partial \mathbf{F}}.$$

Several models have been proposed in literature to describe the orthotropic nature of the cardiac muscle tissue. In this work, the Guccione strain energy function is considered

[17, 18], for which

$$\mathcal{W}(\mathbf{F}) = \frac{c}{2}(e^Q - 1) + \mathcal{W}_{vol}(J), \tag{1.7}$$

with

$$Q = b_{ff}E_{ff}^2 + b_{ss}E_{ss}^2 + b_{nn}E_{nn}^2 + b_{fs}(E_{fs}^2 + E_{sf}^2) + b_{fn}(E_{fn}^2 + E_{nf}^2) + b_{sn}(E_{sn}^2 + E_{ns}^2), \tag{1.8}$$

where $E_{ab} = \mathbf{E}\mathbf{a}_0\mathbf{b}_0$, for $a, b \in \{f, s, n\}$, the principal directions in the reference configuration, are the entries of $\mathbf{E} = \frac{1}{2}(\mathbf{C} - \mathbf{I})$, i.e. of the Green-Lagrange strain energy tensor. We consider a further term, defined as

$$\mathcal{W}_{vol}(J) = \frac{B}{2}(J - 1), \tag{1.9}$$

convex in J, with $J = 1$ as a global minimum, which penalizes large volume variations, thus obtaining the model a weakly incompressible material; $B \in \mathbb{R}^+$ represents the bulk modulus. Further details regarding the parameters of the model are reported in the appendix A.

1.2.2. Active mechanics

The electrical activation of the cardiomyocytes in the cardiac muscle is responsible of their contraction, without the need of an external impulse. This behavior can be modeled by including the active contraction of the muscular fibers in the force balance (1.6). In particular, the active component $\mathbf{P}_a$ of the first Piola-Kirchhoff tensor $\mathbf{P}$ denotes the tension generated by the depolarization of the propagating electrical signal, that provides the internal active forces leading to the contraction. We can express $\mathbf{P}_a$ as

$$\mathbf{P}_a = T_a \frac{\mathbf{F}\mathbf{f}_0 \otimes \mathbf{f}_0}{\sqrt{\mathcal{I}_{4f}}},$$

where $\mathcal{I}_{4f} = \mathbf{F}\mathbf{f}_0 \cdot \mathbf{F}\mathbf{f}_0$ is a measure of the tissue stretch along the fibers direction [25], while $T_a = T_a(\mathbf{X}, t)$ denotes the active tension, which is mainly regulated by the intracellular calcium ions concentration ($[Ca^{2+}]_i$) and the sarcomere length (SL) [31]. In this work, to describe the evolution of the active tension T_a in time, we consider a phenomenological activation model:

$$\begin{cases} \dfrac{\partial T_a}{\partial t} = A([Ca^{2+}]_i, T_a) = \dfrac{1}{\tau}(T_a^{steady}([Ca^{2+}]_i, SL) - T_a), & in\ \ \Omega_0 \times (0, T) \\ T_a = T_{a,0}, & in\ \ \Omega \times \{0\}, \end{cases} \tag{1.10}$$

where T_a depends on space and time by the intracellular calcium concentration spreading in the cardiac muscle, namely $T_a = T_a([Ca^{2+}])$, $T_{a,0} = 0$ and $T_a^{steady}([Ca^{2+}]_i, SL)$ denotes the steady-state active tension, representing a force-calcium relationship well described

by the Hill equation [32–34]:

$$T_a^{steady}([Ca^{2+}]_i, SL) = \frac{T_a^{max}}{1 + \left(\frac{EC_{50}}{[Ca^{2+}]_i}\right)^{n_H}}. \tag{1.11}$$

In (1.11), T_a^{max} is the maximum tension, EC_{50} is the half maximal effective concentration and n_H is the Hill coefficient.
Through the active mechanics contribution, Eq. (1.6) thus becomes:

$$\begin{cases} \rho\dfrac{\partial^2 \mathbf{d}}{\partial t^2} - \nabla_0 \cdot \mathbf{P}(\mathbf{d}, T_a) = \mathbf{0}, & in \quad \Omega_0 \times (0,T) \\ \mathbf{P}(\mathbf{d}, T_a)\mathbf{n} + \mathbf{K}^{epi}\mathbf{d} + \mathbf{C}^{epi}\dfrac{\partial \mathbf{d}}{\partial t} = \mathbf{0}, & on \quad \Gamma_0^{epi} \times (0,T) \\ \mathbf{P}(\mathbf{d}, T_a)\mathbf{n} - p(t)J\mathbf{F}^{-T}\mathbf{n} = \mathbf{0}, & on \quad \Gamma_0^{endo} \times (0,T) \\ \mathbf{P}(\mathbf{d}, T_a)\mathbf{n} - p(t)\left\|J\mathbf{F}^{-T}\mathbf{n}\right\|\mathbf{v}^{base} = \mathbf{0}, & on \quad \Gamma_0^{base} \times (0,T) \\ \mathbf{d} = \mathbf{d}_0, \quad \dfrac{\partial \mathbf{d}}{\partial t} = \dot{\mathbf{d}}_0, & in \quad \Omega_0 \times \{0\}, \end{cases} \tag{1.12}$$

where we have now highlighted the fact that the electrical potential affects cardiac deformations, thus requiring a coupled electromechanical problem to fully understand the behavior of the heart muscular tissue during each heartbeat.
Looking in more detail to the boundary conditions, we have that, on the epicardial boundary Γ_0^{epi}, the generalized Robin boundary condition models the interaction of the left ventricle with pericardium [24], namely, in $(1.12)_2$, we define the following tensors

$$\begin{aligned} \mathbf{K}^{epi} &= K_{\perp}^{epi}(\mathbf{n}\otimes\mathbf{n}) + K_{\parallel}^{epi}(\mathbf{I} - \mathbf{n}\otimes\mathbf{n}), \\ \mathbf{C}^{epi} &= C_{\perp}^{epi}(\mathbf{n}\otimes\mathbf{n}) + C_{\parallel}^{epi}(\mathbf{I} - \mathbf{n}\otimes\mathbf{n}), \end{aligned} \tag{1.13}$$

where the constants $K_{\perp}^{epi}$, $K_{\parallel}^{epi}, K_{\perp}^{epi}$, $C_{\parallel}^{epi}$ are local values of stiffness and viscosity of the epicardial tissue in the normal or tangential directions. At the endocardium Γ_0^{endo}, equation $(1.12)_3$ accounts for the pressure $p(t)$ exerted by the blood contained in the ventricular chamber by a lumped parameters model. Finally, at the base Γ_0^{base}, we set the energy-consistent boundary condition $(1.12)_4$, originally proposed in [21], that provides an explicit expression for the stresses located at the boundary Γ_0^{base}, where we have defined the vector

$$\mathbf{v}^{base}(t) = \frac{\int_{\Gamma_0^{endo}} J\mathbf{F}^{-T}\mathbf{n}d\Gamma_0}{\int_{\Gamma_0^{base}} \left\|J\mathbf{F}^{-T}\mathbf{n}\right\| d\Gamma_0}.$$

In particular, Γ_0^{base} is an artificial boundary and it is provided with boundary conditions that account for the effect of the neglected part of the domain on the considered part, which is mainly due to the blood pressure in the endocardial boundary over the truncated part. Thanks to Eq. $(1.12)_4$, in fact, the stress on Γ_0^{base} perfectly balances the stress exerted on Γ_0^{endo}, which is in contact with the blood, so the net force exerted by the fluid

on the solid is null. This is coherent with the hydrostatic nature of the pressure force, which contributes to the energy of the system, but not to its momentum.

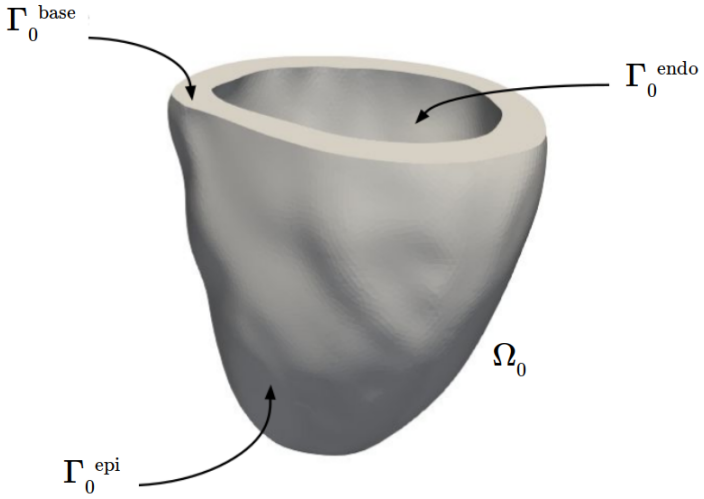

Figure 1.1: Representation of the left ventricle and its boundaries [25, 45].

1.2.3. A lumped parameters model for closed-loop blood circulation

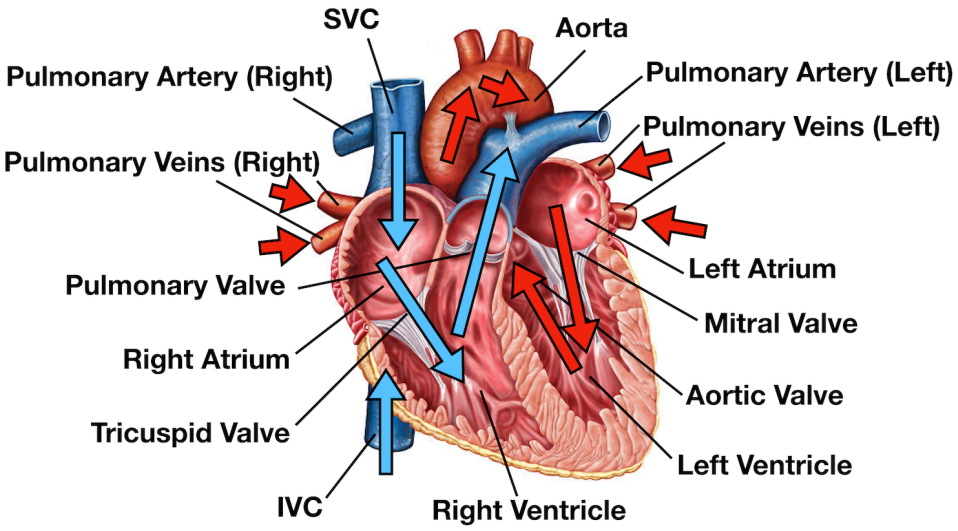

Figure 1.2: Heart anatomy and schematical representation of blood circulation.[2]

To surrogate the intracavity blood flow in the endocardium, without coupling the mechanical model with Navier-Stokes equations for the blood flow inside the cavity as in [41, 42], we consider a simplified lumped description [5, 21, 43].

[2]https://www.ezmedlearning.com/blog/heart-blood-flow-diagram

The pressure $p = p(t)$ in the left ventricular (LV) cavity follows a relatively simple closed-loop model, based on the following four phases:

1. Isovolumetric LV contraction phase, where $p(t)$ increases from the end diastolic pressure (EDP) p_{ED} to the pressure reached when the aortic valve opens p_{AVO}, with the ventricular volume V constant;

2. Ejection phase, where the pressure-volume relationship is described by the following two-element Windkessel model [44]:

$$\begin{cases} C\dfrac{dp}{dt} = -\dfrac{p}{R} - \dfrac{dV}{dt}, & t \in (T_1, T_2] \\ p(T_1) = p_{AVO}, \end{cases} \tag{1.14}$$

   where T_1 is the time when the aortic valve opens and $T_2 > T_1$ is the time when the aortic valve closes. The latter coincides to the end of volume reduction, that is, to the time at which $\dfrac{dV}{dt}$ changes sign. The parameters $C, R > 0$ represent the capacitance and the resistance of the equivalent electric circuit associated to the model, respecively;

3. Isovolumetric LV relaxation phase, where $p(t)$ decreases to the pressure p_{MVO} reached when the mitral valve opens;

4. Filling phase, where $p(t)$ increases linearly to the end diastolic pressure p_{ED}.

To compute the ventricular volume V we use the following formula, as in [43] (see [29] for its derivation):

$$V(t) = \int_{\Gamma_0^{endo}} J(\mathbf{d})\boldsymbol{\xi} \cdot \mathbf{F}^{-T}(\mathbf{d})\mathbf{n}\, d\Gamma_0, \tag{1.15}$$

where $\boldsymbol{\xi}$ is a vector directed as the centerline of the left ventricle.

1.3. Electromechanical coupling

As we have seen in section 1.2.2, the values of the calcium ion concentration $[Ca^{2+}]_i$ are used to compute the active stress tension T_a in order to model the internal active forces responsible for the contraction. Sometimes those values are prescribed as a given data to the mechanics problem, as, e.g., in [46], however, to have a more complete and reliable description of the cardiac contraction mechanism, they should be obtained from the monodomain problem, leading to a one-way coupled electromechanical problem.
Moreover, the mechanics problem influences the electrical problem, yielding to a fully coupled electromechanical problem; in fact, the electrical propagation needs to account to the evolution of the domain in time, due to cardiac relaxation and contraction. This

can be modeled by the introduction of some *mechano-electrical feedbacks* in the electrical model written in the reference configuration, such as the dependence of the ionic current on the stretch in the fiber direction (for further details see [6, 49, 50]). However, in this work, we consider the former, simpler, yet not trivial case, by neglecting any form of *mechano-electrical feedback*.

1.3.1. Electrical solution influence on cardiac deformation

As we introduced, the one-way electromechanical coupling develops around the fact that the active tension depends on the ionic model solution. In particular, the third ionic variable w_3 in the Bueno-Orovio model (1.2) is an adimensional indicator of intracellular calcium concentration, which can be rescaled to the interval $[0, 2.5]$ μM and can be used as input in the computation of the active tension. Namely, the activation model considered, Eq. (1.10), becomes:

$$\begin{cases} \dfrac{\partial T_a}{\partial t} = A(w_3, T_a) = \dfrac{1}{\tau}(T_a^{steady}(w_3, SL) - T_a), & in \ \ \Omega_0 \times (0, T) \\ T_a = T_{a,0}, & in \ \ \Omega \times \{0\} \end{cases} \tag{1.16}$$

where the active tension $T_a = T_a(w_3(\mathbf{X}, t))$ evolves in time according to the propagation of intracellular calcium concentration in the reference undeformed configuration Ω_0.
Thus, the solution of the cardiac electromechanics problem consists in the following steps:

- Step 1: we solve the the cardiac electrophysiology problem, Eq. (1.2), on the reference undeformed configuration Ω_0 to find the propagation of the potential u and the intracellular calcium concentration w_3 in time;
- Step 2: the propagation of calcium influences the evolution of the active tension, which is obtained solving Eq. (1.20), on the reference configuration;
- Step 3: we solve the cardiac mechanics problem (1.12), where, through the active component of the Piola-Kirchhoff tensor $\mathbf{P}_a$, the cardiac deformation depends in time by the evolution of the active tension T_a and, as a consequence, depends indirectly on the variation of the intracellular calcium on the reference undeformed domain Ω_0.

In figure 1.3 a schematical representation of the electromechanical coupling is shown.

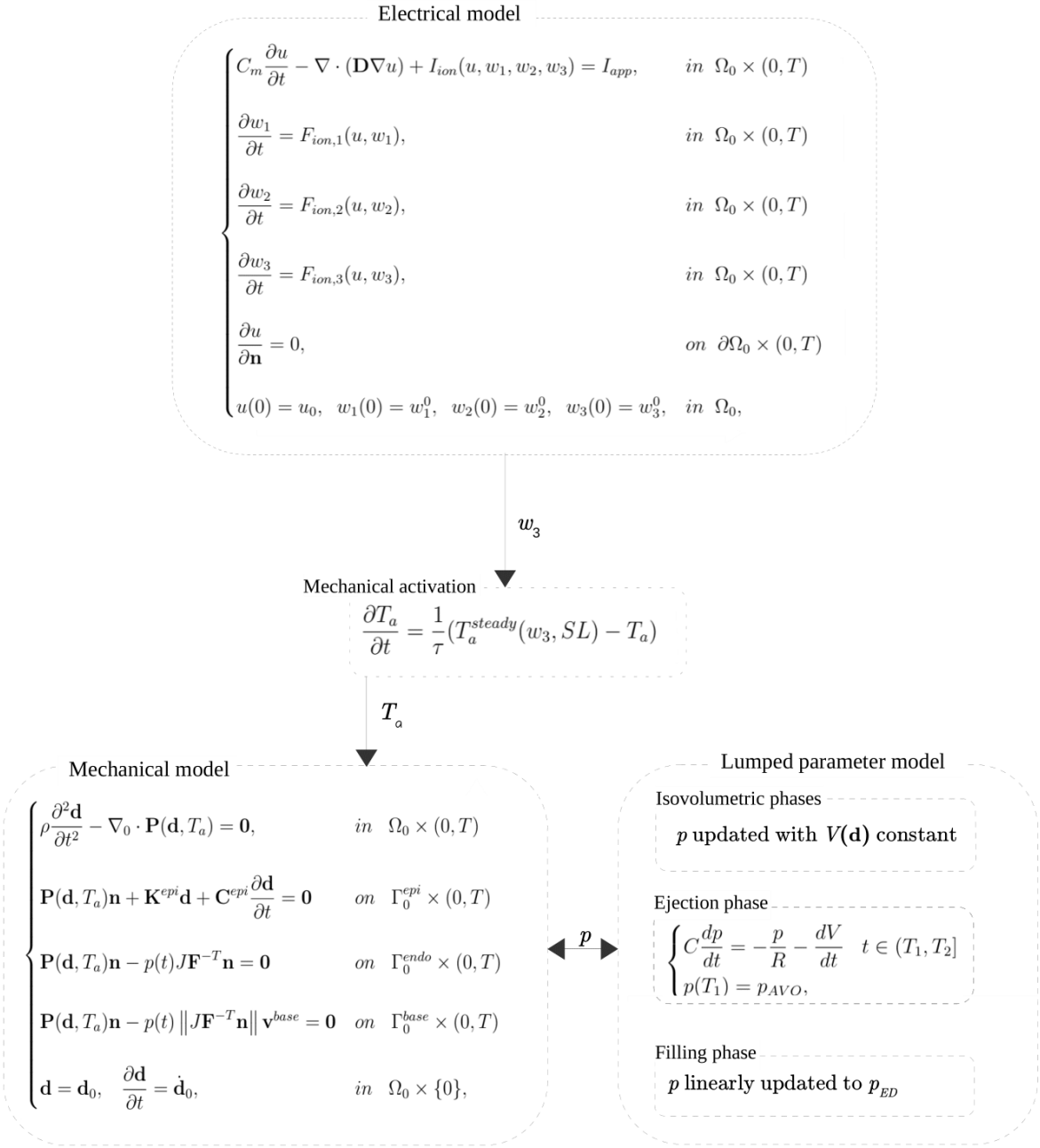

Figure 1.3: Schematical representation of the one-way electromechanical coupling.

Hence, for completeness, here we report the coupled EM problem:

$$\begin{cases} C_m \dfrac{\partial u}{\partial t} - \nabla \cdot (\mathbf{D}\nabla u) + I_{ion}(u, w_1, w_2, w_3) = I_{app}, & in\ \ \Omega_0 \times (0,T) \\ \dfrac{\partial w_1}{\partial t} = F_{ion,1}(u, w_1), & in\ \ \Omega_0 \times (0,T) \\ \dfrac{\partial w_2}{\partial t} = F_{ion,2}(u, w_2), & in\ \ \Omega_0 \times (0,T) \\ \dfrac{\partial w_3}{\partial t} = F_{ion,3}(u, w_3), & in\ \ \Omega_0 \times (0,T) \\ \dfrac{\partial u}{\partial \mathbf{n}} = 0, & on\ \ \partial\Omega_0 \times (0,T) \\ u(0) = u_0, \ \ w_1(0) = w_1^0, \ \ w_2(0) = w_2^0, \ \ w_3(0) = w_3^0, & in\ \ \Omega_0 \times \{0\}, \\ \dfrac{\partial T_a}{\partial t} = A(w_3, T_a) = \dfrac{1}{\tau}(T_a^{steady}(w_3, SL) - T_a), & in\ \ \Omega_0 \times (0,T) \\ T_a = T_{a,0}, & in\ \ \Omega_0 \times \{0\} \\ \rho \dfrac{\partial^2 \mathbf{d}}{\partial t^2} - \nabla_0 \cdot \mathbf{P}(\mathbf{d}, T_a) = \mathbf{0}, & in\ \ \Omega_0 \times (0,T) \\ \mathbf{P}(\mathbf{d}, T_a)\mathbf{n} + \mathbf{K}^{epi}\mathbf{d} + \mathbf{C}^{epi}\dfrac{\partial \mathbf{d}}{\partial t} = \mathbf{0}, & on\ \ \Gamma_0^{epi} \times (0,T) \\ \mathbf{P}(\mathbf{d}, T_a)\mathbf{n} - pJ\mathbf{F}^{-T}\mathbf{n} = \mathbf{0}, & on\ \ \Gamma_0^{endo} \times (0,T) \\ \mathbf{P}(\mathbf{d}, T_a)\mathbf{n} - p\left\|J\mathbf{F}^{-T}\mathbf{n}\right\| \mathbf{v}^{base} = \mathbf{0}, & on\ \ \Gamma_0^{base} \times (0,T) \\ \mathbf{d} = \mathbf{d}_0, \quad \dfrac{\partial \mathbf{d}}{\partial t} = \dot{\mathbf{d}}_0, & in\ \ \Omega_0 \times \{0\}, \end{cases} \tag{1.17}$$

where the endocardial pressure p has to be determined, depending on the cardiac cycle phase, by the lumped parameters model presented in section 1.2.3. Namely, coupling (1.12), where $T \in (0, T_4)$, with

$$\begin{cases} V(\mathbf{d}(t)) = V(\mathbf{d}(0)), & in\ \ (0, T_1] \\ p(0) = p_{ED}, & in\ \ 0 \\ C\dfrac{dp}{dt} = -\dfrac{p}{R} - \dfrac{dV}{dt}, & in\ \ (T_1, T_2] \\ p(T_1) = p_{AVO}, & in\ \ T_1 \\ V(\mathbf{d}(t)) = V(\mathbf{d}(T_2)), & in\ \ (T_2, T_3] \\ p(T_2) = p_{EVR}, & in\ \ T_2, \end{cases} \tag{1.18}$$

where p_{ED} is the end diastolic pressure, p_{AVO} is the pressure when the aortic valve opens and p_{EVR} is the pressure when the left ventricle volume reduction ends (the end of the ejection phase). Then, from T_3 to T_4, there is the filling phase, where $p(t)$ from the value of p_{MVO}, the pressure when the mitrial valve opens, linearly increases to p_{ED}, in order to start again the loop. However, in this work, we will focus only on the first two phases, representing the systole in each heartbeat. In Eq. (1.18), the pressure is continuous in time and the time instants $T_1 < T_2 < T_3 < T_4$ refers to the times when the pressure of a

phase reaches the value of the initial pressure of the following phase.

1.4. Parameters of interest

The problems introduced so far needs to be solved in different scenarios in order to asses the effect of clinically relevant parameters on their solutions, by taking into account, for example, a possible inter-patient variability. We denote by $\boldsymbol{\mu} \in \mathcal{P} \subset \mathbb{R}^{N_p}$ the set of N_p selected parameters.
In particular, when considering an electromechanical coupling, we are interested in analyzing how the electrical conductivities σ_m^l, σ_m^t, σ_m^n or the fibers orientation $\mathbf{f}_0$ affect heart contraction. In fact, electrical conductivities significantly influence the propagation of the electrical signal and, consequently, the displacement of the cardiac muscle. In this work, in particular, we show the results of a variation of the conductivity coefficient along the fiber direction and how it affects the propagation of the transmembrane potential and the intracellular calcium concentration. Additional parameters of interest are the ones involved in the cardiac mechanics, such as, e.g.: the coefficients of the strain energy function, in Eq. (1.8); the Bulk modulus B, in Eq. (1.9), related to the material incompressibility; the parameters in the Windkessel model, Eq. (1.14). In this work, we focus our attention on the variations of the Bulk modulus and the peripheral resistance R in the Windkessel model, to understand how they influences the cardiac deformation in the mechanic contraction, where the active contraction comes from the electrical propagation.

Regarding the cardiac electrophysiology, we thus have $\mathbf{D} = \mathbf{D}(\boldsymbol{\mu})$ and the parametrized version of the electrical model (1.2) reads as:

$$\begin{cases} C_m \dfrac{\partial u(\boldsymbol{\mu})}{\partial t} - \nabla \cdot (\mathbf{D}(\boldsymbol{\mu}) \nabla u(\boldsymbol{\mu})) + \\ \qquad + I_{ion}(u(\boldsymbol{\mu}), w_1(\boldsymbol{\mu}), w_2(\boldsymbol{\mu}), w_3(\boldsymbol{\mu})) = I_{app}, & in \ \ \Omega_0 \times (0,T) \\ \dfrac{\partial w_1(\boldsymbol{\mu})}{\partial t} = F_{ion,1}(u(\boldsymbol{\mu}), w_1(\boldsymbol{\mu})), & in \ \ \Omega_0 \times (0,T) \\ \dfrac{\partial w_2(\boldsymbol{\mu})}{\partial t} = F_{ion,2}(u(\boldsymbol{\mu}), w_2(\boldsymbol{\mu})), & in \ \ \Omega_0 \times (0,T) \\ \dfrac{\partial w_3(\boldsymbol{\mu})}{\partial t} = F_{ion,3}(u(\boldsymbol{\mu}), w_3(\boldsymbol{\mu})), & in \ \ \Omega_0 \times (0,T) \\ \dfrac{\partial u(\boldsymbol{\mu})}{\partial \mathbf{n}} = 0, & on \ \ \partial\Omega_0 \times (0,T) \\ u(0) = u_0, \ \ w_1(0) = w_1^0, \ \ w_2(0) = w_2^0, \ \ w_3(0) = w_3^0, & in \ \ \Omega_0, \end{cases} \tag{1.19}$$

If $\mathbf{D}$ is $\boldsymbol{\mu}$-dependent, also the potential and the ionic variables will depend on parameters. Since the activation equation depends on the solution of the electrical problem, we also

have $T_a = T_a(\boldsymbol{\mu})$, so that (1.20) reads as

$$\frac{\partial T_a(\boldsymbol{\mu})}{\partial t} = A(w_3(\boldsymbol{\mu}), T_a(\boldsymbol{\mu})) = \frac{1}{\tau}(T_a^{steady}(w_3(\boldsymbol{\mu}), SL) - T_a(\boldsymbol{\mu})). \tag{1.20}$$

Similarly, for the mechanical problem, we have $\mathbf{d} = \mathbf{d}(\boldsymbol{\mu})$ and $p(t) = p(t; \boldsymbol{\mu})$, either if we consider parameters that directly affects mechanics or parameters coming from the electrophysiology from the electromechanical coupling. Namely, the parametrized version of (1.12) becomes:

$$\begin{cases} \rho\dfrac{\partial^2 \mathbf{d}(\boldsymbol{\mu})}{\partial t^2} - \nabla_0 \cdot \mathbf{P}(\mathbf{d}(\boldsymbol{\mu}), T_a(\boldsymbol{\mu})) = \mathbf{0}, & in \quad \Omega_0 \times (0,T) \\ \mathbf{P}(\mathbf{d}(\boldsymbol{\mu}), T_a(\boldsymbol{\mu}))\mathbf{n} + \mathbf{K}^{epi}\mathbf{d}(\boldsymbol{\mu}) + \mathbf{C}^{epi}\dfrac{\partial \mathbf{d}(\boldsymbol{\mu})}{\partial t} = \mathbf{0} & on \quad \Gamma_0^{epi} \times (0,T) \\ \mathbf{P}(\mathbf{d}(\boldsymbol{\mu}), T_a(\boldsymbol{\mu}))\mathbf{n} - p(t;\boldsymbol{\mu})J\mathbf{F}^{-T}\mathbf{n} = \mathbf{0} & on \quad \Gamma_0^{endo} \times (0,T) \\ \mathbf{P}(\mathbf{d}(\boldsymbol{\mu}), T_a(\boldsymbol{\mu}))\mathbf{n} - p(t;\boldsymbol{\mu})\left\|J\mathbf{F}^{-T}\mathbf{n}\right\|\mathbf{v}^{base} = \mathbf{0} & on \quad \Gamma_0^{base} \times (0,T) \\ \mathbf{d} = \mathbf{d}_0, \quad \dfrac{\partial \mathbf{d}}{\partial t} = \dot{\mathbf{d}}_0 & in \quad \Omega_0 \times \{0\}. \end{cases} \tag{1.21}$$

2 | Numerical approximations by full order methods

The full-order numerical approximation of the core models considered in this work is performed through a Galerkin-Finite Element Method (FEM) for the space discretization and Finite Differences for time discretization[1]. Moreover, we consider a finer discretization in space for the cardiac electrophysiology model (1.2) than the one used for the mechanical model (1.12). This is motivated by the requirement of a higher resolution for (1.2) due to the sharp wavefronts characterizing electrophysiological solutions, while the mechanical model feature larger spatial scales [47, 48]. Namely, we consider two nested hexahedral meshes $\mathcal{T}_{h_e}$ and $\mathcal{T}_{h_m}$ of the reference undeformed computational domain Ω_0, where $\mathcal{T}_{h_e}$ has been generated by uniformly refining $\mathcal{T}_{h_m}$ according to an octree structure [26], i.e. by recursively splitting each parent element of $\mathcal{T}_{h_m}$ into eight sub-elements for a prescribed number of times corresponding to the number of refinement steps chosen. Here h_e and h_m (with $h_e < h_m$) represent the mesh sizes, which are computed as the mean diameter over all the elements. The elements of the FEM adopted consist in continuous, piecewise polynomials of degree 1 for both the cardiac electrophysiology and the cardiac mechanics space discretization.
We then denote by N_u, N_{w_1}, N_{w_3}, N_{w_3}, N_{T_a} and $N_{\mathbf{d}}$ the number of degrees of freedom (DOFs) for the transmembrane potential, the three ionic variables, the active tension and the displacement, respectively.
For the sake of notation, the dependence on the parameter vector $\boldsymbol{\mu}$ is understood in this chapter.

2.1. Cardiac Electrophysiology

In this section we briefly review the construction of high-fidelity full order models for cardiac electrophysiology relying on the Galerkin-Finite Element method.

[1]For further details on the implementation of the full order approximation methods presented in this chapter, see https://lifex.gitlab.io/lifex/

2.1.1. Weak formulation

In order to construct the FOM, let us consider the weak formulation of problem (1.19). For $t > 0$, given $I_{app}(t) \in L^2(\Omega_0)$, find $u(t) \in X = H^1(\Omega_0)$ and $\mathbf{w}(t) \in (L^2(\Omega_0))^3$ s.t.:

$$\begin{aligned}
&\int_{\Omega_0} \left(C_m \frac{\partial u}{\partial t} + I_{ion}(u, w_1, w_2, w_3) \right) \varphi d\Omega_0 \\
&\qquad + \int_{\Omega_0} \mathbf{D}\nabla u \cdot \nabla \varphi d\mathbf{x} = \int_{\Omega_0} I_{app} \varphi d\mathbf{x} \quad \forall \varphi \in H^1(\Omega_0), \\
&\int_{\Omega_0} \frac{\partial w_1}{\partial t} \xi_1 d\mathbf{x} = \int_{\Omega_0} F_{ion,1}(u, w_1) \xi_1 d\mathbf{x} \quad \forall \xi_1 \in L^2(\Omega_0), \\
&\int_{\Omega_0} \frac{\partial w_2}{\partial t} \xi_2 d\mathbf{x} = \int_{\Omega_0} F_{ion,2}(u, w_2) \xi_2 d\mathbf{x} \quad \forall \xi_2 \in L^2(\Omega_0), \\
&\int_{\Omega_0} \frac{\partial w_3}{\partial t} \xi_3 d\mathbf{x} = \int_{\Omega_0} F_{ion,3}(u, w_3) \xi_3 d\mathbf{x} \quad \forall \xi_3 \in L^2(\Omega_0), \\
&u(0) = u_0, \quad w_1(0) = w_{1,0}, \quad w_2(0) = w_{2,0}, \quad w_3(0) = w_{3,0}.
\end{aligned} \tag{2.1}$$

This coupled problem is well-posed and its wel-posedness can be derived from the more general results estabilished for the bidomain model, see e.g. [1, 3].

2.1.2. Galerkin FE method

Considering the mesh $\mathcal{T}_{h_e}$, we introduce the finite-dimensional space $X_{h_e} \subset X = H^1(\Omega)$ of dimension $dim(X_{h_e}) = N_{h_e}$. In particular, we have that $N_u = N_{h_e}$.
Let $\{\psi_j\}_{j=1}^{N_{h_e}}$ be a set of basis functions of the FE space X_{h_e}. Then, the discrete approximations of $u(\mathbf{X}, t)$ reads as:

$$u_{h_e}(t) = \sum_{i=1}^{N_{h_e}} u_i(t) \psi_i,$$

where the vector $\mathbf{u}_{h_e} = [u_1, ..., u_{N_{h_e}}]^T$, is obtained by solving the following semi-discretized monodomain equation: find $\mathbf{u}_{h_e}$ such that

$$\begin{cases} \mathbf{M} \dfrac{\partial \mathbf{u}_{h_e}}{\partial t} + \mathbf{A}\mathbf{u}_{h_e} + \mathbf{I}_{ion}(\mathbf{u}_{h_e}, \mathbf{w}_{1,h_e}, \mathbf{w}_{2,h_e}, \mathbf{w}_{3,h_e}) = \mathbf{I}_{app}(t), & t \in (0, T) \\ \mathbf{u}_{h_e}(0) = \mathbf{u}_0, \end{cases} \tag{2.2}$$

where

$$(\mathbf{M})_{ij} = C_m \int_{\Omega_0} \psi_i \psi_j d\Omega_0, \quad (\mathbf{A})_{ij} = \int_{\Omega_0} \mathbf{D}\nabla\psi_i \cdot \nabla\psi_j d\Omega_0,$$
$$(\mathbf{I}_{app})_j = \int_{\Omega_0} I_{app}(t) \psi_j d\Omega_0,$$

are, respectively, the mass matrix, the stiffness matrix and the activation term.
The nonlinear vector representing the ionic current is instead:

$$(\mathbf{I}_{ion}(\mathbf{u}_{h_e}, \mathbf{w}_{1,h_e}, \mathbf{w}_{2,h_e}, \mathbf{w}_{3,h_e}))_j = \int_{\Omega_0} I_{ion}(\mathbf{u}_{h_e}, \mathbf{w}_{1,h_e}, \mathbf{w}_{2,h_e}, \mathbf{w}_{3,h_e})\psi_j d\Omega_0.$$

Then, the vectors $\mathbf{w}_{1,h_e} = [w_{1,1}, ..., w_{1,N_{h_e}}]^T$, $\mathbf{w}_{2,h_e} = [w_{2,1}, ..., w_{2,N_{h_e}}]^T$ and $\mathbf{w}_{3,h_e} = [w_{3,1}, ..., w_{3,N_{h_e}}]^T$ represent the semi-discretized ionic variables, which indirectly depends on the space variable over the mesh $\mathcal{T}_{h_e}$ through the transmembrane potential, namely we have $N_{w_1} = N_{w_2} = N_{w_3} = N_{h_e}$. The semi-discretized version of the Bueno-Orovio ionic model can be written as follows:

$$\begin{cases} \dfrac{\partial \mathbf{w}_{1,h_e}}{\partial t} = \mathbf{F}_{ion,1}(\mathbf{u}_{h_e}, \mathbf{w}_{1,h_e}), & t \in (0,T) \\ \dfrac{\partial \mathbf{w}_{2,h_e}}{\partial t} = \mathbf{F}_{ion,2}(\mathbf{u}_{h_e}, \mathbf{w}_{2,h_e}), & t \in (0,T) \\ \dfrac{\partial \mathbf{w}_{3,h_e}}{\partial t} = \mathbf{F}_{ion,3}(\mathbf{u}_{h_e}, \mathbf{w}_{3,h_e}), & t \in (0,T) \\ \mathbf{w}_{1,h_e}(0) = \mathbf{w}_{1,0}, \quad \mathbf{w}_{2,h_e}(0) = \mathbf{w}_{2,0}, \quad \mathbf{w}_{3,h_e}(0) = \mathbf{w}_{3,0}, \end{cases} \tag{2.3}$$

where the vectors $\mathbf{F}_{ion,k}(\mathbf{u}_{h_e}, \mathbf{w}_{2,h_e}) \in \mathbb{R}^{N_{h_e}}$, $k = 1, 2, 3$, are nonlinear terms.

2.1.3. Time discretization and algebraic formulation

The time discretization of the semi-discretized monodomain system (2.2) and ionic model (2.3) are obtained relying on a finite difference scheme, namely the backward differentiation formula (BDF), of order σ, where σ can assume different values (e.g. $1, 2, ..$). In this work we consider a first order scheme, so σ is set to 1.
Given a partition of the time interval $(0, T)$ into N_t subintervals $(t^{(l)}, t^{(l+1)})$, $l = 0, ..., N_t - 1$, of length $\Delta t_e = t^{(l+1)} - t^{(l)}$, we have that $\mathbf{u}_{h_e}^{(l)} \approx \mathbf{u}_{h_e}(t^{(l)})$, $\mathbf{w}_{1,h_e}^{(l)} \approx \mathbf{w}_{1,h_e}(t^{(l)})$, $\mathbf{w}_{2,h_e}^{(l)} \approx \mathbf{w}_{2,h_e}(t^{(l)})$, $\mathbf{w}_{3,h_e}^{(l)} \approx \mathbf{w}_{3,h_e}(t^{(l)})$ and $\mathbf{I}_{app}^{(l)} \approx \mathbf{I}_{app}(t^{(l)})$ $\forall l = 0, ..., N_t$.
For what concerns the nonlinear terms, a semi-implicit approach is considered, for which the nonlinear vector $\mathbf{I}_{ion}$ can be evaluated around the solution already computed at time $t^{(l)}$ and this decouples the PDE from the ODE, leading to a linear system to be solved at each time step. Moreover, an hybrid ionic current interpolation strategy is used to evaluate the ionic current term [12].

The full-order model of (1.2) thus becomes: find $\mathbf{u}_{h_e}^{(l+1)}$, $\mathbf{w}_{1,h_e}^{(l+1)}$, $\mathbf{w}_{2,h_e}^{(l+1)}$ and $\mathbf{w}_{3,h_e}^{(l+1)}$ such that $\mathbf{u}_{h_e}^{(0)} = \mathbf{u}_0$, $\mathbf{w}_{1,h_e}^{(0)} = \mathbf{w}_{1,0}$, $\mathbf{w}_{2,h_e}^{(0)} = \mathbf{w}_{2,0}$, $\mathbf{w}_{3,h_e}^{(0)} = \mathbf{w}_{3,0}$ and, for $l = 0, ..., N_t - 1$,

$$\begin{cases} \dfrac{\mathbf{w}_{1,h_e}^{(l+1)} - \mathbf{w}_{1,h_e}^{(l)}}{\Delta t_e} - \mathbf{F}_{ion,1}(\mathbf{u}_{h_e}^{(l)}, \mathbf{w}_{1,h_e}^{(l+1)}) = \mathbf{0}, \\ \dfrac{\mathbf{w}_{2,h_e}^{(l+1)} - \mathbf{w}_{2,h_e}^{(l)}}{\Delta t_e} - \mathbf{F}_{ion,2}(\mathbf{u}_{h_e}^{(l)}, \mathbf{w}_{2,h_e}^{(l+1)}) = \mathbf{0}, \\ \dfrac{\mathbf{w}_{3,h_e}^{(l+1)} - \mathbf{w}_{3,h_e}^{(l)}}{\Delta t_e} - \mathbf{F}_{ion,3}(\mathbf{u}_{h_e}^{(l)}, \mathbf{w}_{3,h_e}^{(l+1)}) = \mathbf{0}, \\ \mathbf{M}\dfrac{\mathbf{u}_{h_e}^{(l+1)} - \mathbf{u}_{h_e}^{(l)}}{\Delta t_e} + \mathbf{A}\mathbf{u}_{h_e}^{(l+1)} + \mathbf{I}_{ion}(\mathbf{u}_{h_e}^{(l)}, \mathbf{u}_{h_e}^{(l+1)}, \mathbf{w}_{1,h_e}^{(l+1)}, \mathbf{w}_{2,h_e}^{(l+1)}, \mathbf{w}_{3,h_e}^{(l+1)}) - \mathbf{I}_{app}^{(l+1)} = \mathbf{0}, \end{cases} \tag{2.4}$$

where we udpate first the ionic model, by one iteration of the fixed point method, and then we solve the monodomain equation by the Newthon method to update the transmembrane potential. In fact, the equation $(2.4)_4$ can be rewritten in a residual form as follows:

$$\mathbf{r}(\mathbf{u}_{h_e}^{(l+1)}, \mathbf{w}_{1,h_e}^{(l+1)}, \mathbf{w}_{2,h_e}^{(l+1)}, \mathbf{w}_{3,h_e}^{(l+1)}) = \mathbf{L}(\mathbf{u}_{h_e}^{(l+1)}, \mathbf{w}_{1,h_e}^{(l+1)}, \mathbf{w}_{2,h_e}^{(l+1)}, \mathbf{w}_{3,h_e}^{(l+1)}) - \mathbf{f} = \mathbf{0},$$

where

$$\begin{aligned} &\mathbf{L}(\mathbf{u}_{h_e}^{(l+1)}, \mathbf{w}_{1,h_e}^{(l+1)}, \mathbf{w}_{2,h_e}^{(l+1)}, \mathbf{w}_{3,h_e}^{(l+1)}) = \\ &\qquad \mathbf{M}\frac{\mathbf{u}_{h_e}^{(l+1)} - \mathbf{u}_{h_e}^{(l)}}{\Delta t_e} + \mathbf{A}\mathbf{u}_{h_e}^{(l+1)} + \mathbf{I}_{ion}(\mathbf{u}_{h_e}^{(l)}, \mathbf{u}_{h_e}^{(l+1)}, \mathbf{w}_{1,h_e}^{(l+1)}, \mathbf{w}_{2,h_e}^{(l+1)}, \mathbf{w}_{3,h_e}^{(l+1)}), \\ &\qquad\qquad \mathbf{f} = \mathbf{I}_{app}^{(l+1)}. \end{aligned}$$

Hence, we define the residual $\mathbf{r}$ as

$$\begin{aligned} &\mathbf{r}(\mathbf{u}_{h_e}^{(l+1)}, \mathbf{w}_{1,h_e}^{(l+1)}, \mathbf{w}_{2,h_e}^{(l+1)}, \mathbf{w}_{3,h_e}^{(l+1)}) = \\ &\qquad \mathbf{M}\frac{\mathbf{u}_{h_e}^{(l+1)} - \mathbf{u}_{h_e}^{(l)}}{\Delta t_e} + \mathbf{A}\mathbf{u}_{h_e}^{(l+1)} + \mathbf{I}_{ion}(\mathbf{u}_{h_e}^{(l)}, \mathbf{u}_{h_e}^{(l+1)}, \mathbf{w}_{1,h_e}^{(l+1)}, \mathbf{w}_{2,h_e}^{(l+1)}, \mathbf{w}_{3,h_e}^{(l+1)}) - \mathbf{I}_{app}^{(l+1)}. \end{aligned} \tag{2.5}$$

Equation (2.5) represents the residual form of the monodomain equation and it is nonlinear; hence, it is linearized and solved at each time step using one iteration of the Newton method. Here is the scheme of the form

$$\begin{aligned} \mathbf{J}\boldsymbol{\delta}\mathbf{u}_{h_e} &= \mathbf{r}(\mathbf{u}_{h_e,0}^{(l+1)}, \mathbf{w}_{1,h_e}^{(l+1)}, \mathbf{w}_{2,h_e}^{(l+1)}, \mathbf{w}_{3,h_e}^{(l+1)}), \\ \mathbf{u}_{h_e}^{(l+1)} &= \mathbf{u}_{h_e,0}^{(l+1)} - \boldsymbol{\delta}\mathbf{u}_{h_e}, \end{aligned} \tag{2.6}$$

where $\mathbf{J}$ is the Jacobian operator of $\mathbf{L}$, defined as:

$$\mathbf{J}\boldsymbol{\delta}\mathbf{u} = \mathbf{M}\frac{\boldsymbol{\delta}\mathbf{u}}{\Delta t_e} + \mathbf{A}\boldsymbol{\delta}\mathbf{u}. \tag{2.7}$$

Since we are treating the ionic current $\mathbf{I}_{ion}$ semi-implicitly with respect to $\mathbf{u}_{h_e}^{(l+1)}$, we have

that $\mathbf{J}$ is a constant term with respect to $\mathbf{u}_{h_e,0}^{(l+1)}$. Moreover, for the Bueno-Orovio model, the semi-implicit approach adopted for the nonlinear term $\mathbf{I}_{ion}$ yields to $d\mathbf{I}_{ion} = \mathbf{0}$. In this way, the Jacobian doesn't need to be updated at each time-step and can be assembled just once. The initial guess of the Newton method is $\mathbf{u}_{h_e,0}^{(l+1)} = \mathbf{u}_{h_e}^{(l)}$.
Therefore, we can rewrite the FOM as follow: find $\mathbf{u}_{h_e}^{(l+1)}$, $\mathbf{w}_{1,h_e}^{(l+1)}$, $\mathbf{w}_{2,h_e}^{(l+1)}$ and $\mathbf{w}_{3,h_e}^{(l+1)}$ such that $\mathbf{u}_{h_e}^{(0)} = \mathbf{u}_0$, $\mathbf{w}_{1,h_e}^{(0)} = \mathbf{w}_{1,0}$, $\mathbf{w}_{2,h_e}^{(0)} = \mathbf{w}_{2,0}$, $\mathbf{w}_{3,h_e}^{(0)} = \mathbf{w}_{3,0}$ and, for $l = 0, ..., N_t - 1$,

$$\begin{cases} \dfrac{\mathbf{w}_{1,h_e}^{(l+1)} - \mathbf{w}_{1,h_e}^{(l)}}{\Delta t_e} - \mathbf{F}_{ion,1}(\mathbf{u}_{h_e}^{(l)}, \mathbf{w}_{1,h_e}^{(l+1)}) = \mathbf{0}, \\ \dfrac{\mathbf{w}_{2,h_e}^{(l+1)} - \mathbf{w}_{2,h_e}^{(l)}}{\Delta t_e} - \mathbf{F}_{ion,2}(\mathbf{u}_{h_e}^{(l)}, \mathbf{w}_{2,h_e}^{(l+1)}) = \mathbf{0}, \\ \dfrac{\mathbf{w}_{3,h_e}^{(l+1)} - \mathbf{w}_{3,h_e}^{(l)}}{\Delta t_e} - \mathbf{F}_{ion,3}(\mathbf{u}_{h_e}^{(l)}, \mathbf{w}_{3,h_e}^{(l+1)}) = \mathbf{0}, \\ \mathbf{J}\boldsymbol{\delta}\mathbf{u}_{h_e} = \mathbf{r}(\mathbf{u}_{h_e,0}^{(l+1)}, \mathbf{w}_{1,h_e}^{(l+1)}, \mathbf{w}_{2,h_e}^{(l+1)}, \mathbf{w}_{3,h_e}^{(l+1)}), \\ \mathbf{u}_{h_e}^{(l+1)} = \mathbf{u}_{h_e,0}^{(l+1)} - \boldsymbol{\delta}\mathbf{u}_{h_e}, \quad \mathbf{u}_{h_e,0}^{(l+1)} = \mathbf{u}_{h_e}^{(l)}. \end{cases} \tag{2.8}$$

The most demanding computational tasks are related to the assembling of the terms $\mathbf{I}_{ion}$ and $\mathbf{F}_{ion,k}$, $k = 1, 2, 3$, at each time step, and to the solution of the linearized system $(2.8)_4$. Moreover, the time step Δt_e is required to be small to ensure convergence.

2.2. Cardiac Mechanics

In this section, similarly to what we have seen in the previous one, we briefly review the construction of high-fidelity full order models for cardiac mechanics relying on the Galerkin-Finite Element method.

2.2.1. Semi-discretization by Galerkin FE method

Mechanical activation model

The semi-discrete formulation of the activation model (1.20), which is developed on the mesh $\mathcal{T}_{h_m}$, reads: find $\mathbf{T}_{a,h_m}$ such that:

$$\begin{cases} \dfrac{\partial \mathbf{T}_{a,h_m}}{\partial t} = \dfrac{1}{\tau}(\mathbf{T}_{a,h_m}^{steady}(\mathbf{w}_{3,h_m}(t), SL) - \mathbf{T}_{a,h_m}) \quad t \in (0,T) \\ \mathbf{T}_{a,h_m}(0) = \mathbf{T}_{a,0}, \end{cases} \tag{2.9}$$

where $\mathbf{T}_{a,h_m}, \mathbf{T}_{a,h_m}^{steady} \in \mathbb{R}^{N_{T_a}}$ and $\mathbf{w}_{3,h_m}(t)$ is obtained by mapping the intracellular calcium concentration of the Bueno-Orovio model from the finer mesh $\mathcal{T}_{h_e}$, adopted to discretize in space the electrical problem, to the coarser mesh $\mathcal{T}_{h_m}$, adopted to discretize in space the mechanical problem. The map as been built by means of an intergrid transfer operator [26] between the two meshes, thus obtaining $\mathbf{w}_{3,h_m}(t) \in \mathbb{R}^{N_{T_a}}$ from $\mathbf{w}_{3,h_e}(t) \in \mathbb{R}^{N_{h_e}}$.

Mechanical model

Denoting by $[X_{h_m}]^3$ the finite dimensional subspace of vector valued functions, where $X_{h_m} \subset X = H^1(\Omega_0)$, and by $\{\boldsymbol{\phi}_i\}_i^{N_d}$ its basis, the semi-discretized version of problem (1.12) reads: given $\mathbf{T}_{a,h_m}(t)$, find, $\forall t \in (0,T)$, $\mathbf{d}_{h_m}(t) \in [X_{h_m}]^3$ such that

$$\begin{aligned}
&\int_{\Omega_0} \rho \ddot{\mathbf{d}}_{h_m}(t) \cdot \boldsymbol{\phi}_i d\Omega_0 + \int_{\Omega_0} \mathbf{P}(\mathbf{d}_{h_m}(t), \mathbf{T}_{a,h_m}) : \nabla \boldsymbol{\phi}_i d\Omega_0 \\
&\quad + \int_{d\Gamma_0^{epi}} [(\mathbf{n}\otimes\mathbf{n})(K_\perp^{epi}\mathbf{d}_{h_m}(t) + C_\perp^{epi}\dot{\mathbf{d}}_{h_m}(t)) \\
&\quad + (\mathbf{I}-\mathbf{n}\otimes\mathbf{n})(K_\parallel^{epi}\mathbf{d}_{h_m}(t) + C_\parallel^{epi}\dot{\mathbf{d}}_{h_m}(t))] \cdot \boldsymbol{\phi}_i d\Gamma_0^{epi} = \\
&\quad - p(t) \int_{d\Gamma_0^{endo}} J_{h_m}\mathbf{F}_{h_m}^{-T}\mathbf{n} \cdot \boldsymbol{\phi}_i d\Gamma_0^{endo} \\
&\quad + p(t) \int_{d\Gamma_0^{base}} \left\| J_{h_m}\mathbf{F}_{h_m}^{-T}\mathbf{n} \right\| \mathbf{v}_{h_m}^{base} \cdot \boldsymbol{\phi}_i d\Gamma_0^{base} \quad \forall i = 1, ..., N_d,
\end{aligned} \tag{2.10}$$

with $\mathbf{d}_{h_m}(0) = \mathbf{d}_{0,h_m}$, $\dot{\mathbf{d}}_{h_m}(0) = \dot{\mathbf{d}}_{0,h_m}$ and

$$\mathbf{v}^{base}(t) = \frac{\int_{\Gamma_0^{endo}} J\mathbf{F}^{-T}\mathbf{n} d\Gamma_0}{\int_{\Gamma_0^{base}} \left\| J\mathbf{F}^{-T}\mathbf{n} \right\| d\Gamma_0}.$$

The corresponding semi-discretized algebraic formulation reads: find $\underline{\mathbf{d}}_{h_m}(t)$ such that

$$\begin{cases}
\rho\mathbf{M}\ddot{\underline{\mathbf{d}}}_{h_m}(t) + \mathcal{F}\dot{\underline{\mathbf{d}}}_{h_m}(t) + \mathcal{G}\underline{\mathbf{d}}_{h_m}(t) + \mathbf{S}(\underline{\mathbf{d}}_{h_m}(t), \mathbf{T}_{a,h_m}(t)) = p(t)\mathbf{p}(\underline{\mathbf{d}}_{h_m}(t)), \quad t \in (0,T) \\
\underline{\mathbf{d}}_{h_m}(0) = \underline{\mathbf{d}}_{0,h_m}, \quad \dot{\underline{\mathbf{d}}}_{h_m}(0) = \dot{\underline{\mathbf{d}}}_{0,h_m},
\end{cases} \tag{2.11}$$

with :

$$\begin{aligned}
(\mathbf{M})_{i,j} &= \int_{\Omega_0} \boldsymbol{\phi}_j \boldsymbol{\phi}_i d\Omega_0, \\
(\mathbf{S})(\underline{\mathbf{d}}_{h_m}(t), \mathbf{T}_{a,h_m}(t)))_i &= \int_{\Omega_0} \mathbf{P}(\mathbf{d}_{h_m}(t), \mathbf{T}_{a,h_m}) : \nabla \boldsymbol{\phi}_i d\Omega_0, \\
(\mathcal{F})_{i,j} &= \int_{d\Gamma_0^{epi}} [(\mathbf{n}\otimes\mathbf{n})K_\perp^{epi} + (\mathbf{I}-\mathbf{n}\otimes\mathbf{n})K_\parallel^{epi}]\boldsymbol{\phi}_j \cdot \boldsymbol{\phi}_i d\Gamma_0^{epi}, \\
(\mathcal{G})_{i,j} &= \int_{d\Gamma_0^{epi}} [(\mathbf{n}\otimes\mathbf{n})C_\perp^{epi} + (\mathbf{I}-\mathbf{n}\otimes\mathbf{n})C_\parallel^{epi}]\boldsymbol{\phi}_j \cdot \boldsymbol{\phi}_i d\Gamma_0^{epi}, \\
(\mathbf{p}(\underline{\mathbf{d}}_{h_m}(t)))_i &= \int_{d\Gamma_0^{base}} \left\| J_{h_m}\mathbf{F}_{h_m}^{-T}\mathbf{n} \right\| \mathbf{v}_{h_m}^{base} \cdot \boldsymbol{\phi}_i d\Gamma_0^{base} \\
&\quad - \int_{d\Gamma_0^{endo}} J_{h_m}\mathbf{F}_{h_m}^{-T}\mathbf{n} \cdot \boldsymbol{\phi}_i d\Gamma_0^{endo},
\end{aligned}$$

where $\underline{\mathbf{d}}_{h_m}(t) = [\mathbf{d}_{1,h_m}(t), \mathbf{d}_{2,h_m}(t), ..., \mathbf{d}_{N_d,h_m}(t)]^T$ denotes the semi-discretized version of the displacement field.

2.2.2. Time discretization and algebraic formulation

For what concerns the time discretization of problems (2.9) and (2.11), we use a similar approach to the one described in section 2.1.3, that is, we rely on a BDF of order $\sigma = 1$. However, we consider a bigger time-step than the one used for cardiac electrophysiology, since in the mechanical problem we are not dealing with traveling waves that require a finer discretization in time. Namely, given a partition of the time interval $(0, T)$ into N_{t_m} subintervals $(t^{(k)}, t^{(k+1)})$, $k = 0, ..., N_{t_m} - 1$, of length $\Delta t_m = t^{(k+1)} - t^{(k)}$, where $\Delta t_m > \Delta t_e$, we have that $\underline{\mathbf{d}}_{h_m}^{(k)} \approx \underline{\mathbf{d}}_{h_m}(t^{(k)})$ and $\mathbf{T}_{a,h_m}^{(k)} \approx \mathbf{T}_{a,h_m}(t^{(k)}) \quad \forall k = 0, ..., N_{t_m}$.
Moreover, let us consider $q = \dfrac{\Delta t_m}{\Delta t_e}$, which denotes the number of time-steps Δt_e required to complete a time-step Δt_m. Thus, we introduce the notation $t^{(k)} = t^{q(l)}$ $\forall k = l = 0, ..., N_{t_m}$, to indicate the same time instant in the two different time discretizations adopted for the mechanical and the electrical problem, respectively.
The activation model is discretized following an implicit approach, namely the problem reads: find $\mathbf{T}_{a,h_m}^{(k+1)}$ such that

$$\begin{cases} \dfrac{\mathbf{T}_{a,h_m}^{(k+1)} - \mathbf{T}_{a,h_m}^{(k)}}{\Delta t_m} = \dfrac{1}{\tau}(\mathbf{T}_{a,h_m}^{steady}(\mathbf{w}_{3,h_m}^{q(l+1)}, SL) - \mathbf{T}_{a,h_m}^{(k+1)}), \quad k = 0, .., N_{t_m} - 1 \\ \mathbf{T}_{a,h_m}^{(0)} = \mathbf{T}_{a,0}, \end{cases} \tag{2.12}$$

and it is solved at each time step by the fixed point method, using a tolerance equal to 10^{-8} and a maximum number of iteration equal to 30.
For the mechanical problem the treatment of the nonlinear terms also follows an implicit approach, due to the fact that the highly nonlinear (exponential) terms of the strain energy function $\mathcal{W}$ would need a restriction on the time step in both the semi-implicit and explicit contexts. The full-order model of problem (1.21) thus reads: find $\underline{\mathbf{d}}_{h_m}^{(k+1)}$ such that $\underline{\mathbf{d}}_{h_m}^{(0)} = \underline{\mathbf{d}}_{0,h_m}$, $\underline{\mathbf{d}}_{h_m}^{(1)} = \underline{\mathbf{d}}_{0,h_m} + \Delta t_m \dot{\underline{\mathbf{d}}}_{0,h_m}$ and, for each $k = 1, ..., N_{t_m} - 1$

$$\Big(\rho\frac{1}{\Delta t_m^2}\mathbf{M} + \frac{1}{\Delta t_m}\mathcal{F} + \mathcal{G}\Big)\underline{\mathbf{d}}_{h_m}^{(k+1)} + \mathbf{S}(\underline{\mathbf{d}}_{h_m}^{(k+1)}, \mathbf{T}_{a,h_m}^{(k+1)}) = \rho\frac{2}{\Delta t_m^2}\mathbf{M}\underline{\mathbf{d}}_{h_m}^{(k)} - \rho\frac{1}{\Delta t_m^2}\mathbf{M}\underline{\mathbf{d}}_{h_m}^{(k-1)} + \frac{1}{\Delta t_m}\mathcal{F}\underline{\mathbf{d}}_{h_m}^{(k)} + p^{(k+1)}\mathbf{p}(\underline{\mathbf{d}}_{h_m}^{(k)}, \underline{\mathbf{d}}_{h_m}^{(k+1)}). \tag{2.13}$$

To deal with the interaction of blood on the endocardium Γ_0^{endo}, in order to model the evolution of the pressure in time, we need to account the different phases of the cardiac cycle presented in subsection 1.2.3; namely we couple Eq. (2.13) to the discretization of Eq. (1.18). We then solve the coupled problem for the pressure and the displacement field by means of a Newton strategy.
Going into details, in the isovolumetric phases, we solve Eq. (2.13) coupled with the condition $V(\underline{\mathbf{d}}_{h_m}^{(k+1)}) = V(\underline{\mathbf{d}}_{h_m}^{(k)})$. This is a saddle-point problem, in the unknowns $\underline{\mathbf{d}}_{h_m}^{(k+1)}$

and $p^{(k+1)}$, which is solved by Schur complement reduction (see [21, 26] for more details). Namely, by moving all the terms in Eq. (2.13) to the left hand side we rewrite the equation in a residual form as

$$\mathbf{r}_{\mathbf{d}}^{(k+1)}(\underline{\mathbf{d}}_{h_m}^{(k+1)}, p^{(k+1)}) = \mathbf{0},$$

Then, by introducing the residual

$$r_p^{(k+1)}(\underline{\mathbf{d}}_{h_m}^{(k+1)}) = V(\underline{\mathbf{d}}_{h_m}^{(k+1)}) - V(\underline{\mathbf{d}}_{h_m}^{(k)}) = 0,$$

for $j = 0, 1, ...$ iterations of the Newton method, we solve the two linear systems:

$$J_{\mathbf{d},\mathbf{d}}^{(k+1),(j)}\mathbf{v}^{(k+1),(j)} = \mathbf{r}_{\mathbf{d}}^{(k+1),(j)}, \qquad J_{\mathbf{d},\mathbf{d}}^{(k+1),(j)}\mathbf{b}^{(k+1),(j)} = J_{\mathbf{d},p}^{(k+1),(j)} \tag{2.14}$$

where, at each time-step, for each iteration, $J_{\mathbf{d},\mathbf{d}} \in \mathbb{R}^{N_d \times N_d}$ is defined as $J_{\mathbf{d},\mathbf{d}} = \dfrac{\partial}{\partial \underline{\mathbf{d}}}\mathbf{r}_{\mathbf{d}}$, and $J_{\mathbf{d},p} \in \mathbb{R}^{N_d}$ is defined as $J_{\mathbf{d},p} = \dfrac{\partial}{\partial p}\mathbf{r}_{\mathbf{d}}$, with $\mathbf{r}_{\mathbf{d}} \in \mathbb{R}^{N_d}$, $\mathbf{v} \in \mathbb{R}^{N_d}$ and $\mathbf{w} \in \mathbb{R}^{N_d}$.
Thus, by the Schur complement method, we set

$$\begin{aligned} \delta p^{(k+1),(j)} &= \frac{p^{(k+1),(j)} - J_{p,\mathbf{d}}^{(k+1),(j)}\mathbf{v}^{(k+1),(j)}}{J_{p,\mathbf{d}}^{(k+1),(j)}\mathbf{b}^{(k+1),(j)}}, \\ \delta \underline{\mathbf{d}}_{h_m}^{(k+1),(j)} &= -(\mathbf{v}^{(k+1),(j)} + \mathbf{b}^{(k+1),(j)}\delta p^{(k+1),(j)}), \end{aligned} \tag{2.15}$$

where $J_{p,\mathbf{d}}^T \in \mathbb{R}^{N_d}$ is defined as $J_{p,\mathbf{d}} = \dfrac{\partial}{\partial \underline{\mathbf{d}}} r_p$, with $r_p \in \mathbb{R}$.
We then update

$$\begin{aligned} \underline{\mathbf{d}}_{h_m}^{(k+1),(j+1)} &= \underline{\mathbf{d}}_{h_m}^{(k+1),(j)} + \delta \underline{\mathbf{d}}_{h_m}^{(k+1),(j)} \\ p^{(k+1),(j+1)} &= p^{(k+1),(j)} + \delta p^{(k+1),(j)} \end{aligned}$$

choosing as initial guesses $\underline{\mathbf{d}}_{h_m}^{(k+1),(0)} = \underline{\mathbf{d}}_{h_m}^{(k)}$ and $p^{(k+1),(0)} = p^{(k)}$.
When $\left\| \mathbf{r}_{\mathbf{d}}^{(k+1),(j)} \right\|_2 < \epsilon$, for ϵ sufficiently small, and $j \leq N_{iter}^{max}$, we set

$$\underline{\mathbf{d}}_{h_m}^{(k+1)} = \underline{\mathbf{d}}_{h_m}^{(k+1),(j)}, \quad p^{(k+1)} = p^{(k+1),(j)}.$$

On the other hand, during the ejection phase, the pressure is updated before solving the mechanical problem, with an implicit treatment of p. In particular, here, the residual $\mathbf{r}_{\mathbf{d}}^{(k+1)}(\underline{\mathbf{d}}_{h_m}^{(k+1)}, p^{(k+1)}) = \mathbf{r}_{\mathbf{d}}^{(k+1)}(\underline{\mathbf{d}}_{h_m}^{(k+1)})$ does not depend on the pressure at time $t^{(k+1)}$, since it is update before solving the Newton step to update the displacement field. Namely, we solve the following two-element Windkessel model (1.14): for each k such that $t^{(k+1)} \in$

$(T_1, T_2]$, find $p^{(k+1)}$ such that:

$$\begin{cases} C\dfrac{p^{(k+1)} - p^{(k)}}{\Delta t_m} = -\dfrac{p^{(k+1)}}{R} - \dfrac{V^{(k)} - V^{(k-1)}}{\Delta t_m}, \\ p(T_1) = p_{AVO}, \end{cases} \tag{2.16}$$

and then we solve Eq. (2.13) by the Newton method: for $j = 0, 1, ...$, until a convergence criterion is fulfilled

$$\begin{cases} J_{\mathbf{d},\mathbf{d}}^{(k+1),(j)} \delta \underline{\mathbf{d}}_{h_m}^{(k+1),(j)} = -\mathbf{r}_{\mathbf{d}}^{(k+1),(j)}, \\ \underline{\mathbf{d}}_{h_m}^{(k+1),(j+1)} = \underline{\mathbf{d}}_{h_m}^{(k+1),(j)} + \delta \underline{\mathbf{d}}_{h_m}^{(k+1),(j)}. \end{cases} \tag{2.17}$$

choosing as initial guess $\underline{\mathbf{d}}_{h_m}^{(k+1),(0)} = \underline{\mathbf{d}}_{h_m}^{(k)}$.
When $\left\| \mathbf{r}_{\mathbf{d}}^{(k+1),(j)}(\boldsymbol{\mu}) \right\|_2 < \epsilon$, for ϵ sufficiently small, and $j \leq N_{iter}^{max}$, we set

$$\underline{\mathbf{d}}_{h_m}^{(k+1)} = \underline{\mathbf{d}}_{h_m}^{(k+1),(j)}.$$

A similar approach to the latter one is followed for the filling phase, where the pressure is linearly updated at each time step, before the update of the displacement field. The pressure increases until the end-diastolic pressure value p_{ED}, which corresponds to the end of the closed-loop for the blood circulation considered for each heartbeat.

3 | Reduced-order models for one-way coupled problems

The accurate solution of a coupled system like (1.1) is computationally demanding when full-order models (FOMs) such as the one introduced in the previous chapter are adopted. In fact, in order to capture the evolution of a very steep front and the fast dynamics of the electric signal propagation, strong constraints on the spatial mesh size and very small time steps are needed, thus yielding to the assembling of huge matrices. On the other hand, the mechanical problem is characterized by a complex nonlinear constitutive law, where the computational burden is represented by assembling the Jacobian matrices at each Newton step; moreover problem (1.12) depends on time through its coupling with the electrophysiology model, increasing its unsteadiness. Relying on full-order is thus prohibitive whenever such problems have to be solved many times, varying parameter dependent features affecting operators and/or data. In this chapter we present a possible reducedorder modeling strategy to address this computational task.

3.1. Reduced-order modeling

In this these we rely on the reduced basis method for parametrized problem, estending it to handle one-way coupled problems in cardiac electromechanics. The application of a projection-based ROM consists into the approximation of the solution of a FOM by means of a linear combination of few, problem-specific, global-basis functions obtained from a set of FOM snapshots. In particular, in the *offline* phase of the method, we consider proper orthogonal decomposition to build a reduced basis space and a (Petrov-)Galerkin projection to generate the ROM. Then, by means of the discrete empirical interpolation method (DEIM), we enhance the efficiency in the assembling of the nonlinear terms, leading to an*hyper*-ROM, which is solved in the *online* phase.

The method of snapshots to perform POD has been introduced by Sirovich [7] and relies on the collection of a series of full-order solutions, performing a singular value decomposition of the set of snapshots, and truncating the resulting left singular vectors set to create the reduced basis.

3.1.1. Proper Orthogonal Decomposition

For non-parametrized time-dependent PDEs, the criteria to choose the snapshots, in order to build a global ROM basis, consists in storing the full order solution at each timestep, namely:

$$\mathbf{S} = [\mathbf{s}_1, \mathbf{s}_2, ..., \mathbf{s}_{N_T}] \in \mathbb{R}^{N_h \times N_T},$$

where $\mathbf{s}_l \in \mathbb{R}^{N_h}$ is the FOM solution at time $t^{(l)}$, $l = 0, ..., N_T$. On the other hand, for parametrized time-dependent PDEs, where multiple evaluations of the solution are required for several values of the parameter $\boldsymbol{\mu} \in \mathcal{P}$, the criteria to choose snapshots involves both the time and parameter dependency, namely:

$$\mathbf{S} = [\mathbf{s}_1(\boldsymbol{\mu}_1), \mathbf{s}_2(\boldsymbol{\mu}_1), ..., \mathbf{s}_1(\boldsymbol{\mu}_2), \mathbf{s}_2(\boldsymbol{\mu}_2), ..., \mathbf{s}_{N_T}(\boldsymbol{\mu}_{N_\mu})] \in \mathbb{R}^{N_h \times (N_T \cdot N_{train})},$$

where $\mathbf{s}_l(\boldsymbol{\mu}_j) \in \mathbb{R}^{N_h}$ is the FOM solution at time $t^{(l)}$, $l = 0, ..., N_T$, for the parameter $\boldsymbol{\mu}_j$. N_{train} indicates the number of parameters $\boldsymbol{\mu}_j$ considered to store the snapshots.
The vector $\mathbf{s}$, in this work, represent the solution of our problems of interest, namely it can be, e.g, the displacement field $\underline{\mathbf{d}}_{h_m}^{(k)}(\boldsymbol{\mu})$, the transmembrane potential $\mathbf{u}_{h_e}^{(l)}(\boldsymbol{\mu})$ or a ionic variable $\mathbf{w}_{h_e}^{(l)}(\boldsymbol{\mu})$. Then, depending on the time discretization considered, N_T can be either N_{t_m}, for the mechanical problem, or N_t, for the electrical problem.
Proper orthogonal decomposition, then, constructs n orthogonal functions $\boldsymbol{\phi}_j \in L^2(\Omega)$ such that the following projection error is minimized:

$$\mathcal{J}(\boldsymbol{\phi}_1, \boldsymbol{\phi}_2, ..., \boldsymbol{\phi}_n) = \sum_{l=1}^{N_{snapshots}} \left\| \mathbf{s}_l - \sum_{j=1}^{n} \langle \mathbf{s}_l, \boldsymbol{\phi}_j \rangle \boldsymbol{\phi}_j \right\|_2^2,$$

where $\langle \cdot, \cdot \rangle$ is the scalar product and the norm is the Euclidean norm.
Moreover, a minimum of the functional $\mathcal{J}$ can be computed through the *Singular Value Decomposition* of the matrix $\mathbf{S}^T\mathbf{S}$ [1] and the reduced basis vectors $\boldsymbol{\phi}_j$ consist in the left singular vectors set [4, 15].
Denoting by $\{\lambda_j\}_{j=1}^{N_{snapshots}}$ the positive eigenvalues of $\mathbf{S}^T\mathbf{S}$ sorted in decreasing order, where $N_{snapshots}$ can be either N_T or $N_T \cdot N_{train}$, the error associated with the minimum of the functional becomes

$$\mathcal{J}(\boldsymbol{\phi}_1, \boldsymbol{\phi}_2, ..., \boldsymbol{\phi}_n) = \sum_{j=n+1}^{N_{snapshots}} \lambda_j.$$

Since each basis vector is associated with a singular value, the singular vectors are ranked in order of importance, so that the $N_{snapshots} - n$ basis vectors associated to small singular values can be removed without losses in solution space approximation.

[1] Since the matrix $\mathbf{S}^T\mathbf{S}$ is a symmetric positive-definite matrix, its *Singular Value Decomposition* consists in its *eigendecomposition*.

In fact, given a POD tolerance $tol_{POD} \ll 1$, n is selected as the smallest dimension s.t. the relative truncation error is smaller than tol_{POD}, namely

$$\frac{\sum_{j=n+1}^{N_{snapshots}} \lambda_j}{\sum_{j=1}^{N_{snapshots}} \lambda_j} < tol_{POD},$$

which can be seen as the following minimization problem:

$$n = \arg\min_k \left(\frac{\sum_{j=1}^{k} \lambda_j}{\sum_{j=1}^{N_{snapshots}} \lambda_j} \geq 1 - tol_{POD} \right),$$

from which we are able to select the dimension of the truncated reduced basis that better approximate the original solution space. Of course, this approximation highly depends on the problem considered. In fact, e.g., for parameter dependent problems, the dimension of the training set N_{train} may influence the singular values decay of the snapshots matrix, and, as a consequence, the dimension of the reduced basis in the ROM approximation. Thus, in such cases, in order to correctly capture the variability of the solution over the parameter space, the dimension of the training should be sufficiently rich. However, more in general, for problems characterized by large parameter variations, different physical regimes, or moving features such as fronts or discontinuities, the singular values decay of the snapshots matrix can be extremely slow, due to the high variability of the solutions stored, and this highly affect the dimensions of the truncated basis when relying on a global ROM strategy as the one presented in this work, in order to approximate the original solution space. In those scenarios, there is the need to rely on different techniques, such as the local reduced-order model presented in [1], which, however, hasn't been exploited in this work.

3.1.2. Global ROM construction for parametrized problems

Solving a parametrized, time-dependent problem for different values of the parameter $\boldsymbol{\mu} \in \mathcal{P}$, at different time-steps, represents a particularly difficult computational task. Thus, relying on RB methods, provides a twofold advantage in this case, since we can construct an efficient numerical approximation which accounts for parameter variations and compute an accurate solution at lower computational costs and memory storage. In this work, we adopt the following scheme to build a global reduced-order model for parametrized problems:

- during the *offline* phase, the parameter domain is explored and, for $N_{\boldsymbol{\mu}}$ different instances of the parameter $\boldsymbol{\mu}$, we compute and store a set of high fidelity solution snapshots, taken at each time-step, for each parameter;
- the set of snapshots stored is used to generate, by means of POD, a low dimensional

global RB space for the solution, namely we have that the dimension is $n \ll N_h$;

- then, during the *online* phase, for each new value of $\boldsymbol{\mu} \in \mathcal{P}$, we solve the reduced model combining the reduced arrays stored *offline*, whose complexity no longer depends on N_h, thus reducing the computational complexity with respect to the FOM.

.

3.2. A reduced-order model for the cardiac electrophysiology subproblem

In order to develop a reduced-order model for the cardiac electrophysiology subproblem, let us write the parametrized version of its full-order model (3.1). Namely: given $\boldsymbol{\mu} \in \mathcal{P}$, find $\mathbf{u}_{h_e}^{(l+1)} = \mathbf{u}_{h_e}^{(l+1)}(\boldsymbol{\mu})$, $\mathbf{w}_{1,h_e}^{(l+1)} = \mathbf{w}_{1,h_e}^{(l+1)}(\boldsymbol{\mu})$, $\mathbf{w}_{2,h_e}^{(l+1)} = \mathbf{w}_{2,h_e}^{(l+1)}(\boldsymbol{\mu})$ and $\mathbf{w}_{3,h_e}^{(l+1)} = \mathbf{w}_{3,h_e}^{(l+1)}(\boldsymbol{\mu})$ such that , for $l = 0, ..., N_t - 1$

$$
\begin{cases}
\dfrac{\mathbf{w}_{1,h_e}^{(l+1)} - \mathbf{w}_{1,h_e}^{(l)}}{\Delta t_e} - \mathbf{F}_{ion,1}(\mathbf{u}_{h_e}^{(l)}, \mathbf{w}_{1,h_e}^{(l+1)}; \boldsymbol{\mu}) = \mathbf{0}, \\
\dfrac{\mathbf{w}_{2,h_e}^{(l+1)} - \mathbf{w}_{2,h_e}^{(l)}}{\Delta t_e} - \mathbf{F}_{ion,2}(\mathbf{u}_{h_e}^{(l)}, \mathbf{w}_{2,h_e}^{(l+1)}; \boldsymbol{\mu}) = \mathbf{0}, \\
\dfrac{\mathbf{w}_{3,h_e}^{(l+1)} - \mathbf{w}_{3,h_e}^{(l)}}{\Delta t_e} - \mathbf{F}_{ion,3}(\mathbf{u}_{h_e}^{(l)}, \mathbf{w}_{3,h_e}^{(l+1)}; \boldsymbol{\mu}) = \mathbf{0}, \\
\mathbf{w}_{1,h_e}^{(0)} = \mathbf{w}_{1,0}(\boldsymbol{\mu}), \mathbf{w}_{2,h_e}^{(0)} = \mathbf{w}_{2,0}(\boldsymbol{\mu}), \mathbf{w}_{3,h_e}^{(0)} = \mathbf{w}_{3,0}(\boldsymbol{\mu}), \\
\\
\mathbf{J}(\boldsymbol{\mu})\boldsymbol{\delta}\mathbf{u}_{h_e} = \mathbf{r}(\mathbf{u}_{h_e,0}^{(l+1)}, \mathbf{w}_{1,h_e}^{(l+1)}, \mathbf{w}_{2,h_e}^{(l+1)}, \mathbf{w}_{3,h_e}^{(l+1)}; (\boldsymbol{\mu})), \\
\mathbf{u}_{h_e}^{(l+1)} = \mathbf{u}_{h_e,0}^{(l+1)} - \boldsymbol{\delta}\mathbf{u}_{h_e}, \quad \mathbf{u}_{h_e,0}^{(l+1)} = \mathbf{u}_{h_e}^{(l)}. \\
\mathbf{u}_{h_e}^{(0)} = \mathbf{u}_0(\boldsymbol{\mu}),
\end{cases}
\tag{3.1}
$$

where we update first the ionic model, Eq.s $(3.1)_{1-4}$, by the fixed point method and then Eq. $(3.1)_{5-7}$, by one iteration of the Newton method, as presented in chaper 2.

3.2.1. POD-Galerkin and hyper-reduction techniques

When aiming at building a ROM for a problem such as (3.1), the nature of the problem leads to a different treatment for the potential variable and the ionic variables, since the former is the solution of a PDE, while the latter varies in space indirectly, due to the dependence on the transmembrane potential. The approximation of $\mathbf{u}_{h_e}(\boldsymbol{\mu})$ can be written as

$$
\mathbf{u}_{h_e}^{(l)}(\boldsymbol{\mu}) \approx \mathbf{V}_u \mathbf{u}_n^{(l)}(\boldsymbol{\mu}),
\tag{3.2}
$$

where the columns of $\mathbf{V}_u \in \mathbb{R}^{N_h \times n_u}$ ($n_u \ll N_h$) are basis functions (*eigenmodes*) obtained by POD, thus $\mathbf{V}_u$ is an orthogonal matrix and takes the name of transformation matrix. The approximation of the ionic variables $\mathbf{w}_{k,h}$, $k = 1, 2, 3$, is instead obtained by evaluating the ODEs only at a subset of mesh nodes, the so called *reduced mesh*, involved in the efficient evaluation of the nonlinear term $\mathbf{I}_{ion}$. In fact, the ionic variables are gappy data and, as we will see later on, in order to reconstruct them over all the domain, at each time, the Gappy POD method can be used instead, which requires anyway a set of basis functions for each ionic variable, similarly to equation (3.2) for the potential.
Hence, assuming that the ionic model has already been updated at time $t^{(l+1)}$ by solving $(3.1)_{1-4}$, the reduced-order model for the monodomain equation is obtained by inserting (3.2) into $(3.1)_5$ and performing a Galerkin projection, which consists in a left projection of the monodomain equation onto the column space of the trasformation matrix $\mathbf{V}_u$, i.e our reduced space for the transmembrane potential. Hence, the Galerkin-RB problem for the increment form of the monodomain equation reads: find $\mathbf{u}_n^{(l+1)} = \mathbf{u}_n^{(l+1)}(\boldsymbol{\mu})$, $l = 0, ..., N_t - 1$, such that

$$\begin{cases} \mathbf{V}_u^T \mathbf{J}(\boldsymbol{\mu}) \mathbf{V}_u \boldsymbol{\delta}\mathbf{u}_n = \mathbf{V}_u^T \mathbf{r}(\mathbf{V}_u \mathbf{u}_{n,0}^{(l+1)}, \mathbf{w}_{1,h_e}^{(l+1)}, \mathbf{w}_{2,h_e}^{(l+1)}, \mathbf{w}_{3,h_e}^{(l+1)}; \boldsymbol{\mu}), \\ \mathbf{u}_n^{(l+1)} = \mathbf{u}_{n,0}^{(l+1)} - \boldsymbol{\delta}\mathbf{u}_n, \quad \mathbf{u}_{n,0}^{(l+1)} = \mathbf{u}_n^{(l)}, \\ \mathbf{u}_n^{(0)} = \mathbf{V}_u^T \mathbf{u}_0, \end{cases} \tag{3.3}$$

However, the residual $\mathbf{r}$, defined in Eq. (2.5), is a nonlinear term, since it requires the assembling of the nonlinear term $\mathbf{I}_{ion}$. Thus, the $\boldsymbol{\mu}$-dependence in this case is nonaffine and the evaluation of the vector, at each time-step, is still performed on the full-order space, compromising the overall ROM efficiency. In order to efficiently evaluate also the nonlinear terms, in this work we rely on the discrete empirical interpolation method (DEIM) [1]. Namely, we interpolate the nonlinear residual over m interpolation points to get its approximate affine expansion at each time step. This leads to the following *hyper-reduced* order model for the increment of the transmembrane potential (for the sake of notation, we will indicate the dependence on the three ionic variables using just one, more general, ionic variable $\mathbf{w}_{h_e}^{(l+1)}$ representing them): find $\mathbf{u}_n^{(l+1)}$, $l = 0, ..., N_t - 1$, such that

$$\begin{cases} \mathbf{V}_u^T \mathbf{J}(\boldsymbol{\mu}) \mathbf{V}_u \boldsymbol{\delta}\mathbf{u}_n = \mathbf{V}_u^T \boldsymbol{\Phi} (\mathbf{P}^T \boldsymbol{\Phi})^{-1} \mathbf{r}(\mathbf{P}^T \mathbf{V}_u \mathbf{u}_{n,0}^{(l+1)}, \mathbf{P}^T \mathbf{w}_{h_e}^{(l+1)}; \boldsymbol{\mu}), \\ \mathbf{u}_n^{(l+1)} = \mathbf{u}_{n,0}^{(l+1)} - \boldsymbol{\delta}\mathbf{u}_n, \quad \mathbf{u}_{n,0}^{(l+1)} = \mathbf{u}_n^{(l)}, \\ \mathbf{u}_n^{(0)} = \mathbf{V}_u^T \mathbf{u}_0. \end{cases} \tag{3.4}$$

The columns of the matrix $\boldsymbol{\Phi} \in \mathbb{R}^{N_{h_e} \times m}$ are the m POD *modes* obtained by applying POD to the snapshot matrix of the nonlinear residual $\mathbf{r}$.
The matrix $\mathbf{P} \in \mathbb{R}^{N_{h_e} \times m}$ is a reduction matrix, defined as $\mathbf{P} = [\mathbf{e}_{\mathcal{I}_1} \mid ... \mid \mathbf{e}_{\mathcal{I}_m}]$, where $\mathbf{e}_{\mathcal{I}_i} = [0, ..., 0, 1, 0, ..., 0]^T \in \mathbb{R}^{N_{h_e}}$ is the $\mathcal{I}_i$-th column of the identity matrix $\mathbf{I} \in \mathbb{R}^{N_{h_e} \times N_{h_e}}$

and $\mathcal{I} \subset \{1, ..., N_{h_e}\}$ is the set of the $|\mathcal{I}| = m$ interpolation indices adopted for the DEIM. The indices are selected iteratively, by a greedy process, through the so-called *magic points* algorithm [1].
The matrix $\mathbf{\Phi}(\mathbf{P}^T\mathbf{\Phi})^{-1}$ can be pre-assembled, enhancing the efficient computation of the nonlinear terms on the m dofs $\mathcal{I}_1, ..., \mathcal{I}_m$ forming the *reduced mesh* (we can indeed consider the matrix $\mathbf{P}$ as a projection matrix onto the *reduced mesh*).
Then, the *hyper-reduced* order model reads: find $\mathbf{u}_n^{(l+1)}$, $\mathbf{w}_{1,h_e}^{(l+1)}$, $\mathbf{w}_{2,h_e}^{(l+1)}$ and $\mathbf{w}_{3,h_e}^{(l+1)}$, for $l = 0, ..., N_t - 1$ such that

$$
\begin{cases}
\mathbf{P}^T \dfrac{\mathbf{w}_{1,h_e}^{(l+1)} - \mathbf{w}_{1,h_e}^{(l)}}{\Delta t_e} - \mathbf{F}_{ion,1}(\mathbf{P}^T\mathbf{V}_u\mathbf{u}_n^{(l)}, \mathbf{P}^T\mathbf{w}_{1,h_e}^{(l+1)}; \boldsymbol{\mu}) = \mathbf{0}, \\
\mathbf{P}^T \dfrac{\mathbf{w}_{2,h_e}^{(l+1)} - \mathbf{w}_{2,h_e}^{(l)}}{\Delta t_e} - \mathbf{F}_{ion,2}(\mathbf{P}^T\mathbf{V}_u\mathbf{u}_n^{(l)}, \mathbf{P}^T\mathbf{w}_{2,h_e}^{(l+1)}; \boldsymbol{\mu}) = \mathbf{0}, \\
\mathbf{P}^T \dfrac{\mathbf{w}_{3,h_e}^{(l+1)} - \mathbf{w}_{3,h_e}^{(l)}}{\Delta t_e} - \mathbf{F}_{ion,3}(\mathbf{P}^T\mathbf{V}_u\mathbf{u}_n^{(l)}, \mathbf{P}^T\mathbf{w}_{3,h_e}^{(l+1)}; \boldsymbol{\mu}) = \mathbf{0}, \\
\\
\mathbf{V}_u^T\mathbf{J}(\boldsymbol{\mu})\mathbf{V}_u\boldsymbol{\delta}\mathbf{u}_n = \mathbf{V}_u^T\mathbf{\Phi}(\mathbf{P}^T\mathbf{\Phi})^{-1}\mathbf{r}(\mathbf{P}^T\mathbf{V}_u\mathbf{u}_{n,0}^{(l+1)}, \mathbf{P}^T\mathbf{w}_{h_e}^{(l+1)}; \boldsymbol{\mu}), \\
\mathbf{u}_n^{(l+1)} = \mathbf{u}_{n,0}^{(l+1)} - \boldsymbol{\delta}\mathbf{u}_n, \quad \mathbf{u}_{n,0}^{(l+1)} = \mathbf{u}_n^{(l)}, \\
\mathbf{u}_n^{(0)} = \mathbf{V}_u^T\mathbf{u}_0.
\end{cases}
\tag{3.5}
$$

The model above represents a very efficient way to solve the coupled monodomain Bueno-Orovio system. However, although the transmembrane potential $\mathbf{u}_{h_e}$ can be obtained by a linear combination of the n_u POD *modes* (columns of $\mathbf{V}_u$) with the ROM solution $\mathbf{u}_n$, on each point of the grid, at each time (cf. equation (3.2)) and for each new instance of the parameter $\boldsymbol{\mu}$, the same procedure is not possible for the ionic variables, which are just evaluated at the points forming the *reduced mesh* and belong only to that subspace.
Nonetheless, the ionic variables, in particular the calcium ion concentration, are directly responsible for the cardiac cell contraction. For this reason, their efficient and accurate evaluation is of crucial importance in the electromechanical coupling, especially in the field of RB methods, since it is of fundamental importance to consider how variations of the parameters in the electrical problem indirectly affects the cardiac contractions in clinical applications.
In the following subsection we introduce a new strategy to approximate the ionic variables, interponing their calculation in the reduced-order framework we have introduced.

3.2.2. Gappy POD for ionic variables reconstruction

Above we have investigated the role of the DEIM in the efficient evaluation of the nonlinear terms included in the monodomain equation. In the DEIM the number of interpolation points corresponds to the dimension m of the reduced space spanned by $\mathbf{\Phi}$, namely the

matrix $\mathbf{P}^T\mathbf{\Phi}$ is a square matrix.
On the other hand, Gappy POD is a ROM technique that considers the case where more sampling points $m > n$ than the dimension n of the reduced space are used, which is indeed the case of gappy data.
Let us consider equations $(3.5)_{1-3}$, namely the *hyper-reduced* system of ODEs regulating ionic variables activation, which returns the ionic variables computed only at the set of m interpolation points forming the *reduced* mesh. Moreover, let us introduce a reduced basis approximation of $\mathbf{w}^{(l)}_{k,h_e} = \mathbf{w}^{(l)}_{k,h_e}(\boldsymbol{\mu})$, given by $\mathbf{w}^{(l)}_{k,h_e} \approx \mathbf{V}_{w_k}\mathbf{w}^{(l)}_{k,n}$, $k = 1, 2, 3$.
Hence, for each ionic variable $\mathbf{w}^{(l+1)}_{k,h_e}$, $k = 1, 2, 3$, we can write the solution of the *hyper-reduced* ionic model $(3.5)_{1-3}$ as follows: for $l = 0, ..., N_t - 1$, we set

$$\mathbf{P}^T\mathbf{w}^{(l+1)}_{k,h_e} \approx \mathbf{P}^T\sum_{i=1}^{n_{w_k}} b_i^{(l+1)}\boldsymbol{\phi}_i = \mathbf{P}^T\mathbf{V}_{w_k}\mathbf{w}^{(l+1)}_{k,n}, \tag{3.6}$$

where $\boldsymbol{\phi}_i$ is a basis function, corresponding to the i-th column of the transformation matrix $\mathbf{V}_{w_k} \in \mathbb{R}^{N_{h_e}\times n_{w_k}}$, obtained by the POD method applied to the snapshots matrix $\mathbf{S}_{w_k}$ of the k-th ionic variable, for each $k = 1, 2, 3$.
The matrix $\mathbf{P}^T\mathbf{V}_{w_k} \in \mathbb{R}^{m\times n_{w_k}}$ is not a squared matrix, since we build the model in such a way that $m > n_{w_k}$ for each k, i.e., the number of points at which the ionic variables are evaluated is larger than the dimension n_{w_k} of the space spanned by the columns of the transformation matrix $\mathbf{V}_{w_k}$. From (3.6), we have that the ROM approximation of the k-th ionic variable at each time $t^{(l+1)}$ is

$$\mathbf{w}^{(l+1)}_{k,n} \approx (\mathbf{P}^T\mathbf{V}_{w_k})^\dagger\mathbf{P}^T\mathbf{w}^{(l+1)}_{k,h_e},$$

which can be reprojected on the full domain, at each time, leading to the following approximation:

$$\mathbf{w}^{(l+1)}_{k,rec} = \mathbf{V}_{w_k}\mathbf{w}^{(l+1)}_{k,n} \approx \mathbf{V}_{w_k}(\mathbf{P}^T\mathbf{V}_{w_k})^\dagger\mathbf{P}^T\mathbf{w}^{(l+1)}_{k,h_e}.$$

where $(\mathbf{P}^T\mathbf{V}_{w_k})^\dagger$ is the Moore-Penrose inverse of $\mathbf{P}^T\mathbf{V}_{w_k}$ and can be efficiently precomputed by using the QR decomposition, namely, given $\mathbf{P}^T\mathbf{V}_{w_k} = \mathbf{Q}_{\mathbf{P}^T\mathbf{V}_{w_k}}\mathbf{R}_{\mathbf{P}^T\mathbf{V}_{w_k}}$, $\mathbf{Q}_{\mathbf{P}^T\mathbf{V}_{w_k}} \in \mathbb{R}^{m\times n}$ and $\mathbf{R}_{\mathbf{P}^T\mathbf{V}_{w_k}} \in \mathbb{R}^{n\times n}$ we have that

$$\mathbf{w}^{(l+1)}_{k,rec} = \mathbf{V}_{w_k}\mathbf{w}^{(l+1)}_{k,n} \approx \mathbf{V}_{w_k}\mathbf{R}^{-1}_{\mathbf{P}^T\mathbf{V}_{w_k}}\mathbf{Q}^T_{\mathbf{P}^T\mathbf{V}_{w_k}}\mathbf{P}^T\mathbf{w}^{(l+1)}_{k,h_e},$$

where $\mathbf{V}_{w_k}\mathbf{R}^{-1}_{\mathbf{P}^T\mathbf{V}_{w_k}}\mathbf{Q}^T_{\mathbf{P}^T\mathbf{V}_{w_k}}$ is precomputed and stored in the *offline* phase.
Hence, when solving the system (3.5), at each time step, for each parameter, we can efficiently evaluate the ionic variables all over the domain by means of the Gappy POD method.

3.2.3. Least square Petrov-Galerkin method

In the subsection 3.2.1 we presented the *POD-Galerkin* approach to develop the reduced-order model (3.3), namely we have applied a Galerkin projection to the increment equation $(3.3)_1$, leading to the following reduced Newton method:

$$\begin{aligned} \mathbf{V}_u^T \mathbf{J} \mathbf{V}_u \boldsymbol{\delta} \mathbf{u}_h &= \mathbf{V}_u^T \mathbf{r}, \\ \mathbf{u}_n^{(l+1)} &= \mathbf{u}_{n,0}^{(l+1)} - \boldsymbol{\delta} \mathbf{u}_n. \end{aligned} \tag{3.7}$$

The Jacobian matrix is assembled in such a way it is symmetric and positive definite, moreover it is assembled only once and just the residuals need to be updated at each time step. As suggested by [4], this leads to seeking optimal solution of equation (3.7), that correspond to the minimum of the following error functional:

$$\boldsymbol{\delta} \mathbf{u}_n = \arg \min_{\mathbf{a} \in \mathbb{R}^{n_u}} \left\| \mathbf{V}_u \mathbf{a} - \mathbf{J}^{-1} \mathbf{r} \right\|_{\boldsymbol{\Theta}}, \tag{3.8}$$

where $\boldsymbol{\Theta} = \mathbf{J}$. However, when the dimension of the column space of $\mathbf{V}_u$ is small, numerical instabilities might affect the solution of the ROM (3.3), due to the nature of the electrophysiology problem, which consists in the propagation of a very steep wave.
In order to reduce the numerical instabilities, a least-squares Petrov-Galerkin (LSPG) approach has been investigated as an alternative to the Galerkin projection in the *offline* phase. The LSPG approach is able to seek an optimal solution to the minimization problem (3.8) even when the Jacobian $\mathbf{J}$ is not SPD, which is often the case when dealing with nonlinear problems [4]. This is because the minimization problem (3.8) corresponds to the normal form of the least squares problem when $\boldsymbol{\Theta} = \mathbf{J}^T \mathbf{J}$:

$$\boldsymbol{\delta} \mathbf{u}_n = \arg \min_{\mathbf{a} \in \mathbb{R}^{n_u}} \left\| \mathbf{J} \mathbf{V}_u \mathbf{a} + \mathbf{r} \right\|_2 = \arg \min_{\mathbf{a} \in \mathbb{R}^{n_u}} \left\| \mathbf{V}_u \mathbf{a} - \mathbf{J}^{-1} \mathbf{r} \right\|_{\mathbf{J}^T \mathbf{J}}, \tag{3.9}$$

so that the reduced Newton method with least-squares Petrov Galerkin projection becomes:

$$\begin{aligned} \mathbf{V}_u^T \mathbf{J}^T \mathbf{J} \mathbf{V}_u \boldsymbol{\delta} \mathbf{u}_h &= -\mathbf{V}_u^T \mathbf{J}^T \mathbf{r}, \\ \mathbf{u}_n^{(l+1)} &= \mathbf{u}_{n,0}^{(l+1)} + \boldsymbol{\delta} \mathbf{u}_n. \end{aligned} \tag{3.10}$$

Similarly to the Gappy POD method, the system (3.10) can be efficiently solved by QR decomposition, namely $\mathbf{J} \mathbf{V}_u = \mathbf{Q}_{\mathbf{J}\mathbf{V}_u} \mathbf{R}_{\mathbf{J}\mathbf{V}_u}$ where $\mathbf{Q}_{\mathbf{J}\mathbf{V}_u} \in \mathbb{R}^{N_h \times n_u}$ and $\mathbf{R}_{\mathbf{J}\mathbf{V}_u} \in \mathbb{R}^{n_u \times n_u}$, leading to an equivalent form of (3.10):

$$\begin{aligned} \mathbf{R}_{\mathbf{J}\mathbf{V}_u} \boldsymbol{\delta} \mathbf{u}_h &= -\mathbf{Q}_{\mathbf{J}\mathbf{V}_u}^T \mathbf{r}, \\ \mathbf{u}_n^{(l+1)} &= \mathbf{u}_{n,0}^{(l+1)} + \boldsymbol{\delta} \mathbf{u}_n. \end{aligned} \tag{3.11}$$

The least-squares Petrov-Galerkin represents a valid alternative to the Galerkin one, even when both the methods lead to optimal solutions as the case in analysis, in order to gain stability and accuracy; this is why it is of interest to study the behavior of ROM with both the approaches. For what concerns the computational costs, we expect the LSPG projection to be slightly less efficient than the Galerkin projection, due to the assembling of the left projection operator $\mathbf{J}\mathbf{V}_u$ and the QR decomposition. However, compared to the FOM, the two approaches represent both an improvement in terms of efficiency, since they are able to seek the solution of the cardiac electrophysiology subproblem on a subspace of much smaller dimensions than the original one.

3.3. A reduced-order model for the cardiac mechanical subproblem

The construction of a ROM for the mechanical subproblem follows a similar approach to the one we exploited in subsection 3.2.1. Namely we consider a POD-Galerkin method to build a first reduced-order model and then we apply the DEIM for the *hyper-reduction*, to efficiently compute the nonlinear terms.

Let us consider the parametrized version of problem (2.13), namely, given $\boldsymbol{\mu} \in \mathcal{P}$, we have that $\underline{\mathbf{d}}_{h_m}^{(k)} = \underline{\mathbf{d}}_{h_m}^{(k)}(\boldsymbol{\mu})$ and $p^{(k)} = p^{(k)}(\boldsymbol{\mu})$. As we have done for the full-order model, due to the interaction of blood with the endocardium, to update the pressure we have to distinguish the problem depending on the related cardiac cycle phase. Namely, in the isovolumetric phases, the parametrized version of the problem becomes: given $\underline{\mathbf{d}}_{h_m}^{(k+1),(0)} = \underline{\mathbf{d}}_{h_m}^{(k)}$ and $p^{(k+1),(0)} = p^{(k)}$ as initial guesses for the Newthon method, for each k such that $t^{(k+1)}$ belongs to an isovolumetric phase, for $j \geq 0$ solve

$$\begin{cases} J_{\mathbf{d},\mathbf{d}}\big(\underline{\mathbf{d}}_{h_m}^{(k+1),(j)}, p^{(k+1),(j)}; \boldsymbol{\mu}\big)\mathbf{v}^{(k+1),(j)}(\boldsymbol{\mu}) = \mathbf{r}_{\mathbf{d}}\big(\underline{\mathbf{d}}_{h_m}^{(k+1),(j)}, p^{(k+1),(j)}; \boldsymbol{\mu}\big), \\ J_{\mathbf{d},\mathbf{d}}\big(\underline{\mathbf{d}}_{h_m}^{(k+1),(j)}, p^{(k+1),(j)}; \boldsymbol{\mu}\big)\mathbf{b}^{(k+1),(j)}(\boldsymbol{\mu}) = J_{\mathbf{d},p}^{(k+1),(j)}(\boldsymbol{\mu}), \\ \delta p^{(k+1),(j)} = \dfrac{p^{(k+1),(j)} - J_{p,\mathbf{d}}^{(k+1),(j)}(\boldsymbol{\mu})\mathbf{v}^{(k+1),(j)}(\boldsymbol{\mu})}{J_{p,\mathbf{d}}^{(l+1),(j)}(\boldsymbol{\mu})\mathbf{b}^{(k+1),(j)}(\boldsymbol{\mu})}, \\ \delta\underline{\mathbf{d}}_{h_m}^{(k+1),(j)} = -(\mathbf{v}^{(k+1),(j)}(\boldsymbol{\mu}) + \mathbf{b}^{(k+1),(j)}(\boldsymbol{\mu})\delta p^{(k+1),(j)}), \\ \underline{\mathbf{d}}_{h_m}^{(k+1),(j+1)} = \underline{\mathbf{d}}_{h_m}^{(k+1),(j)} + \delta\underline{\mathbf{d}}_{h_m}^{(k+1),(j)}, \\ p^{(k+1),(j+1)} = p^{(k+1),(j)} + \delta p^{(k+1),(j)}, \end{cases} \tag{3.12}$$

until $\left\|\mathbf{r}_{\mathbf{d}}^{(k+1),(j)}\big(\underline{\mathbf{d}}_{h_m}(\boldsymbol{\mu}), p^{(k+1),(j)}(\boldsymbol{\mu})\big)\right\|_2 < \epsilon$, for ϵ sufficiently small, and $j \leq N_{iter}^{max}$, where j is the index of the Newton iteration.

For the other two phases, where the pressure is updated before solving Eq. (2.13), the parametrized version reads: given $\underline{\mathbf{d}}_{h_m}^{(k+1),(0)} = \underline{\mathbf{d}}_{h_m}^{(k)}$ as initial guess of the Newthon method at each iteration, for each k such that $t^{(k+1)}$ belongs to the ejection or the filling phase,

for $j \geq 0$ solve

$$\begin{cases} J_{\mathbf{d},\mathbf{d}}\big(\underline{\mathbf{d}}_{h_m}^{(k+1),(j)};\boldsymbol{\mu}\big)\delta\underline{\mathbf{d}}_{h_m}^{(k+1),(j)} = -\mathbf{r}_{\mathbf{d}}\big(\underline{\mathbf{d}}_{h_m}^{(k+1),(j)};\boldsymbol{\mu}\big), \\ \underline{\mathbf{d}}_{h_m}^{(k+1),(j+1)} = \underline{\mathbf{d}}_{h_m}^{(k+1),(j)} + \delta\underline{\mathbf{d}}_{h_m}^{(k+1),(j)}, \end{cases} \tag{3.13}$$

until $\left\|\mathbf{r}_{\mathbf{d}}^{(k+1),(j)}(\boldsymbol{\mu})\right\|_2 < \epsilon$ and $j \leq N_{iter}^{max}$, where j is the index of the Newton iteration. Here, it is important to point out that, in the construction of the ROM for the cardiac mechanics, we adopt a global reduced basis, built by means of a POD over a snapshots matrix that consider snapshots of the displacement from all the sequential phases of the cardiac cycle, for each parameter. Thus, we assume there is not a distinction between the different phases, since they mainly affect the evolution of the pressure p and the left ventricle volume V, and only indirectly the displacement field. Moreover, the passage from a phase of the cardiac cycle to the sequent phase is only due to the values of the pressure on the endocardium Γ_0^{endo} and how we model its evolution in time, as we have seen in Eq. (1.18), but it doesn't modify the way we model the cardiac deformation.

3.3.1. POD-Galerkin and hyper-reduction techniques

The approximation of $\underline{\mathbf{d}}_{h_m}^{(k+1)}(\boldsymbol{\mu})$, $\forall k = 0, ..., N_{t_m} - 1$ can be written as

$$\underline{\mathbf{d}}_{h_m}^{(k+1)}(\boldsymbol{\mu}) \approx \mathbf{V}_{\mathbf{d}}\underline{\mathbf{d}}_n^{(k+1)}(\boldsymbol{\mu}), \tag{3.14}$$

where the columns of the transformation matrix $\mathbf{V}_d \in \mathbb{R}^{N_d \times n_d}$ ($n_d \ll N_d$) are the orthonormal basis functions obtained by proper orthogonal decomposition over the snapshots matrix for the displacement.
Substituting (3.14) in problem (3.12), and performing a Galerkin projection, we thus obtain: given $\underline{\mathbf{d}}_n^{(k+1),(0)} = \underline{\mathbf{d}}_n^{(k)}$ and $p^{(k+1),(0)} = p^{(k)}$, for each k such that $t^{(k+1)}$ belong to an isovolumetric phase, for $j \geq 0$ solve

$$\begin{cases} \mathbf{V}_{\mathbf{d}}^T J_{\mathbf{d},\mathbf{d}}\big(\mathbf{V}_{\mathbf{d}}\underline{\mathbf{d}}_n^{(k+1),(j)}, p^{(k+1),(j)};\boldsymbol{\mu}\big)\mathbf{V}_{\mathbf{d}}\mathbf{v}_n^{(k+1),(j)}(\boldsymbol{\mu}) = \\ \qquad\qquad \mathbf{V}_{\mathbf{d}}^T\mathbf{r}_{\mathbf{d}}\big(\mathbf{V}_{\mathbf{d}}\underline{\mathbf{d}}_n, p^{(k+1),(j)};\boldsymbol{\mu}\big), \\ \mathbf{V}_{\mathbf{d}}^T J_{\mathbf{d},\mathbf{d}}\big(\mathbf{V}_{\mathbf{d}}\underline{\mathbf{d}}_n^{(k+1),(j)}, p^{(k+1),(j)};\boldsymbol{\mu}\big)\mathbf{V}_{\mathbf{d}}\mathbf{b}_n^{(k+1),(j)}(\boldsymbol{\mu}) = \\ \qquad\qquad \mathbf{V}_{\mathbf{d}}^T J_{\mathbf{d},p}^{(k+1),(j)}(\boldsymbol{\mu}), \\ \delta p^{(k+1),(j)} = \dfrac{p^{(k+1),(j)} - \mathbf{V}_{\mathbf{d}}^T J_{p,\mathbf{d}}^{(k+1),(j)}(\boldsymbol{\mu})\mathbf{V}_{\mathbf{d}}\mathbf{v}_n^{(k+1),(j)}(\boldsymbol{\mu})}{\mathbf{V}_{\mathbf{d}}^T J_{n,p,\mathbf{d}}^{(k+1),(j)}(\boldsymbol{\mu})\mathbf{V}_{\mathbf{d}}\mathbf{b}_n^{(k+1),(j)}(\boldsymbol{\mu})}, \\ \delta\underline{\mathbf{d}}_n^{(k+1),(j)} = -(\mathbf{v}_n^{(k+1),(j)}(\boldsymbol{\mu}) + \mathbf{b}_n^{(k+1),(j)}(\boldsymbol{\mu})\delta p^{(k+1),(j)}), \\ \underline{\mathbf{d}}_n^{(k+1),(j+1)} = \underline{\mathbf{d}}_n^{(k+1),(j)} + \delta\underline{\mathbf{d}}_n^{(k+1),(j)}, \\ p^{(k+1),(j+1)} = p^{(k+1),(j)} + \delta p^{(k+1),(j)}, \end{cases} \tag{3.15}$$

until $\left\|\mathbf{r}_{\mathbf{d}}^{(k+1),(j)}(\boldsymbol{\mu})\right\|_2 < \epsilon$, for ϵ sufficiently small, and $j \leq N_{iter}^{max}$, where $\mathbf{v}_n^{(k+1),(j)}(\boldsymbol{\mu}) = \mathbf{V}_{\mathbf{d}}^T\mathbf{v}^{(k+1),(j)}(\boldsymbol{\mu})$ and $\mathbf{b}_n^{(k+1),(j)}(\boldsymbol{\mu}) = \mathbf{V}_{\mathbf{d}}^T\mathbf{b}^{(k+1),(j)}(\boldsymbol{\mu})$ are the projections of $\mathbf{v}^{(k+1),(j)}(\boldsymbol{\mu})$ and $\mathbf{b}^{(k+1),(j)}(\boldsymbol{\mu})$ on the reduced space generated by the basis functions for the displacement field, respectively.
We substitute Eq. (3.14) also in (3.13) and, performing a Galerkin projection onto $\mathbf{V}_d$, we obtain the followin Galerkin-RB problem: given $\underline{\mathbf{d}}_n^{(k+1),(0)}(\boldsymbol{\mu}) = \underline{\mathbf{d}}_n^{(k)}(\boldsymbol{\mu})$, for each k such that $t^{(k+1)}$ belong to the ejection or the filling phase, for $j \geq 0$ solve

$$\begin{cases} \mathbf{V}_{\mathbf{d}}^T J_{\mathbf{d},\mathbf{d}}\big(\mathbf{V}_{\mathbf{d}}\underline{\mathbf{d}}_n^{(k+1),(j)};\boldsymbol{\mu}\big)\mathbf{V}_{\mathbf{d}}\delta\underline{\mathbf{d}}_n^{(k+1),(j)} = -\mathbf{V}_{\mathbf{d}}^T\mathbf{r}_{\mathbf{d}}\big(\mathbf{V}_{\mathbf{d}}\underline{\mathbf{d}}_n^{(k+1),(j)};\boldsymbol{\mu}\big), \\ \underline{\mathbf{d}}_n^{(k+1),(j+1)} = \underline{\mathbf{d}}_n^{(k+1),(j)} + \delta\underline{\mathbf{d}}_n^{(k+1),(j)}, \end{cases} \tag{3.16}$$

until $\left\|\mathbf{r}_{\mathbf{d}}^{(k+1),(j)}(\boldsymbol{\mu})\right\|_2 < \epsilon$ and $j \leq N_{iter}^{max}$.
At this stage of the mechanical reduce-order model, the nonlinear residual $\mathbf{r_d}$ and, as a consequence, the jacobian matrix $J_{\mathbf{d},\mathbf{d}}$ are still assembled at each time, for each Newton iteration, on the original FOM space and then projected on the reduced space, thus limiting the efficiency of the ROM. As we have done for the cardiac electrophysiology ROM, in order to efficiently assemble those terms, we rely on the discrete empirical interpolation method (DEIM). Namely, by collecting snapshots of the nonlinear residual $\mathbf{r_d}$ at each time-step and for each parameter instance $\boldsymbol{\mu} \in \mathcal{P}$, and by applying proper orthogonal decomposition to the obtained snapshots matrix, we compute the transformation matrix $\boldsymbol{\Phi}_{\mathbf{d}} \in \mathbb{R}^{N_d \times m_d}$. We then introduce the restriction matrix $\mathbf{P}_{\mathbf{d}} \in \mathbb{R}^{N_d \times m_d}$, which is a projection matrix onto the *reduced mesh* formed by the m_d interpolation indices adopted for the DEIM. Hence, we can approximate the nonlinear terms in an efficient way as follows

$$\begin{aligned} \mathbf{r}_{\mathbf{d}}\big(\mathbf{V}_{\mathbf{d}}\underline{\mathbf{d}}_n^{(k+1),(j)}(\boldsymbol{\mu}), p^{(k+1),(j)}(\boldsymbol{\mu})\big) \approx \\ \boldsymbol{\Phi}_{\mathbf{d}}\big(\mathbf{P}_{\mathbf{d}}^T\boldsymbol{\Phi}_{\mathbf{d}}\big)^{-1}\mathbf{r}_{\mathbf{d}}\big(\mathbf{P}_{\mathbf{d}}^T\mathbf{V}_{\mathbf{d}}\underline{\mathbf{d}}_n^{(k+1),(j)}(\boldsymbol{\mu}), p^{(k+1),(j)}(\boldsymbol{\mu})\big), \\ J_{\mathbf{d},\mathbf{d}}\big(\mathbf{V}_{\mathbf{d}}\underline{\mathbf{d}}_n^{(k+1),(j)}(\boldsymbol{\mu}), p^{(k+1),(j)}(\boldsymbol{\mu})\big) \approx \\ \boldsymbol{\Phi}_{\mathbf{d}}\big(\mathbf{P}_{\mathbf{d}}^T\boldsymbol{\Phi}_{\mathbf{d}}\big)^{-1}J_{\mathbf{d},\mathbf{d}}\big(\mathbf{P}_{\mathbf{d}}^T\mathbf{V}_{\mathbf{d}}\underline{\mathbf{d}}_n^{(k+1),(j)}(\boldsymbol{\mu}), p^{(k+1),(j)}(\boldsymbol{\mu})\big). \end{aligned} \tag{3.17}$$

For the sake of notation, let us rewrite the terms $J_{\mathbf{d},\mathbf{d}}\big(\mathbf{P}_{\mathbf{d}}^T\mathbf{V}_{\mathbf{d}}\underline{\mathbf{d}}_n^{(k+1),(j)}(\boldsymbol{\mu}), p^{(k+1),(j)}(\boldsymbol{\mu})\big) \in \mathbb{R}^{m_d \times N_d}$ and $\mathbf{r}_{\mathbf{d}}\big(\mathbf{P}_{\mathbf{d}}^T\mathbf{V}_{\mathbf{d}}\underline{\mathbf{d}}_n^{(k+1),(j)}(\boldsymbol{\mu}), p^{(k+1),(j)}(\boldsymbol{\mu})\big) \in \mathbb{R}^{m_d}$ as follows:

$$\begin{aligned} \widetilde{J}_{\mathbf{d},\mathbf{d}}^{(k+1),(j)}(\boldsymbol{\mu}) = J_{\mathbf{d},\mathbf{d}}\big(\mathbf{P}_{\mathbf{d}}^T\mathbf{V}_{\mathbf{d}}\underline{\mathbf{d}}_n^{(k+1),(j)}(\boldsymbol{\mu}), p^{(k+1),(j)}(\boldsymbol{\mu})\big), \\ \widetilde{\mathbf{r}}_{\mathbf{d}}^{(k+1),(j)}(\boldsymbol{\mu}) = \mathbf{r}_{\mathbf{d}}\big(\mathbf{P}_{\mathbf{d}}^T\mathbf{V}_{\mathbf{d}}\underline{\mathbf{d}}_n^{(k+1),(j)}(\boldsymbol{\mu}), p^{(k+1),(j)}(\boldsymbol{\mu})\big) \end{aligned}$$

Moreover the left projection matrix $\boldsymbol{\Phi}_{\mathbf{d}}\big(\mathbf{P}_{\mathbf{d}}^T\boldsymbol{\Phi}_{\mathbf{d}}\big)^{-1}$ can be pre-assembled, reducing the computational cost related to the assembling of the nonlinear terms on the *reduced mesh*.

The approximation of the nonlinear terms by DEIM allows us to write the *hyper-reduced* form of problems (3.15) and (3.16), which correspond to the mechanical reduced-order model solved during the *online* phase, for each new instance of the parameter $\boldsymbol{\mu} \in \mathcal{P}$. In particular, for the isovolumetric phases, the *hyper*-ROM reads as follow: given $\underline{\mathbf{d}}_n^{(k+1),(0)} = \underline{\mathbf{d}}_n^{(k)}$ and $p^{(k+1),(0)} = p^{(l)}$, for each k such that $t^{(k+1)}$ belong to an isovolumetric phase, for $j \geq 0$ solve

$$\begin{cases} \mathbf{V}_\mathbf{d}^T \boldsymbol{\Phi}_\mathbf{d} \left(\mathbf{P}_\mathbf{d}^T \boldsymbol{\Phi}_\mathbf{d}\right)^{-1} \widetilde{J}_{\mathbf{d},\mathbf{d}}^{(k+1),(j)}(\boldsymbol{\mu}) \mathbf{V}_\mathbf{d} \mathbf{v}_n^{(k+1),(j)}(\boldsymbol{\mu}) = \\ \qquad\qquad\qquad\qquad \mathbf{V}_\mathbf{d}^T \boldsymbol{\Phi}_\mathbf{d} \left(\mathbf{P}_\mathbf{d}^T \boldsymbol{\Phi}_\mathbf{d}\right)^{-1} \widetilde{\mathbf{r}}_\mathbf{d}^{(k+1),(j)}(\boldsymbol{\mu}), \\ \mathbf{V}_\mathbf{d}^T \boldsymbol{\Phi}_\mathbf{d} \left(\mathbf{P}_\mathbf{d}^T \boldsymbol{\Phi}_\mathbf{d}\right)^{-1} \widetilde{J}_{\mathbf{d},\mathbf{d}}^{(k+1),(j)}(\boldsymbol{\mu}) \mathbf{V}_\mathbf{d} \mathbf{b}_n^{(k+1),(j)}(\boldsymbol{\mu}) = \\ \qquad\qquad\qquad\qquad \mathbf{V}_\mathbf{d}^T J_{\mathbf{d},p}^{(k+1),(j)}(\boldsymbol{\mu}), \\ \delta p^{(k+1),(j)} = \dfrac{p^{(k+1),(j)} - \mathbf{V}_\mathbf{d}^T J_{p,\mathbf{d}}^{(k+1),(j)}(\boldsymbol{\mu}) \mathbf{V}_\mathbf{d} \mathbf{v}_n^{(k+1),(j)}(\boldsymbol{\mu})}{\mathbf{V}_\mathbf{d}^T J_{n,p,\mathbf{d}}^{(k+1),(j)}(\boldsymbol{\mu}) \mathbf{V}_\mathbf{d} \mathbf{b}_n^{(l+1),(j)}(\boldsymbol{\mu})}, \\ \delta \underline{\mathbf{d}}_n^{(k+1),(j)} = -(\mathbf{v}_n^{(k+1),(j)}(\boldsymbol{\mu}) + \mathbf{b}_n^{(k+1),(j)}(\boldsymbol{\mu}) \delta p^{(k+1),(j)}), \\ \underline{\mathbf{d}}_n^{(k+1),(j+1)} = \underline{\mathbf{d}}_n^{(k+1),(j)} + \delta \underline{\mathbf{d}}_n^{(k+1),(j)}, \\ p^{(k+1),(j+1)} = p^{(k+1),(j)} + \delta p^{(k+1),(j)}, \end{cases} \tag{3.18}$$

until $\left\| \widetilde{\mathbf{r}}_\mathbf{d}^{(k+1),(j)}(\boldsymbol{\mu}) \right\|_2 < \epsilon$ and $j \leq N_{iter}^{max}$.
For the remaining two phases of the considered cardiac cycle, the *hyper*-ROM reads: given $\underline{\mathbf{d}}_n^{(k+1),(0)}(\boldsymbol{\mu}) = \underline{\mathbf{d}}_n^{(k)}(\boldsymbol{\mu})$, for each l such that $t^{(k+1)}$ belong to the ejection or the filling phase, for $j \geq 0$ solve

$$\begin{cases} \mathbf{V}_\mathbf{d}^T \boldsymbol{\Phi}_\mathbf{d} \left(\mathbf{P}_\mathbf{d}^T \boldsymbol{\Phi}_\mathbf{d}\right)^{-1} \widetilde{J}_{\mathbf{d},\mathbf{d}}^{(k+1),(j)}(\boldsymbol{\mu}) \mathbf{V}_\mathbf{d} \delta \underline{\mathbf{d}}_n^{(k+1),(j)} = \\ \qquad\qquad\qquad\qquad -\mathbf{V}_\mathbf{d}^T \boldsymbol{\Phi}_\mathbf{d} \left(\mathbf{P}_\mathbf{d}^T \boldsymbol{\Phi}_\mathbf{d}\right)^{-1} \widetilde{\mathbf{r}}_\mathbf{d}^{(k+1),(j)}(\boldsymbol{\mu}), \\ \underline{\mathbf{d}}_n^{(k+1),(j+1)} = \underline{\mathbf{d}}_n^{(k+1),(j)} + \delta \underline{\mathbf{d}}_n^{(k+1),(j)}, \end{cases} \tag{3.19}$$

until $\left\| \widetilde{\mathbf{r}}_\mathbf{d}^{(k+1),(j)}(\boldsymbol{\mu}) \right\|_2 < \epsilon$ and $j \leq N_{iter}^{max}$.
Hence, the two hyper-reduced models presented, which varies only in the way the pressure is updated in the different cardiac cycle phases, represent a very efficient way to solve the cardiac mechanics problem. As we have seen in section 3.2.1 for the transmembrane potential, the ROM approximation of the displacement field $\underline{\mathbf{d}}_{h_m}$ can be obtained by a linear combination of the n_d basis functions (columns of $\mathbf{V}_d$) with the *online* ROM solution $\underline{\mathbf{d}}_{h_m}$ at each times-step, for each new instance of $\boldsymbol{\mu} \in \mathcal{P}$.

3.4. A reduced-order model for the one-way coupled electromechanical problem

The reduced-order model for the one-way coupled electromechanical problem is obtained by coupling the two ROMs for cardiac electrophysiology and cardiac mechanics introduced in this chapter. As we anticipated in section 1.3, in this work we are considering a one-way coupled electromechanical model, thus, solving the electromechanical ROM considered consists in solving first the ROM for the electrophysiology subproblem and then the ROM for the mechanical subproblem, where the active part depends at each time-step by the intracellular calcium concentration through the activation model presented in Eq. (1.10). The *online* phase of the electromechanical model is thus solved as follows: given $\mathbf{u}_{h_e}^{(0)} = \mathbf{u}_0$, $\mathbf{w}_{1,h_e}^{(0)} = \mathbf{w}_{1,0}$, $\mathbf{w}_{2,h_e}^{(0)} = \mathbf{w}_{2,0}$, $\mathbf{w}_{3,h_e}^{(0)} = \mathbf{w}_{3,0}$ and $T_{a,h_m}^{(0)} = T_{a,0}, \underline{\mathbf{d}}_{h_m}^{(0)} = \underline{\mathbf{d}}_{0,h_m}$, $\underline{\mathbf{d}}_{h_m}^{(1)} = \underline{\mathbf{d}}_{0,h_m} + \Delta t_m \dot{\underline{\mathbf{d}}}_{0,h_m}$

- by an intergrid map, we interpolate the efficiently computed ionic variable $\mathbf{w}_{3,rec}^{(l+1)}$, representing the intracellular calcium dynamic, from $\mathcal{T}_{h_e}$ to $\mathcal{T}_{h_m}$, to obtain $\mathbf{w}_{3,h_m}^{(l+1)}$, for $l = 0, ..., N_t - 1$. In fact, due to the propagation of a very steep front, cardiac electrophysiology needs to be solved on a finer mesh, $\mathcal{T}_{h_e}$, with respect to the coarser one, $\mathcal{T}_{h_m}$, used for the mechanics problem, namely we considered two refinement steps of the initial grid for the former and no refinement steps for the latter;
- we then find $\underline{\mathbf{d}}_{h_m}^{(k+1)}$, for each $k = 0, ..., N_{t_m} - 1$, solving the *online* phase of the cardiac mechanics ROM subproblem, namely either (3.18) or (3.19), depending on the value of the pressure on the endocardium, i.e. depending on the phases of the cardiac cycle. The active part of (3.18) and (3.19) is assembled by evaluating, at each time-step k, the active tension $T_{a,h_m}^{(k+1)}$ through the activation model (2.12), where $\mathbf{w}_{3,h_m}^{q\cdot(l+1)} = \mathbf{w}_{3,h_m}^{(k+1)}$ is the intracellular calcium concentration, evaluated at the time intervals considered for the discretization of the mechanical problem, which determines the electromechanical coupling.

We remark that the one-way coupled electromechanical ROM presented in this work can efficiently simulate how the electrical propagation affetcs the cardiac deformations under parameter variations, coming either from the electrical subproblem and/or from the mechanical one. This is of fundamental importance when we consider clinical applications of such model, where the solutions are highly dependent on parameter variations, due to the inter-patient variability, and for which, relying on the full order methods, represent an almost infeasible task, for the too demanding computational costs.

4 | Efficient evaluation of ionic variables in cardiac electrophysiology

In this chapter, we investigate the numerical performances of the RB methods for cardiac electrophysiology, looking at efficiency and accuracy in the development of the ROM and, in particular, the accuracy in the reconstruction of the ionic variables in all the domain at each time. We are going to compare the two different approaches adopted in the construction of the ROM in the *offline* phase, namely the Galerkin projection and the least-squares Petrov-Galerkin, and how they affect the goodness of the solutions in the *online* phase. The numerical simulations have been performed on a high performance computer equipped with a Intel Xeon CPU E5-2640v4, 2.40GHz and 64 GB RAM.

4.1. Setting

Recalling what seen in chapter 3, the *offline* phase for the construction of a parametrized electrophysiology ROM consists in the following consecutive steps:

- Step 1: Solve the FOM, Eq. (3.1), for N_{train} training parameters, to save snapshots of the transmembrane potential and the ionic variables in time, for each parameter $\boldsymbol{\mu}_j, j = 1, ..., N_{train}$, from which the transformation matrices $\mathbf{V}_u$, $\mathbf{V}_{w_1}$, $\mathbf{V}_{w_2}$, $\mathbf{V}_{w_3}$ are computed by means of proper orthogonal decomposition;
- Step 2: solve a first non *hyper*-ROM, descrived by (3.3), for $N_{train-ROM}$ parameters, and save snapshots of the residual $\mathbf{r}$ in time, for each parameter $\boldsymbol{\mu}_j$, $j = 1, ..., N_{train-ROM}$, to construct the transformation matrix $\boldsymbol{\Phi}$ through POD;
- Step 3: assemble and store the left projection matrices for the DEIM and the Gappy POD method to develop the *hyper-reduction*.

Then, in the *online* phase (*POD-Gaklerkin-DEIM phase*), the ROM is built to efficiently approximate the problem solution, assembling the non-linear terms on the *reduced mesh* and solving the *hyper-reduced* system (3.5), for each new instance of the parameter $\boldsymbol{\mu} \in \mathcal{P}$. To compute the accuracy of the *hyper*-ROM approximations for the potential and the ionic

variables, the following mean relative error is adopted ($\mathbf{g}$ is a generic variable representing either the transmembrane potential or a ionic variable):

$$err_g = mean_{t\in(0,T)} \frac{\left\|\mathbf{g}_h(t;\mathbf{x}) - \mathbf{V}_g^T \mathbf{g}_n(t;\mathbf{x})\right\|_2}{\|\mathbf{g}_h(t;\mathbf{x})\|_2}, \tag{4.1}$$

namely, at each time-step, not considering the initial one, the relative error for a vector of the solution evolving in space with respect to the FOM solution is computed and then the mean over all the time-steps is taken.

4.2. Test 1: Evaluation of ionic variables on a slab domain

As first test case, we consider a three-dimensional monodomain model, which describes the behavior of the transmembrane potential and the ionic variables over a slab of the myocardial tissue, $\Omega_0 = (0, 0.05) \times (0, 0.001) \times (0, 0.05)\ \ m^3$.
For the mesh $\mathcal{T}_{h_e}$, two global refinement steps have been applied to the initial grid, leading to 156800 cells and $N_{h_e} = 197985$ dofs, in order to have a more realistic and less mesh depending travelling wave.
The accuracy of the Gappy POD method in the approximation of the ionic variables and the investigation of the performances for the two approaches POD-Galerkin and POD least-squares Petrov-Galerkin in the construction of the ROM are considered first for a non-parametrized electrophysiology problem. Namely, the train and the test in the *offline* and *online* phases have been performed on the same instance of the conductivity coefficients. In fact, in this first case tested, the conductivity tensor is fixed and reads:

$$\mathbf{D}(\mathbf{x}) = \sigma_m^t \mathbf{1} + (\sigma_m^l - \sigma_m^t)\mathbf{f}_0 \otimes \mathbf{f}_0 + (\sigma_m^n - \sigma_m^t)\mathbf{n}_0 \otimes \mathbf{n}_0,$$

with $\sigma_m^l = 1.5 \cdot 10^{-4}\ m^2/s$, $\sigma_m^t = 7 \cdot 10^{-5}\ m^2/s$ and $\sigma_m^n = 4 \cdot 10^{-5}\ m^2/s$ for the longitudinal, transversal and normal conductivity coefficients respectively. These values provide a propagation velocity of 0.75 m/s along the fibers direction, 0.62 m/s in the transversal direction and 0.54 m/s along the normal direction.
In figure 4.1, we report the computational mesh $\mathcal{T}_{h_e}$ and the fibers vector field considered over the slab domain.
The applied current consists in a Gaussian impulse set in the corner $(0.0, 0.0, 0.05)$ and reads as:

$$I_{app}(\mathbf{x}, t) = 400 exp\Big(- \frac{x_1^2 + x_2^2 + x_3^2}{0.005}\Big)\mathbf{I}_{[0,0.003s]}(t),$$

where $\mathbf{I}$ is the indicator function.
The ionic model is the Bueno-Orovio model, presented in section (1.1.2), however, the

methods introduced and the relative implementations work fine also for other ionic models, such as the Aliev-Panfilov or the FitzHugh Nagumo model.
As time interval, we consider the interval $(0, T)$, $T = 120\ ms$, with a time step $\Delta t_e = 10^{-4} s$, which is able to catch both the depolarization and the start of the repolarization of the cardiac membrane, meaning that the propagation of the steep wave generated by the impulse reaches the whole domain and begins to dissipate in the last 20ms.

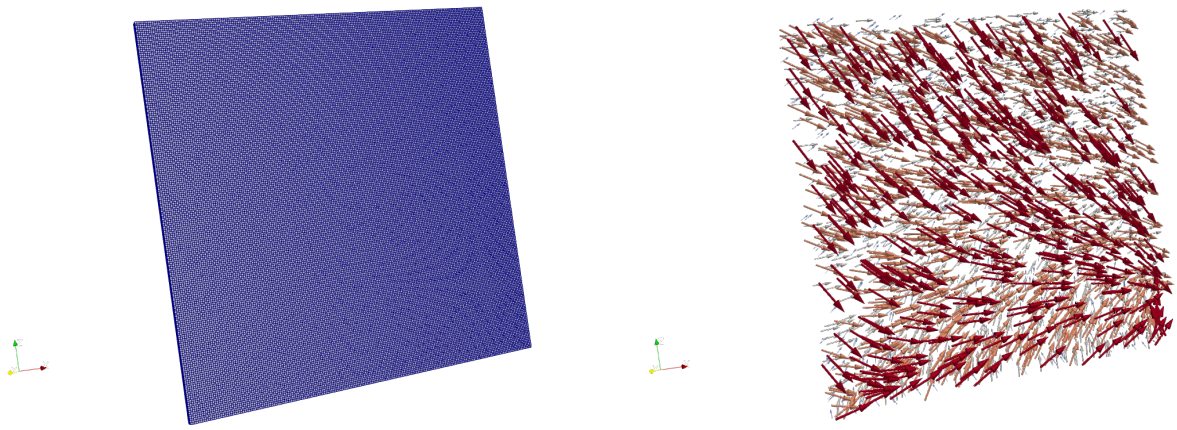

Figure 4.1: Computational mesh ($\mathcal{T}_{h_e}$) over the slab domain (left) and fibers field (right).

4.2.1. Dimension of POD spaces varying the POD tolerance

As seen in subsection 3.1.1, the dimensions of the reduced basis, for each variable, depends on the value of the POD tolerance used. To evaluate the accuracy of the ROM, the tests are performed varying the dimension of the reduced basis. In table (4.1), for each variable, we have the RB dimension corresponding to the respective POD tolerance adopted for the simulations, which are $tol_{POD} = 10^{-1}$, 10^{-2} and 10^{-3}:

tol_{POD}	10^{-1}	10^{-2}	10^{-3}
n_u	18	151	339
n_{w_1}	10	68	369
n_{w_2}	1	2	9
n_{w_3}	8	43	150
m	600	986	1078

Table 4.1: Number of eigenmodes obtained by the POD method for the different variables adopted in the two approaches varying the POD tolerance. The dimension m of the nonlinear term's reduced basis is obtained using $tol_{POD} = 10^{-5}$ in all the three cases.

For what concerns the reduced-order representation of the nonlinear term, it is built through POD using a POD tolerance fixed to 10^{-5} in all the case tested. The value is

lower than the values adopted for the potential and the ionic variables in order to retain stability; in fact, the number of bases m, corresponding also to the number of $dofs$ adopted for the DEIM and forming the *reduced mesh*, should be higher than the number of basis functions for the variables, mainly to avoid ill-conditioning of the matrices of the form $\mathbf{P}^T\mathbf{V}$ when considering the Gappy POD method.

4.2.2. Numerical results

In table 4.2 the relative errors related to the ROM built using a *POD-Galerkin* approach are displayed. As we can see from table 4.1, for a high POD tolerance, the dimensions of the reduced bases are small, leading to low-quality approximations of the variables and high relative errors. This is due to the fact that there are not enough basis elements able to represent all the characteristics of the spaces of expected solutions when the POD tolerance for the proper orthogonal decomposition for the variables is high. This is often the case when a global ROM is adopted to approximate stiff problems like the monodomain model, characterized by the propagation of a very steep front. However,

Relative errors using Galerkin projection	POD tolerance		
	10^{-1}	10^{-2}	10^{-3}
err_{u-POD}	1.00	$3.62{\cdot}10^{-1}$	$1.46{\cdot}10^{-2}$
$\text{err}_{u-PODDEIM}$	1.00	$3.82{\cdot}10^{-1}$	$2.76{\cdot}10^{-2}$
$\text{err}_{w1-Gappy}$	1.54	$2.56{\cdot}10^{-1}$	$1.08{\cdot}10^{-2}$
$\text{err}_{w2-Gappy}$	$1.78{\cdot}10^{-1}$	$1.11{\cdot}10^{-2}$	$8.79{\cdot}10^{-4}$
$\text{err}_{w3-Gappy}$	$9.71{\cdot}10^{-1}$	$2.9{\cdot}10^{-1}$	$9.81{\cdot}10^{-3}$

Table 4.2: Relative errors for the transmembrane potential and the ionic variables when building the ROM with the *POD-Galerkin* approach.

by increasing the dimensions of the reduced basis for the variables, it is possible to see a remarkable improvement in the approximations, while still having a great reduction of the dimension N_{h_e} of the original space and a lowering of the computational costs with respect to the full order model (cf. figure 4.8).
In figures 4.2 and 4.3 we can see a snapshot at 60ms of the transmembrane potential and the ionic variables, from the FOM solution to the one of the *hyper-reduced* model. In particular, the approximation obtained using a $tol_{POD} = 10^{-1}$, which is low-quality due to the low number of bases adopted for the reduction, is shown in figure 4.2. The same snapshot at 60ms, using a $tol_{POD} = 10^{-3}$, which leads to higher dimensions of the reduced spaces for the approximation, is shown in figure 4.3. We can see how the reconstruction of the ionic variables by Gappy POD method and the transmembrane potential computed by the *hyper*-ROM (3.5) are perfectly comparable to the ones obtained by the FOM, at lower computational costs, as it is shown in figure 4.8, and lower memory storage.

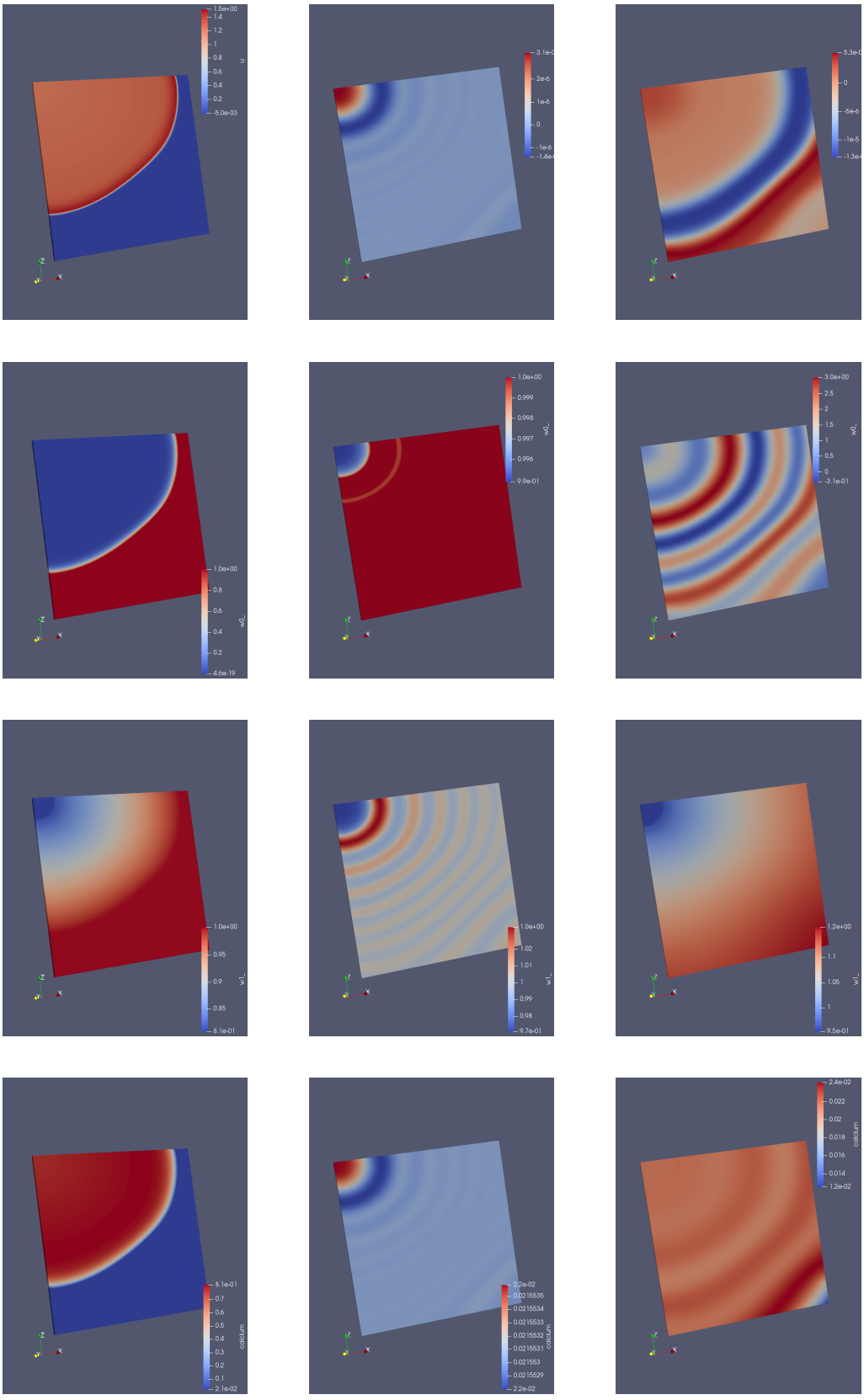

Figure 4.2: Snapshots of the transmembrane potential (first row) and the ionic variables (from the second row to the last one, w_1, w_2,w_3 rispectively) at 60ms in the POD-Galerkin ROM and $PODtol = 10^{-1}$. Left: FOM solutions; center: solutions of the POD-Galerkin ROM without *hyper-reduction*; right: solutions of the hyper-ROM model with Gappy POD reconstruction of the ionic variables (*POD-Galerkin-DEIM*).

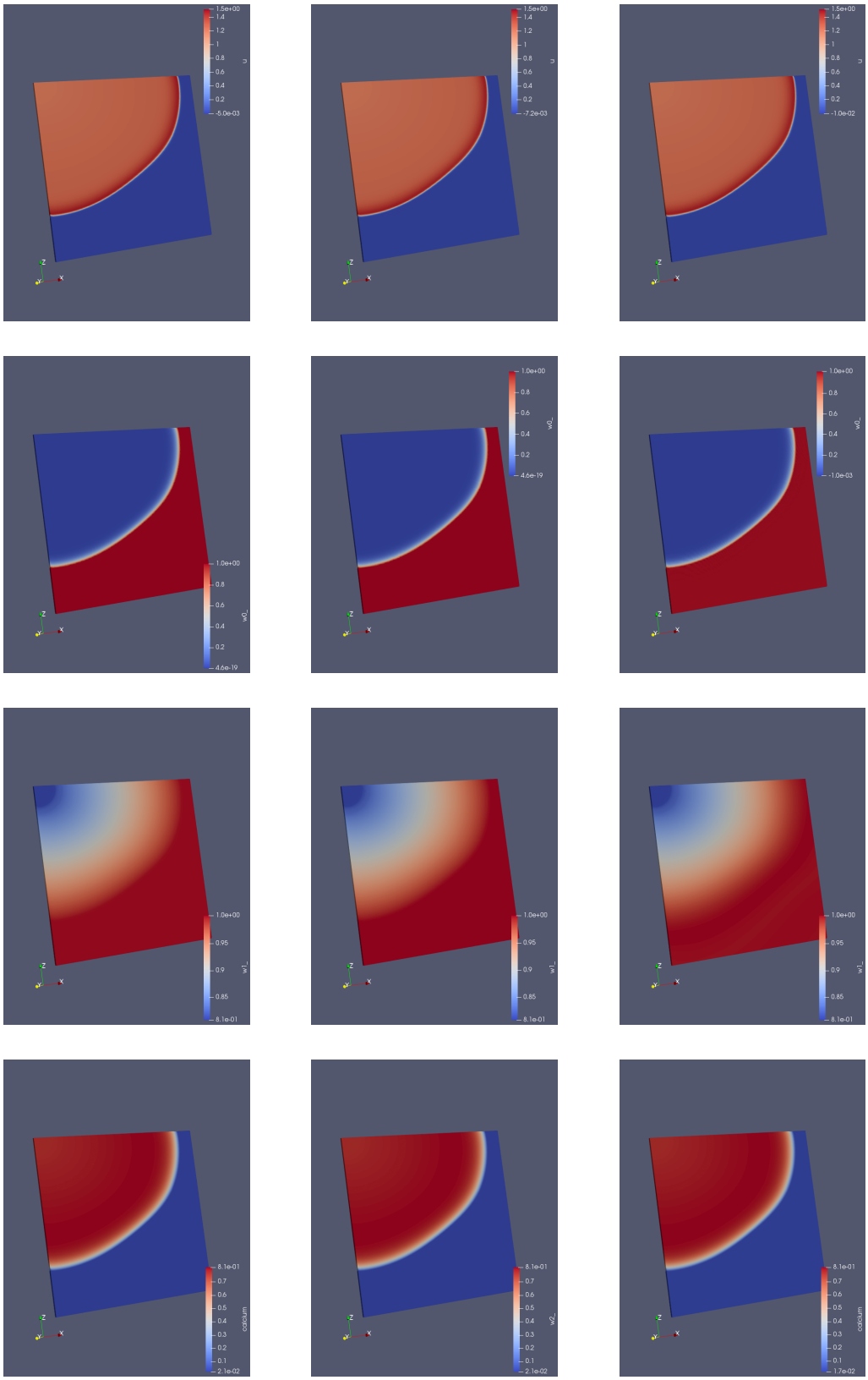

Figure 4.3: Snapshots of the transmembrane potential (first row) and the ionic variables (from the second row to the last one, w_1, w_2,w_3 rispectively) at 60ms in the POD-Galerkin ROM and $PODtol = 10^{-3}$. Left: FOM solutions; center: solutions of the POD-Galerkin ROM without *hyper-reduction*; right: solutions of the hyper-ROM model with Gappy POD reconstruction of the ionic variables (*POD-Galerkin-DEIM*).

In table 4.3 the relative errors are reported, varying the POD tolerance, when the ROM in the *POD phase* is built with a least-squares Petrov Galerkin projection.

Relative errors using LSPG projection	POD tolerance		
	10^{-1}	10^{-2}	10^{-3}
err_{u-POD}	1.00	$3.6{\cdot}10^{-1}$	$1.28{\cdot}10^{-2}$
$\text{err}_{u-PODDEIM}$	1.00	$3.85{\cdot}10^{-1}$	$1.7{\cdot}10^{-2}$
$\text{err}_{w1-Gappy}$	1.01	$2.58{\cdot}10^{-1}$	$6.53{\cdot}10^{-3}$
$\text{err}_{w2-Gappy}$	$1.79{\cdot}10^{-1}$	$1.17{\cdot}10^{-2}$	$8.51{\cdot}10^{-4}$
$\text{err}_{w3-Gappy}$	$9.71{\cdot}10^{-1}$	$2.93{\cdot}10^{-1}$	$6.05{\cdot}10^{-3}$

Table 4.3: Relative errors for the transmembrane potential and the ionic variables when building the ROM with the *POD-LSPG* approach.

The behavior of the solutions varying the POD tolerance is similar to the one resulting from the Galerkin projection, with a slightly better accuracy when the POD tolerance is equal to 10^{-3}, as we can see also from figure 4.6. In figures 4.4 and 4.5 we can see a snapshot at 120ms of the transmembrane potential and the ionic variables, from the FOM solution to the one of the hyper-reduction when using LSPG projection in the POD phase. At 120 ms it is possible to see the starting of the repolarization phase, which brings the potential to a negative value just after the depolarization phase, where the action potential changed the membrane potential to a positive value due to the applied current impulse.
In figure 4.4 the solutions obtained with a POD tolerance equal to 10^{-1} are reported, showing still a low-quality approximation of the variables, both in the *POD-Galerkin* ROM and the *POD-Galerkin-DEIM hyper*-ROM, due to the low number of bases adopted for the reduction. The use of LSPG does not increase the accuracy in this case, and this is because both Galerkin and LSPG projection are able to find optimal solution to the respective minimization problems (3.8) and (3.9), but the too low informations carried by the reduced bases results in the search for a solution that is not optimal in the global sense.

In figure 4.5 then, the solutions obtained with a POD tolerance equal to 10^{-3} are reported. Overall, the solutions are well-approximated, even when considering a time interval where both depolarization and repolarization phases are present, which represent an increasing of the stiffness of the monodomain problem due to the progression and the dissipation of the electric wave.

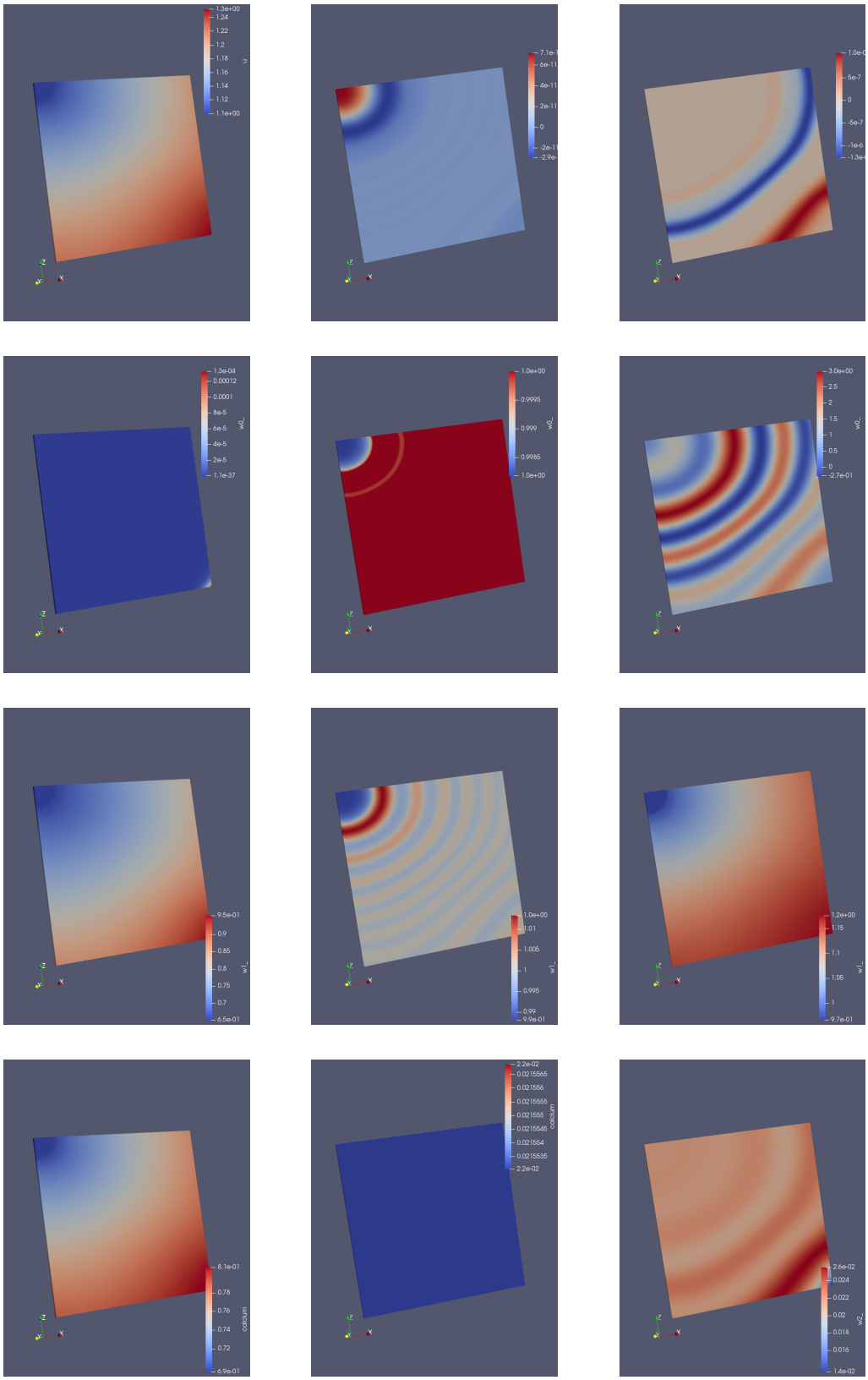

Figure 4.4: Snapshots of the transmembrane potential (first row) and the ionic variables (from the second row to the last one, w_1, w_2,w_3 rispectively) at 60ms in the POD-LSPG ROM and $PODtol = 10^{-1}$. Left: FOM solutions; center: solutions of the POD-LSPG ROM without *hyper-reduction*; right: solutions of the hyper-ROM model with Gappy POD reconstruction of the ionic variables (*POD-LSPG-DEIM*).

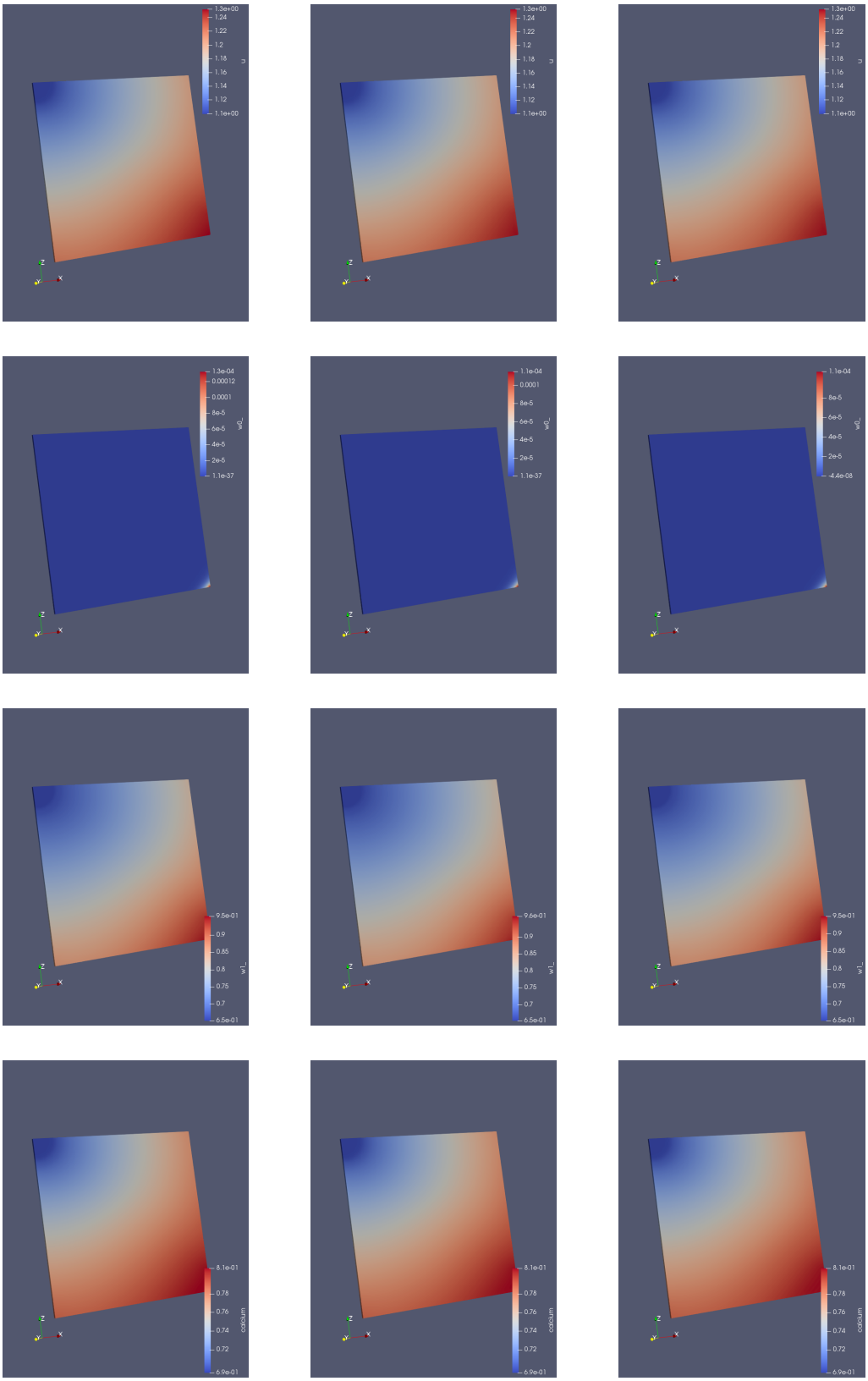

Figure 4.5: Snapshots of the transmembrane potential (first row) and the ionic variables (from the second row to the last one, w_1, w_2,w_3 rispectively) at 60ms in the POD-LSPG ROM and $PODtol = 10^{-1}$. Left: FOM solutions; center: solutions of the POD-LSPG ROM without *hyper-reduction*; right: solutions of the hyper-ROM model with Gappy POD reconstruction of the ionic variables (*POD-LSPG-DEIM*).

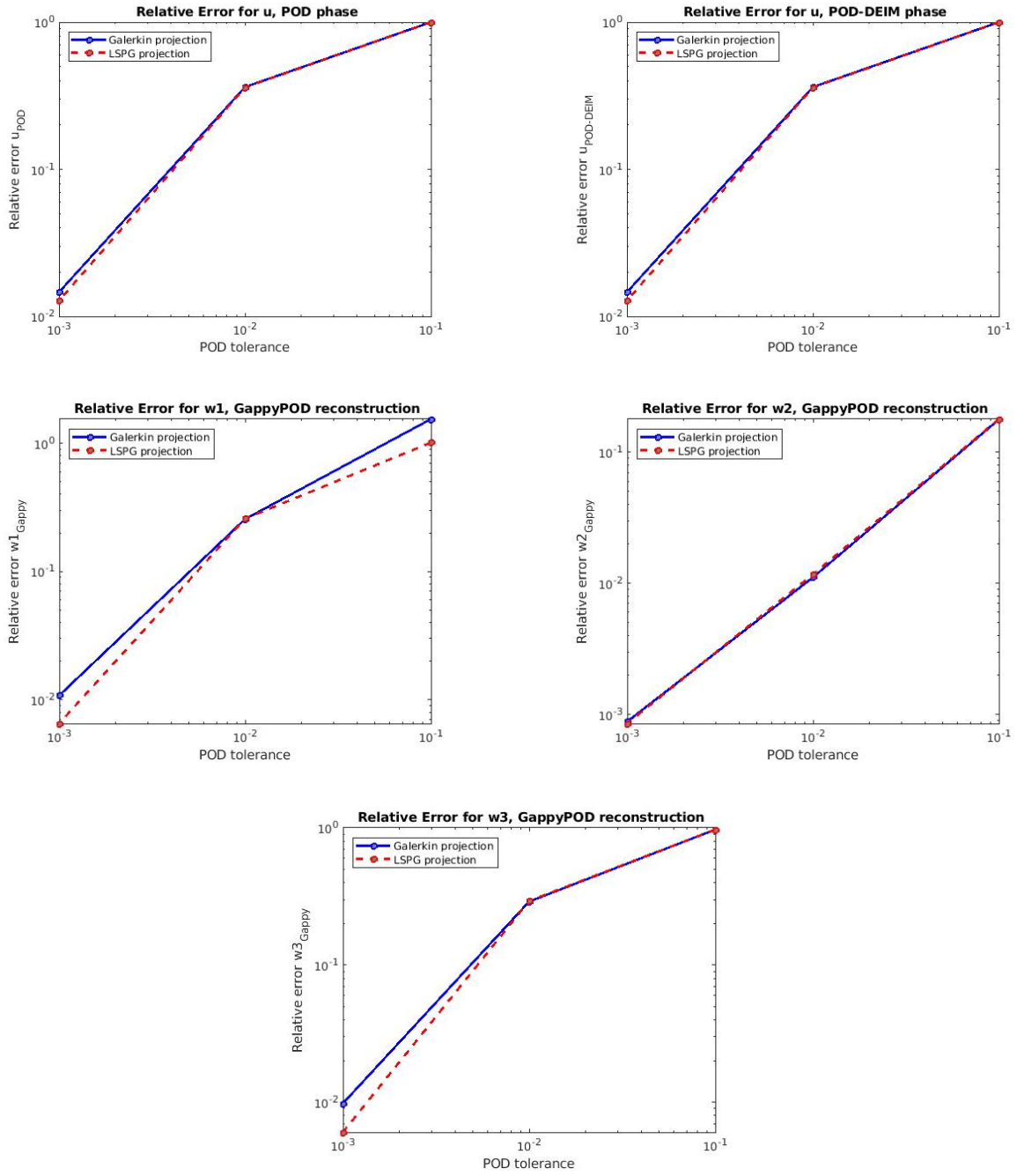

Figure 4.6: Relative errors varying the POD tolerance, comparing the *POD-Galerkin* approach with the *POD-LSPG* approach.

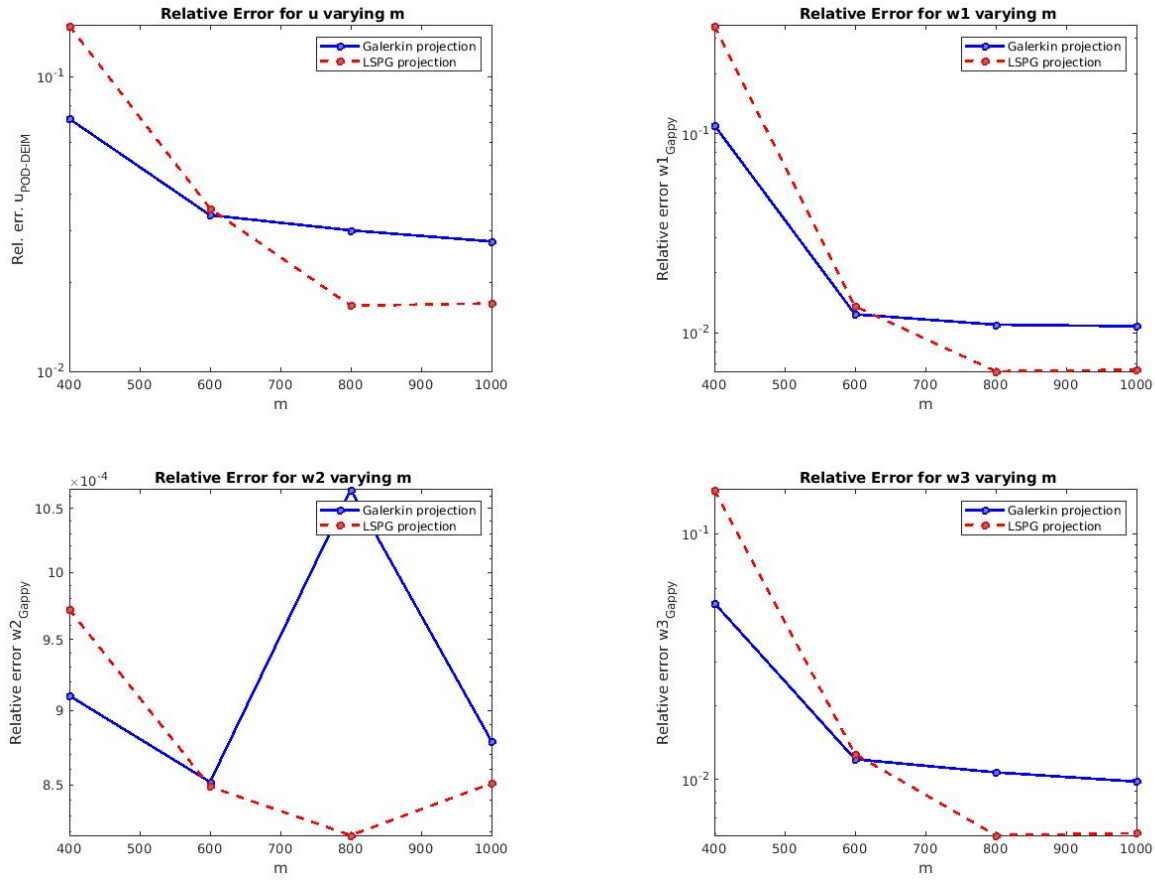

Figure 4.7: Relative errors varying the dimension of the reduced basis for the nonlinear terms m, which is also the number of interpolation points of the DEIM and the dimension of the *reduced mesh*, while keeping fixed the POD tolerance for the variables to 10^{-3}. Comparison of the *POD-Galerkin* approach with the *POD-LSPG* approach.

To evaluate also the accuracy varying the number of basis functions obtained by the POD method for the nonlinear residuals and, equivalently, the number of interpolation points m forming the *reduced mesh*, in figure 4.7 we show the relative errors related to the potential and the ionic variables varying m, when the POD tolerance for the variables is fixed to 10^{-3}. As we can see, the errors are higher for m close to the dimensions of the reduced bases of the potential and the ionic variables and decrease when m increases. The last cases tested, when $m = 1078$, correspond to the cases shown in figures 4.3 and 4.5, where, for the nonlinear term, the reduced basis is built through POD using a POD tolerance equal to 10^{-5}. In general, for higher dimensions m, the LSPG projection results slighlty more accurate than the Galerkin projection, while for lower m the *POD-Galerkin* method gives better results, even though are the cases of less accurate approximations.
In figure 4.8 the efficiency of the ROM is evaluated, both in the POD and POD-DEIM phases, comparing the two different approaches when building the ROM in the POD phase.

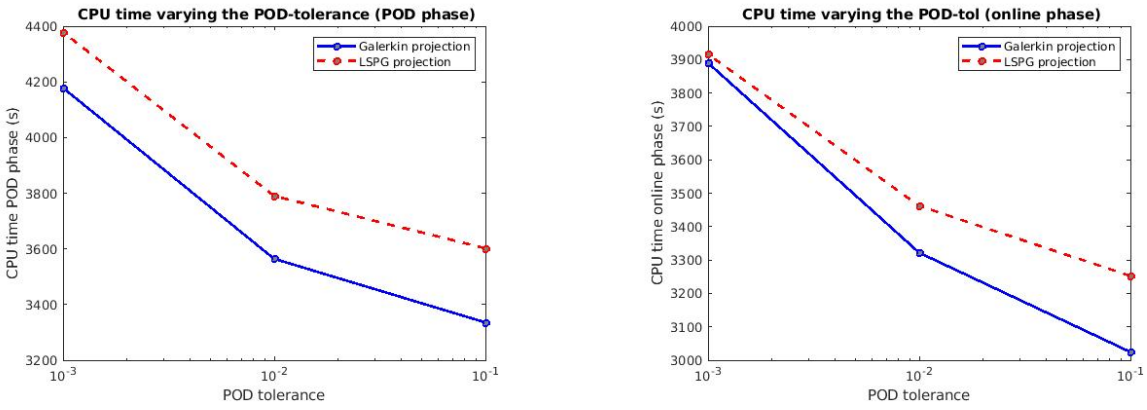

Figure 4.8: CPU time solving the POD-Galerkin ROM, without *hyper-reduction*, on the left and the POD-Galerkin-DEIM *hyper*-ROM on the right, comparing the *POD-Galerkin* approach with the *POD-LSPG* approach. The CPU time for solving the FOM is about 5400s.

The CPU time for solving the FOM is about 5400 s, so the computational speedup provided by the introduced reduced-order modeling is evident, namely, in the most efficient and accurate case, the speedup is $1.52x$ with respect to the FOM. In figure 4.8 we can also see how the LSPG approach is slightly less efficient in the *POD phase*, while almost comparable in the *POD-DEIM phase* when $tol_{POD} = 10^{-3}$, which is the case where the approximation of solutions with ROM are the most accurate.

4.3. Test 2: Parametrized electrophysiology on a slab domain

The cardiac electrophysiology problem highly depends on parameters variations, as we depicted in section 1.4. In this test we consider, for the electrical problem, $\mu \in \mathcal{P} \subset \mathbb{R}$, where $\mu = \sigma_m^l$ is the conductivity coefficient along the fibers direction. In particular, we let vary σ_m^l in the interval $[1.2 \cdot 10^{-4}, 2 \cdot 10^{-4}] m^2/s$ to understand how the RB techniques introduced, in particular the Gappy POD method, behave over parameters variations. The other two conductivities coefficients are fixed to the values $\sigma_m^t = 7 \cdot 10^{-5}\ m^2/s$ and $\sigma_m^n = 4 \cdot 10^{-5}\ m^2/s$.
The mesh, the fibers field and the time interval are the same considered in the previous section, namely, in figure 4.1 are shown the computational mesh and the fibers field, while the time interval is $(0, T)$, with $T = 120ms$, to proper characterize the depolarization phase of the transmembrane potential.
From the previous results, we decided to adopt a POD-Galerkin projection, since the fact that the Jacobian is symmetric and positive definite, in the problem considered, brings no particular differences in the results with respect to the POD least-squares Petrov-Galerkin projection.

4.3.1. ROM setup

In the first training phase, we solve the FOM for $N_{train} = 4$ parameters, namely $\mu_{1-FOM} = 1.2 \cdot 10^{-4}$, $\mu_{2-FOM} = 1.466 \cdot 10^{-4}$, $\mu_{3-FOM} = 1.733 \cdot 10^{-4}$, $\mu_{4-FOM} = 2 \cdot 10^{-4}$, to save snapshots of the transmembrane potential and the ionic variables in time, for each parameter. By the POD method we built the reduced basis, using a $tol_{POD} = 10^{-}3$; then, in the second training phase, we solve the ROM without *hyper-reduction* for $N_{train-ROM} = 5$ parameters, namely $\mu_{1-ROM} = 1.2 \cdot 10^{-4}$, $\mu_{2-ROM} = 1.4 \cdot 10^{-4}$, $\mu_{3-ROM} = 1.6 \cdot 10^{-4}$, $\mu_{4-ROM} = 1.8 \cdot 10^{-4}$, $\mu_{5-ROM} = 2 \cdot 10^{-4}$, to save snapshots of the residual in time, for each parameter. The transformation matrix $\mathbf{\Phi}$ for the residual is obtained by POD with a $tol_{POD} = 10^{-4}$. We then selected the minimum dimension of the POD spaces for each variable in order to attain accurate results; these values and the *offline* overall time for the construction of the ROM are displayed in table 4.4.
The nature of the cardiac electrophysiology problem, which consists in the propagation of a very steep wave, limits the efficiency of the parametrized ROM built, especially when relying on global basis functions to approximate the solution, as the case in analysis. Thus, an high number of reduced basis are needed to correctly approximate the high variability of the solution in time and for different parameters. Moreover, the high dimensions of the algebraic systems in the FOM represented a challenging task in the training simulations over the high performance computer adopted, especially for memory allocation, since the snapshots in time of the solutions and the nonlinear term, for each parameter in the training phase, are dense matrices in $\mathbb{R}^{197985 \times 1200}$, with a weight of 1.9 Gb, hence making impossible to consider larger sets of training and limiting the diagnostic of the model.

Offline CPU time:	
FOM training	21692.12s
Non *hyper*-ROM training	24701.53s
Total *Offline* time	46393.65s
POD spaces dimension:	
n_u	950
n_{w_1}	900
n_{w_2}	10
n_{w_3}	350
m	2000

Table 4.4: *Offline* phase CPU time and dimension of the POD spaces in the construction of the *hyper*-ROM for the electrophysiology parametrized problem.

4.3.2. Numerical results

For testing, we consider $N_{test} = 3$ new parameters, namely $\mu_1 = 1.3 \cdot 10^{-4}$, $\mu_2 = 1.5 \cdot 10^{-4}$ and $\mu_3 = 1.9 \cdot 10^{-4}$. In table 4.5 we report the mean of the relative errors over the parameters tested, defined as follows

$$\overline{err}_{\mathbf{g}} = \frac{1}{N_{test}} \sum_{i=1}^{N_{test}} err_{\mathbf{g}}(\boldsymbol{\mu}_i),$$

where $\mathbf{g}$ is either the transmembrane potential or a ionic variable approximation computed in the *online* phase. Moreover, in the table we show also the mean CPU time for the FOM simulation and the one in the ROM *online* phase, together with the speedup gained, which is low, $1.24x$, mainly due to the high dimension of the reduced basis, as depicted in the previous subsection. In figures 4.9 and 4.11 we show the evolution in

Mean relative error over the $N_{test} = 3$ parameters	
$\overline{err}_{u-PODDEIM}$	$5.27{\cdot}10^{-2}$
$\overline{err}_{w1-Gappy}$	$1.12{\cdot}10^{-1}$
$\overline{err}_{w2-Gappy}$	$1.38{\cdot}10^{-2}$
$\overline{err}_{w3-Gappy}$	$2.53{\cdot}10^{-2}$
Mean CPU time:	
CPU time FOM	5127.49s
CPU time *hyper*-ROM	4131.12s
Speed up	1.24

Table 4.5: Mean of the relative error for the transmembrane potential and the ionic variables ROM approximations and mean CPU time of the FOM and HRROM simulations over the $N_{test} = 3$ parameters tested.

time of the transmembrane potential u and the intracellular calcium concentration w_3, respectively, comparing the FOM solution to the *online* ROM approximation, obtained by the parameter μ_1. Similarly, in figures 4.10 and 4.12 we show the evolution in time of the transmembrane potential u and the intracellular calcium concentration w_3, respectively, comparing the FOM solution to the *online* ROM approximation, obtained by the parameter μ_3.
The results of the ROM approximation are accurate with respect to the FOM solution, meaning that the parametrized ROM constructed is able to characterize the evolution of the solutions under parameters variation in the cardiac electrophysiology problem.

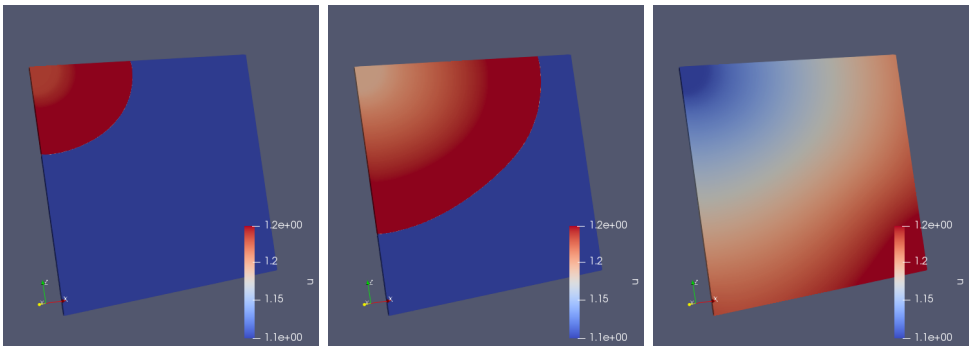

(a) t=30ms, μ_1−FOM (b) t=60ms, μ_1−FOM (c) t=120ms, μ_1−FOM

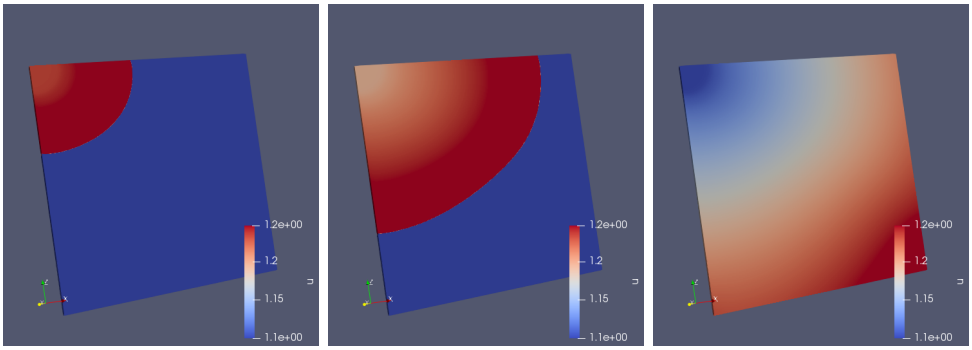

(d) t=30ms, μ_1−ROM (e) t=60ms, μ_1−ROM (f) t=120ms, μ_1−ROM

Figure 4.9: Evolution of the transmembrane potential in time; comparison between FOM (top) and *online hyper*-ROM (bottom) for the parameter μ_1.

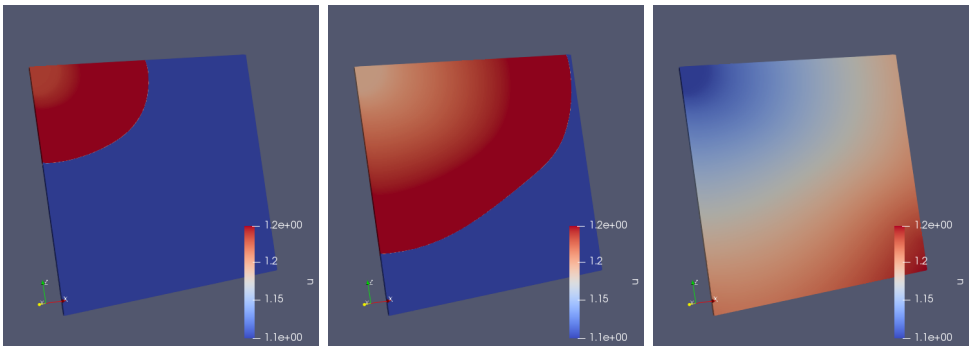

(a) t=30ms, μ_3−FOM (b) t=60ms, μ_3−FOM (c) t=120ms, μ_3−FOM

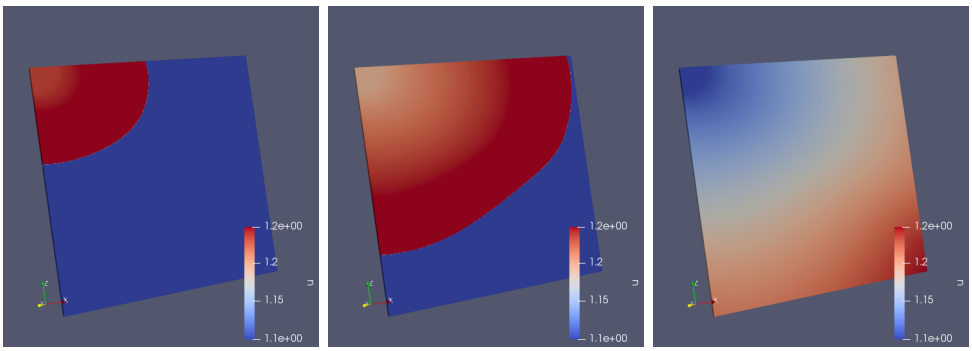

(d) t=30ms, μ_3−ROM (e) t=60ms, μ_3−ROM (f) t=120ms, μ_3ROM

Figure 4.10: Evolution of the transmembrane potential in time; comparison between FOM (top) and *online hyper*-ROM (bottom) for the parameter μ_3.

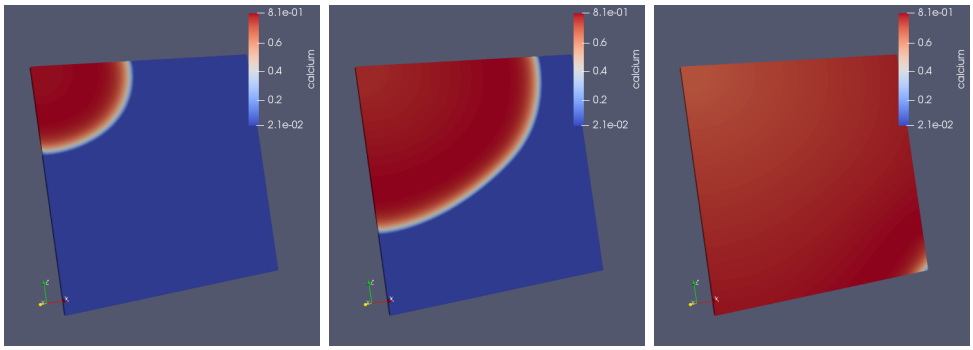

(a) t=30ms, μ_1-FOM (b) t=60ms, μ_1-FOM (c) t=120ms, μ_1-FOM

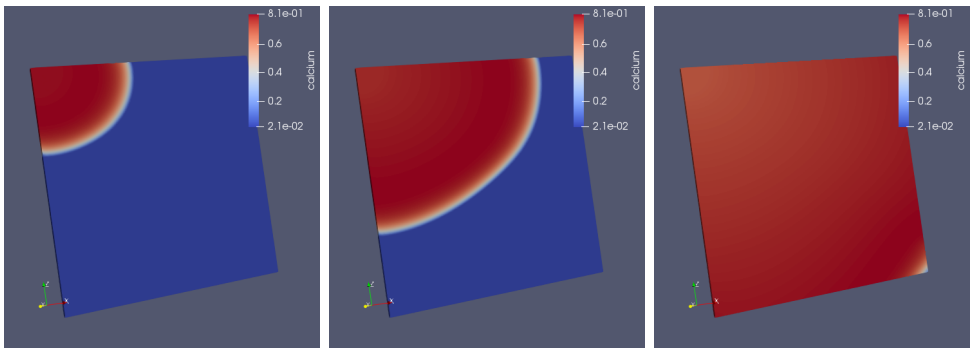

(d) t=30ms, μ_1-ROM (e) t=60ms, μ_1-ROM (f) t=120ms, μ_1-ROM

Figure 4.11: Evolution of the intracellular calcium in time; comparison between FOM (top) and *online hyper*-ROM (bottom) for the parameter μ_1.

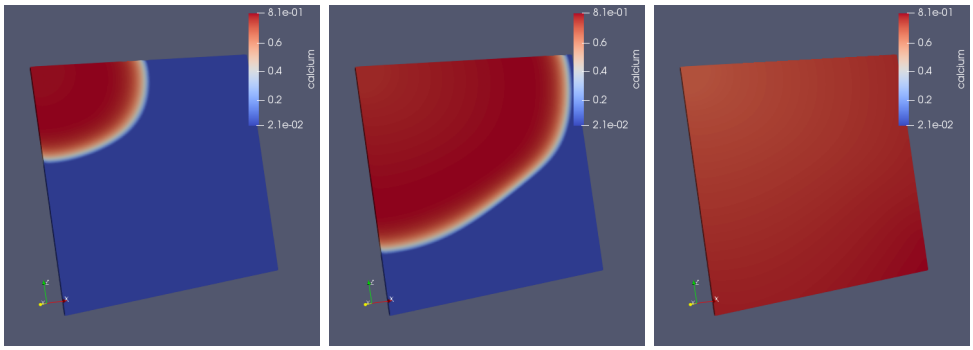

(a) t=30ms, μ_3-FOM (b) t=60ms, μ_3-FOM (c) t=120ms, μ_3-FOM

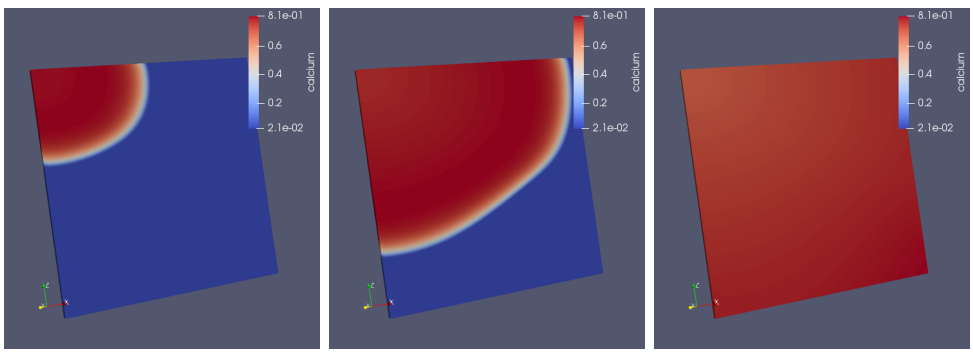

(d) t=30ms, μ_3-ROM (e) t=60ms, μ_3-ROM (f) t=120ms, μ_3ROM

Figure 4.12: Evolution of the intracellular calcium in time; comparison between FOM (top) and *online hyper*-ROM (bottom) for the parameter μ_3.

4.4. Test 3: Evaluation of ionic variables on a left ventricle

In this third test case, we consider the three-dimensional monodomain model over a patient-specific left ventricle domain. The geometry derives from the Zygote Solid 3D heart model [45].
Similarly to the case test 1, section 4.2, the mesh consists in two global refinement steps of the initial grid, leading to 293632 cells and $N_{he} = 314129$ degrees of freedom. In figure 4.13, the left ventricle computational mesh is displayed.

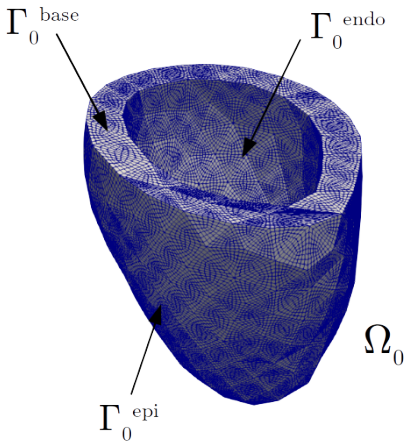

Figure 4.13: Left ventricle computational mesh for cardiac electrophysiology ($\mathcal{T}_{he}$).

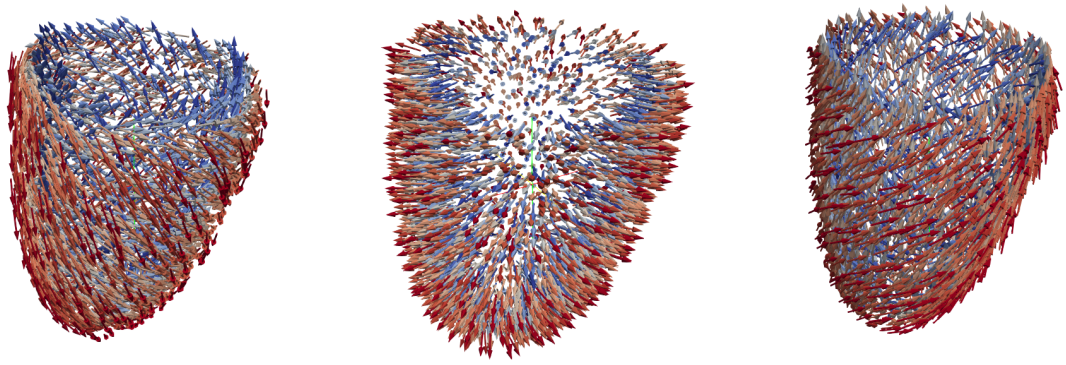

Figure 4.14: Representation of fibers, sheets and normal fields ,rispectively.

The fibers and sheets distribution is generated according to the rule-based algorithm pro-

posed in [51], in figure 4.14.
The time interval considered is $(0, T)$, with $\Delta t_e = 10^{-4}$ and $T = 210ms$, which is larger than the one we used in the first test case, since it is of interest to explore and capture the evolution of the transmembrane potential and, in particular, of the calcium concentration, also during the repolarization phase. This is mainly due to the cardiac electromechanical coupling, in fact the mechanical contraction, which depends on intracellular calcium concentration, is a much slower process than the electrical propagation.
Due to the high number of degrees of freedom needed to obtain a realistic and stable solution, and the dimension of the time interval considered, the computational resources adopted for the simulations weren't sufficient to build a well trained parametrized electrical ROM. Thus, we present the results by fixing the electrical conductivities, with the aim to analyze efficiency and accuracy of the cardiac electrophysiology reduced-order model in more complex scenarios. The conductivity tensor is the same considered in the first test, namely

$$\mathbf{D}(\mathbf{x}) = \sigma_m^t \mathbf{1} + (\sigma_m^l - \sigma_m^t)\mathbf{f}_0 \otimes \mathbf{f}_0 + (\sigma_m^n - \sigma_m^t)\mathbf{n}_0 \otimes \mathbf{n}_0,$$

with $\sigma_m^l = 1.5 \cdot 10^{-4}\ m^2/s$, $\sigma_m^t = 7 \cdot 10^{-5}\ m^2/s$ and $\sigma_m^n = 4 \cdot 10^{-5}\ m^2/s$ for the longitudinal to the fibers, transversal and normal conductivity coefficients respectively.
The electrical gaussian impulse I_{app} is applied at three points, located on the endocardial surface, close to the apex.

4.4.1. Dimensions of the reduced spaces varying the POD tolerance

As we have done in section 4.2, to evaluate the accuracy and the efficiency of reduced-order model, the tests are performed varying the dimension of the reduced basis. In table (4.6), for each variable, we have the POD space dimension corresponding to the respective POD tolerance adopted for each simulation, which are $tol_{POD} = 10^{-1},\ 10^{-2}$ and 10^{-3}:

tol_{POD}	10^{-1}	10^{-2}	10^{-3}
n_u	5	74	182
n_{w_1}	7	44	249
n_{w_2}	1	2	16
n_{w_3}	3	17	69
m	75	510	566

Table 4.6: Dimensions of the reduced-order spaces for the different variables varying the POD tolerance. The dimension m of the reduced space for the nonlinear terms is obtained using a POD tolerance equal to 10^{-5} in all the three cases.

The POD tolerance adopted for the snapshot matrix of the nonlinear residuals is $tol_{DEIM} = 10^{-5}$ for all the case tested. Since those snapshots are taken by solving the reduced-order

model without *hyper-reduction*, Eq. (3.3), the dimension m depends also on the dimension of the reduced spaces for the variables, namely on the quality of the non *hyper-reduced*-order approximation.

4.4.2. Numerical results

Here we present the numerical results of the propagation of the transmembrane potential and the ionic variables over the left ventricle.
In table 4.7, where the relative errors are displayed for the three different reduced-order models considered, we can see that the results are similar to the ones obtained over the slab domain, in section 4.2. Namely, when the dimension of the reduced-order spaces for the variables is small, the approximation by ROM is not accurate and it is mainly due to the nature of problems like the monodomain model for cardiac electrophysiology. By increasing the number of basis functions $n.$ and interpolation points m considered accuracy increases monotonically, however, too lower POD tolerances yield to unefficient reduced-order modeling, so it is important to find the right *trade-off* between accuracy and efficiency when building ROMs.
In table 4.8 and figure 4.15 we show the comparison of the computational costs between the full-order model, the reduced-order model and the *hyper*-reduced-order model (*online* phase). In particular, it is possible to see the great improvement in terms of CPU time of the ROM's *online* phase with respect to the FOM, even when considering a lower POD tolerance, i.e. an higher number of basis functions, e.g. $tol_{POD} = 10^{-3}$, which consists in more accurate approximation obtained by reduced-order modeling. Namely, in the most efficient and accurate case, the *online* phase simulation gains a speedup of $3.09x$ with respect to the FOM simulation.

Relative errors	POD tolerance		
	10^{-1}	10^{-2}	10^{-3}
err_{u-POD}	1.00	$9.45{\cdot}10^{-2}$	$5.55{\cdot}10^{-3}$
$\text{err}_{u-PODDEIM}$	$\gg 1$	$9.73{\cdot}10^{-2}$	$8.61{\cdot}10^{-3}$
$\text{err}_{w1-Gappy}$	$\gg 1$	$7.84{\cdot}10^{-1}$	$8.26{\cdot}10^{-2}$
$\text{err}_{w2-Gappy}$	$6.3{\cdot}10^{-1}$	$3.3{\cdot}10^{-3}$	$8.71{\cdot}10^{-4}$
$\text{err}_{w3-Gappy}$	$9.82{\cdot}10^{-1}$	$5.31{\cdot}10^{-2}$	$4.03{\cdot}10^{-3}$

Table 4.7: Relative errors for the transmembrane potential and the ionic variables *hyper*-ROM approximations built varying the POD tolerance.

CPU time [s]	POD tolerance		
	10^{-1}	10^{-2}	10^{-3}
FOM	17020.53	16878.27	17203.32
ROM	15268.62	15237.97	15652.19
hyper-ROM	4677.69	5464.27	5918.24

Table 4.8: CPU time of the full-order model and the reduced-order models varying the POD tolerance.

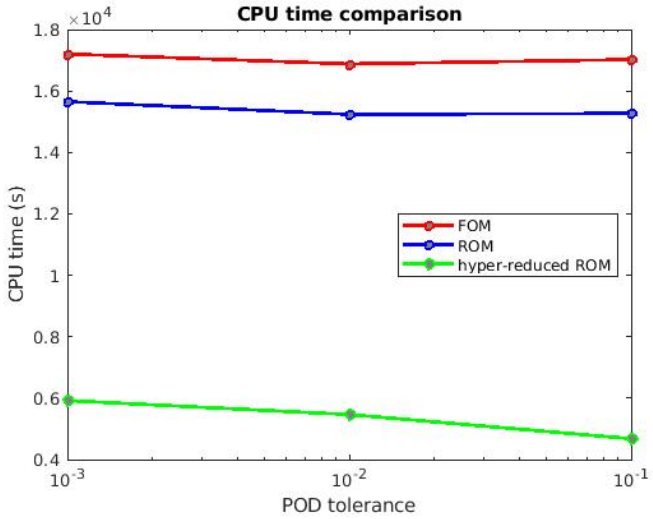

Figure 4.15: CPU time [s] for the simulation of FOM (red), ROM (blue) and *hyper*-ROM (green) varying the POD tolerance.

In figures 4.16 and 4.17, the comparison between the high-fidelity solution, obtained by FOM, and the reduced-order approximation, obtained by Gappy POD reconstruction during the *online* phase, with a $tol_{POD} = 10^{-3}$, is displayed for the variables w_1 and w_2, respectively. In particular, three snapshots in time are shown, namely 35ms, 70ms and 210ms, to characterize the evolution in time of the two ionic variables. The high accuracy obtained by the *hyper-reduced* approximation of the solution with respect to FOM leads to see no differences between the two solutions, whereas the computational costs are highly reduced for the former, as we have seen in table 4.8.
On the other hand, in figures 4.18 and 4.19, we show the comparison between the high-fidelity solution, obtained by FOM, and the reduced-order approximations, obtained during the *online* phase, with a $tol_{POD} = 10^{-3}$ and a $tol_{POD} = 10^{-2}$, for the intracellular calcium concentration w_3 and the transmembrane potential u, respectively. The snapshots of the two variables are taken for four different time instants, namely 35ms, 70ms, 140ms and 210ms, which show the propagation in time, starting from the three initial I_{app} impulses. Moreover, the solution obtained by the ROM built with a POD tolerance equal to 10^{-2} is displayed to show that also with a smaller number of basis functions for the variables, with respect to the case where $tol_{POD} = 10^{-3}$, the approximations are

sufficiently accurate, while having a gain in efficiency. This is an important result for the electromechanical reduced-order model, since, if we consider a $tol_{POD} = 10^{-2}$, the intracellular calcium concentration, responsible for the active contraction, can be accurately obtained by the Gappy POD method, in the online phase, through a relatively small number of basis, increasing the overall efficiency of the model.

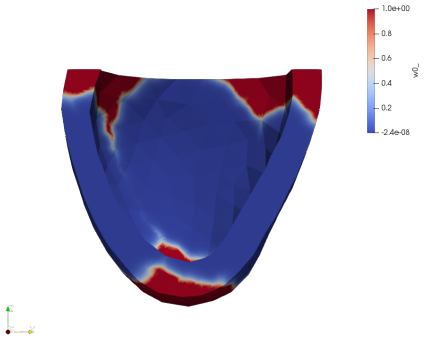

(a) t=35ms, FOM

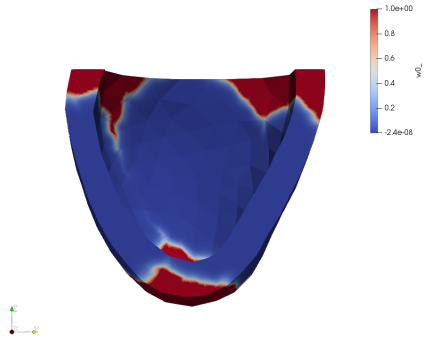

(b) *hyper*-ROM

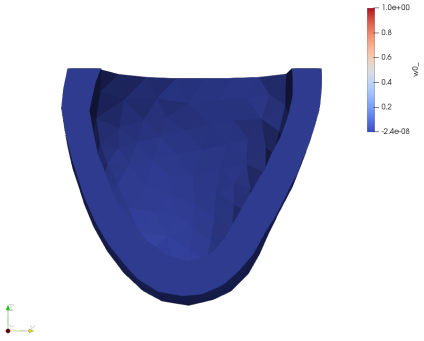

(c) t=70ms, FOM

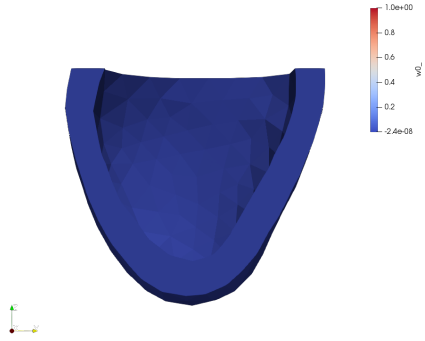

(d) *hyper*-ROM

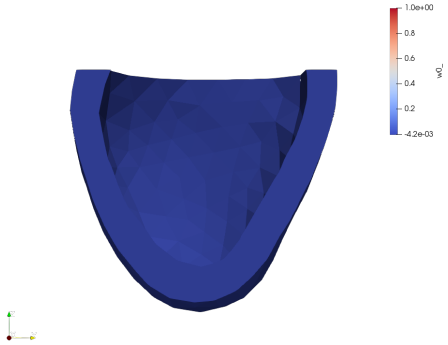

(e) t=210ms, FOM

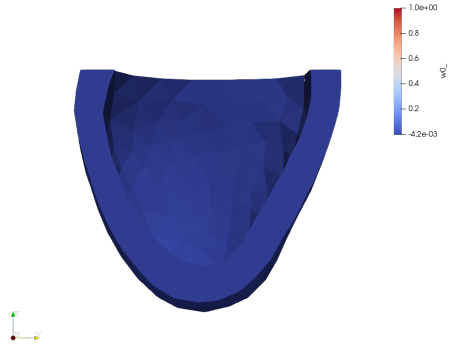

(f) *hyper*-ROM

Figure 4.16: Evolution of w1 in time; comparison between FOM and *online* ROM when $\text{tol}_{POD} = 10^{-3}$.

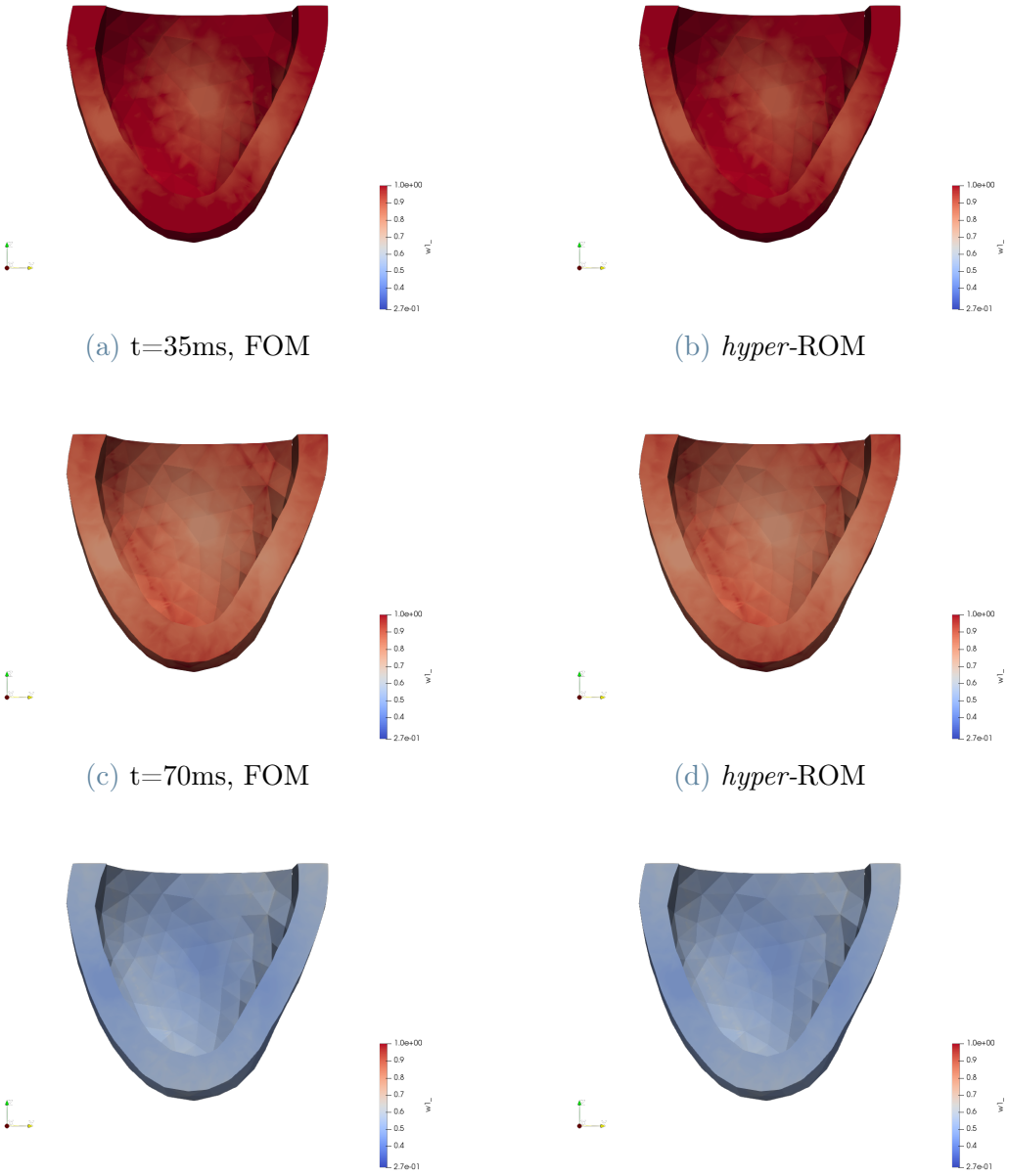

(a) t=35ms, FOM (b) *hyper*-ROM

(c) t=70ms, FOM (d) *hyper*-ROM

(e) t=210ms, FOM (f) *hyper*-ROM

Figure 4.17: Evolution of w2 in time; comparison between FOM and *online* ROM when $tol_{POD} = 10^{-3}$.

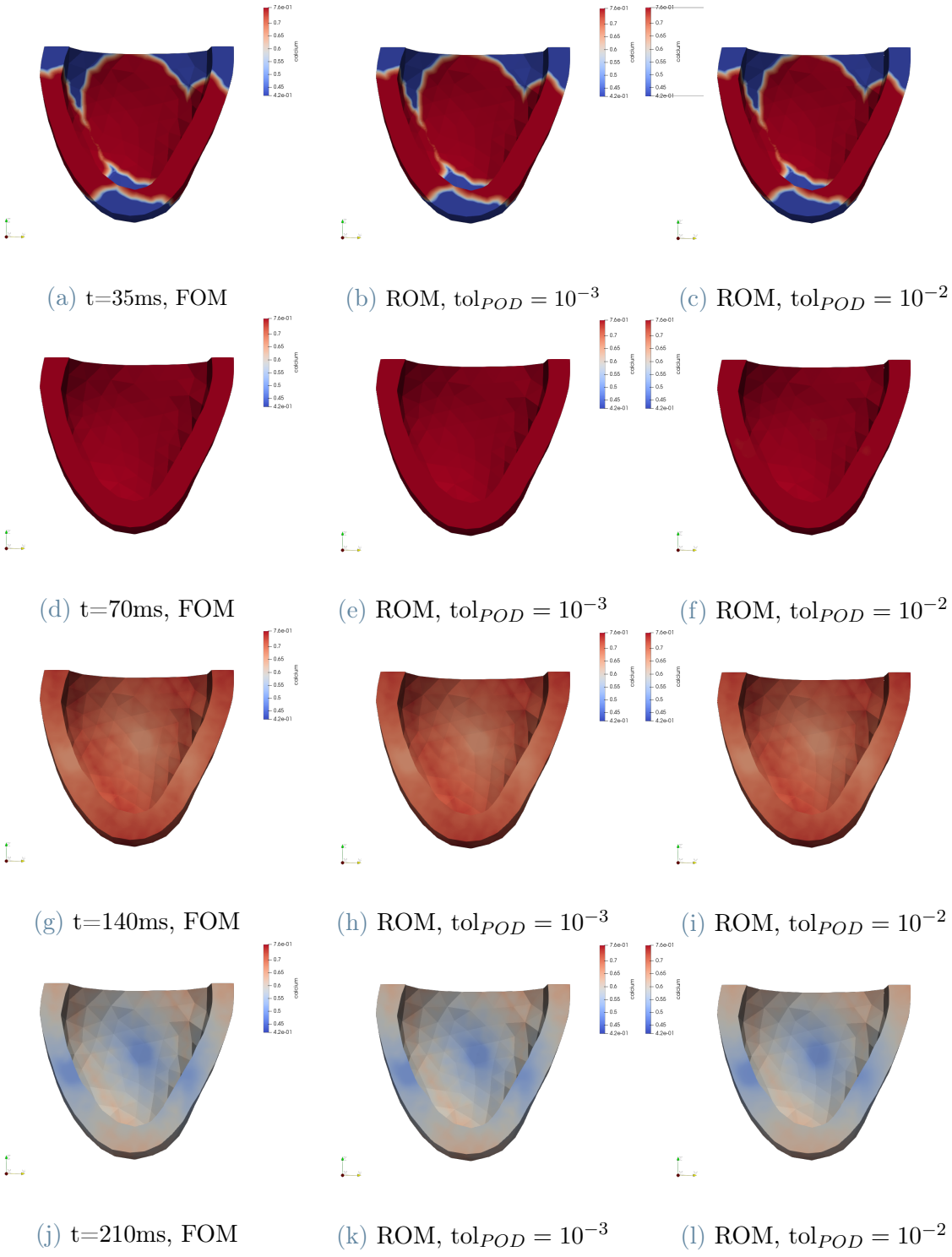

(a) t=35ms, FOM (b) ROM, $\text{tol}_{POD} = 10^{-3}$ (c) ROM, $\text{tol}_{POD} = 10^{-2}$

(d) t=70ms, FOM (e) ROM, $\text{tol}_{POD} = 10^{-3}$ (f) ROM, $\text{tol}_{POD} = 10^{-2}$

(g) t=140ms, FOM (h) ROM, $\text{tol}_{POD} = 10^{-3}$ (i) ROM, $\text{tol}_{POD} = 10^{-2}$

(j) t=210ms, FOM (k) ROM, $\text{tol}_{POD} = 10^{-3}$ (l) ROM, $\text{tol}_{POD} = 10^{-2}$

Figure 4.18: Evolution of the intracellular calcium (w3) in time; comparison between FOM (left), *online hyper*-ROM when $tol_{POD} = 10^{-3}$ (center), *online hyper*-ROM when $tol_{POD} = 10^{-2}$ (right).

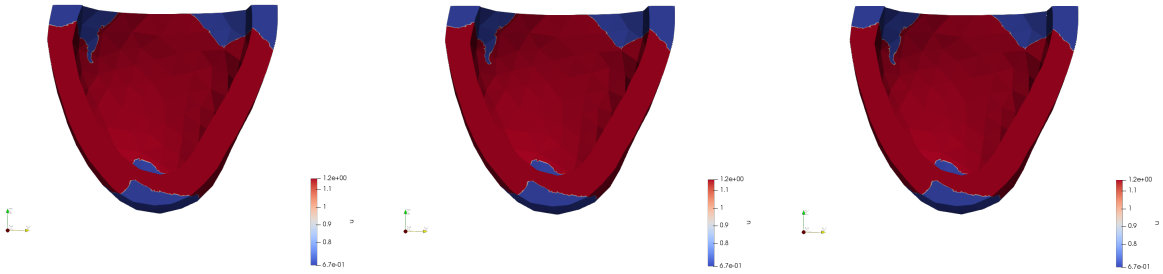

(a) t=35ms, FOM (b) ROM, $\text{tol}_{POD} = 10^{-3}$ (c) ROM, $\text{tol}_{POD} = 10^{-2}$

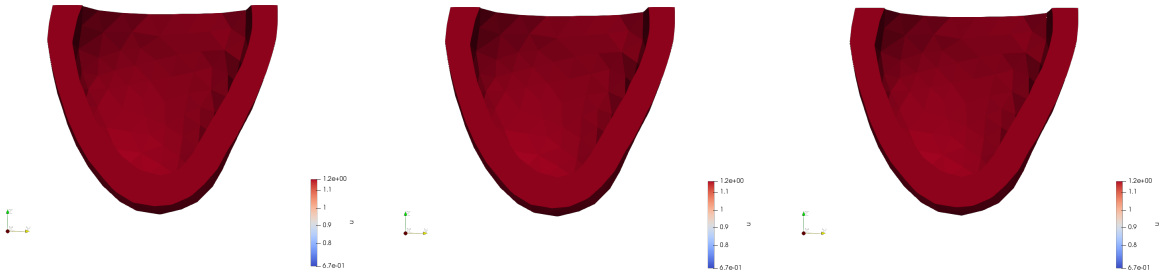

(d) t=70ms, FOM (e) ROM, $\text{tol}_{POD} = 10^{-3}$ (f) ROM, $\text{tol}_{POD} = 10^{-2}$

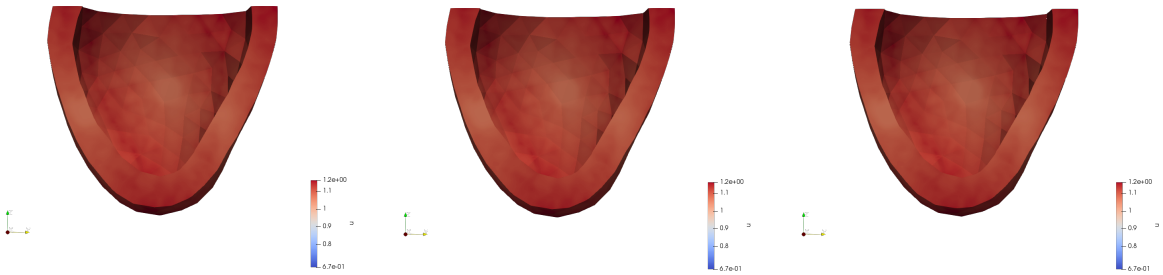

(g) t=1400ms, FOM (h) ROM, $\text{tol}_{POD} = 10^{-3}$ (i) ROM, $\text{tol}_{POD} = 10^{-2}$

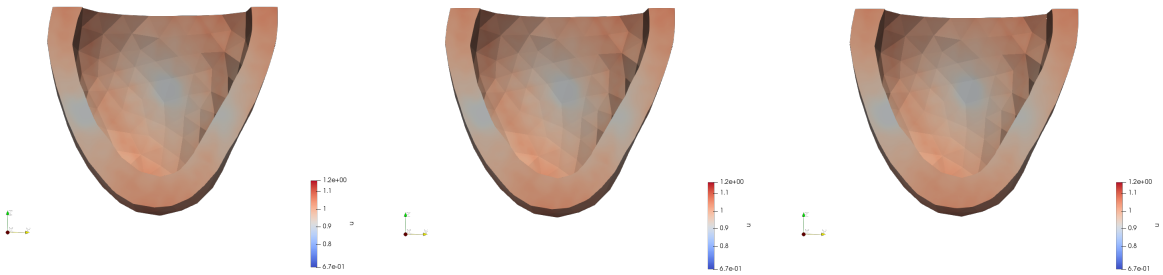

(j) t=210ms, FOM (k) ROM, $\text{tol}_{POD} = 10^{-3}$ (l) ROM, $\text{tol}_{POD} = 10^{-2}$

Figure 4.19: Evolution of the transmembrane potential (u) in time; comparison between FOM (left), *online hyper-* ROM when $tol_{POD} = 10^{-3}$ (center), *online hyper-* ROM when $tol_{POD} = 10^{-2}$ (right).

5 | A parametrized one-way coupled electromechanical ROM

In this chapter, we analyze the numerical performances of reduced-order modeling for the electromechanical coupling. In particular, we will analyze the overall efficiency and accuracy of the coupled reduced-order model under parameters variations for the mechanical model, wherein the activation depends on the intracellular calcium concentration, efficiently evaluated by the cardiac electrophysiology ROM.

5.1. Setting

5.1.1. *Offline-online* strategy

As we have done in the previous chapter for cardiac electrophysiology, we recall the steps to build a ROM for the parametrized mechanical problem. Namely, given $\boldsymbol{\mu}_j \in \mathcal{P}$, where $\mathcal{P}$ is the parameters' space and $j = 1, ..., N_{train}$, with N_{train} the training dimension, the *offline* phase consists in the following steps:

- Step 1: solve the FOM, Eq. (2.13), for the N_{train} training parameters, to save snapshots of the displacement field $\mathbf{d}(\boldsymbol{\mu}_j)$, from which the transformation matrix $\mathbf{V_d}$ is computed by means of proper orthogonal decomposition;
- Step 2: solve a first non *hyper*-ROM, described by Eq.s (3.15) and (3.16), for $N_{train-ROM}$ parameters and save snapshots of the residual $\mathbf{r_d}(\boldsymbol{\mu}_j)$ to construct the transformation matrix $\boldsymbol{\Phi_d}$ through POD;
- Step 3: assemble the left projection matrix for the DEIM in order to build an *hyper*-ROM.

Once the *offline* phase is computed, in the *online* phase, for each new instance of $\boldsymbol{\mu} \in \mathcal{P}$, we solve the *hyper-reduced* system (3.18) or (3.19), depending on the cardiac cycle phase, to efficiently and accurately approximate the displacement field.

The *online* phase of the one-way coupled electromechanical reduced-order model can be summarized as follows:

- Solve the *online* phase for the cardiac electrophysiology, saving at each time step $l = 1, ..., N_t$ the reduced-order reconstructed ionic variable $w_3^l \in R^{N_{h_e}}$;
- Interpolate the ionic variable approximating calcium dynamics on the coarser mesh $\mathcal{T}_{h_m}$ by an intergrid map to obtain $w_{3,h_m}^l \in R^{N_{T_a}}$, for each $l = 1, ..., N_t$;
- Solve the *online* phase for the cardiac mechanics, where, at each time step $k = 1, ..., N_{t_m}$, we update the active tension T_{a,h_m}^k by solving Eq. (2.12), which depends on the calcium concentration w_{3,h_m}.

To evaluate the accuracy of the ROM approximation for the displacement, we consider the mean relative error presented in chapter 4, Eq. (4.1), where, here, $\mathbf{g}$ refers to the displacement field $\mathbf{d}$, namely we will refer to it as $err_{\mathbf{d}-online}$.

5.1.2. Parameters of interest and time interval

ROM techniques allow to efficiently solve parametric problems in different scenarios, in order to asses the effect of some relevant parameters on the solutions, which is of crucial importance in clinical applications to account a possible inter-patient variability. The parameters' space considered for the electromechanical problem is $\mathcal{P} \subset \mathbb{R}^2$.
In particular, the two parameters of interest regards the mechanical subproblem and they are the Bulk modulus B, in Eq. (1.9) , which influences the material incompressibility, namely it indicates how much the cardiac tissue is resistent to compression, and the peripheral resistance R in the two-element Windkessel model (1.14), which indicates the resistance that must be overcome to push blood through the circulatory system and create flow.
It is important to specify that the developed implementation of the model allows also to consider parametrizations of the electrophysiology ROM system and how they affect the mechanical solution, which is an important task in order to fully understand the various dynamics of an heartbeat under parameter variations.
For what concerns the time interval, we consider $(0, T)$ with $T = 210ms$ to evaluate efficiency and accuracy of the ROM electromechanical coupling. This time interval allow us to show the first two phases of the cardiac cycle, namely the first isovolumetric phase and the ejection phase, which correspond to the cardiac systolic phase, i.e. the contraction mechanism, wherein we can mainly characterize the influences of electrical propagation in cardiac mechanics. Moreover, for the time discretization, we use a time step $\Delta t_e = 10^{-4}$ for cardiac electrophysiology and a time step $\Delta t_m = 10^{-3}$ for cardiac mechanics, yielding to $N_t = 2100$ timesteps and $N_{t_m} = 210$ timesteps, respectively, and $q = \dfrac{\Delta t_m}{\Delta t_e} = 10$.

5.2. Parametrized one-way coupled electromechanics on a left ventricle

In the following test cases, we evaluate the electromechanical coupling on the undeformed reference domain Ω_0, which is the patient-specific left ventricle presented in section 4.4. For cardiac electrophysiology, the mesh considered is the one shown in figure 4.13, with two refinement steps of the initial grid; for cardiac mechanics, the coarser mesh is presented in figure 5.1 and consists in 4588 cells, with $N_{h_m} = N_d = 18501$ dofs for the displacement and $N_{T_a} = 6167$ dofs for the active tension.

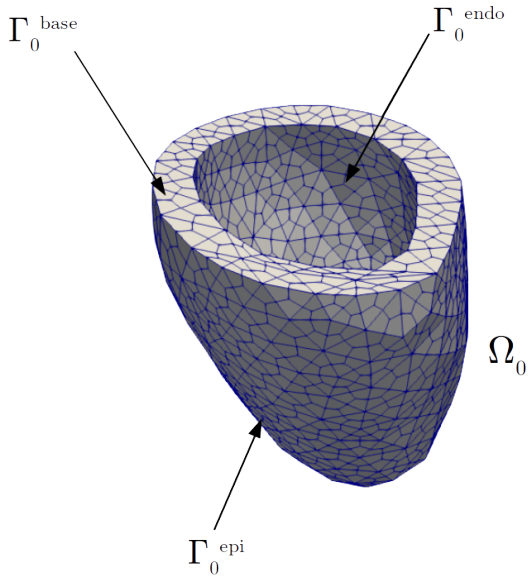

Figure 5.1: Left ventricle computational mesh for cardiac mechanics ($\mathcal{T}_{h_m}$).

5.2.1. ROM setup

Here we present the setting of the electromechanical reduced-order model considered in the tests and we show the main results related to the *offline* phase, in order to develop an efficient and accurate *hyper*-ROM.

For the cardiac electrophysiology, we fix the conductivity coefficients to $\sigma_m^l = 1.5 \cdot 10^{-4}\ m^2/s$, $\sigma_m^t = 7 \cdot 10^{-5}\ m^2/s$ and we build the reduced-order models varying the POD tolerance; namely, the dimension of the reduced basis adopted are the ones displayed in table 4.6, focusing on the cases $tol_{POD} = 10^{-2}$ and $tol_{POD} = 10^{-3}$.

On the other hand, as anticipated in subsection 5.1.2, for the mechanical problem we consider a dependence on the parameter $\boldsymbol{\mu} \in \mathcal{P}$, with $\boldsymbol{\mu} = [B, R]$, where the Bulk modulus B varies in the interval $[2.5 \cdot 10^4, 7.5 \cdot 10^4]Pa$ and the peripheral resistance R varies in

$[2.5 \cdot 10^7, 4.5 \cdot 10^7] Pa \cdot s/m^3$.
The construction of the ROM for the parametrized mechanical problem involves two *offline* training phases. The first training phase consists in solving the mechanical FOM for $N_{train} = 20$ different parameters, selected homogeneously [1] on the intervals considered, to generate snapshots of the displacement field. By proper orthogonal decomposition, with a $tol_{POD} = 10^{-3}$, we obtain $n_d = 31$ basis functions for the displacement $\mathbf{d}$. Then, in the second training phase, we solve the ROM without *hyper-reduction* for $N_{train-ROM} = 30$ different parameters, to save snapshots of the residual. The transformation matrix $\mathbf{\Phi}_d$ of the residual is obtained by POD with a $tol_{POD} = 4 \cdot 10^{-4}$, leading to $m_d = 519$ basis functions, which is also the dimension of the *reduced mesh* for the mechanical *hyper*-ROM. The choices of the dimensions of the training sets, namely $N_{train} = 20$ and $N_{train-ROM} = 30$, have been derived by analyzing the trade-off between accuracy and efficiency in the construction of an *online* ROM for cardiac mechanics able to accurately approximate the solution of each new instance of the parameter $\boldsymbol{\mu}$.

In table 5.1 some results of the diagnostic of the mechanical ROM construction are displayed. Namely we consider, varying the dimension of the training sets, the CPU time to collect the snapshots of the displacement field for the N_{train} parameters; the CPU time to collect the snapshots of the nonlinear residual for the $N_{train-ROM}$ parameters; the total *offline* CPU time; and the minimum dimension of the POD spaces for the displacement field and the nonlinear term in order to achieve accurate results in the *online phase* for each new instance of the parameter. The approximation symbol in the table refers to an approximated mean over the results of different parameters tested *online*.

	Training sets (N_{train}; $N_{train-ROM}$)		
	(10; 10)	(20; 20)	(20; 30)
CPU time *offline* FOM training	14931.52s	30412.14s	30412.14s
CPU time *offline* ROM training	13242.78s	27651.9s	40148.23s
Total CPU time *offline*	28174.3s	58064.04s	70560.37s
n_d	31	31	31
m_d	965	680	519
$err_{\mathbf{d}-online}$	$\approx 10^{-3}$	$\approx 10^{-3}$	$\approx 10^{-3}$
CPU time *online*	$\approx 1250s$	$\approx 1000s$	$\approx 800s$

Table 5.1: Diagnostic on the construction of the cardiac mechanics ROM varying the dimensions of the training sets.

[1] In the training the exploration concerns the whole parameter space, thus, it is important to select values that cover as much as possible the interval of variation considered for each parameter.

In particular, from the results we can see how an higher number of interpolation points for the DEIM is required to attain accurate approximations when the *offline* phase is trained over a small amount of parameters, limiting the efficiency of the *hyper*-ROM. This is due to the fact that the variability of the solution and the nonlinear term is not sufficiently explored. This is furthermore explained in figure 5.2, where we report the singular values decay for the solution and the nonlinear term, varying the dimension of the training sets. Coherently with what we have seen at the end of section 3.1.1, we can see how, to properly model the variability of the solution over the parameter space, we need a sufficiently rich dimension of the training sets. In particular, for the solution, the variability captured by the snapshots matrix noticeably increases when we save snapshots coming from 20 different parameters instead of 10. On the other hand, for the non linear term, the singular values decay increases going from 10 to 20 parameters considered in the train, while it tends to have a similar trend for $N_{train-ROM} = 20$ and $N_{train-ROM} = 30$, meaning that the variability may stagnate and the snapshots matrix for the nonlinear term captures most of the possible behaviours varying $\boldsymbol{\mu} \in \mathcal{P}$.

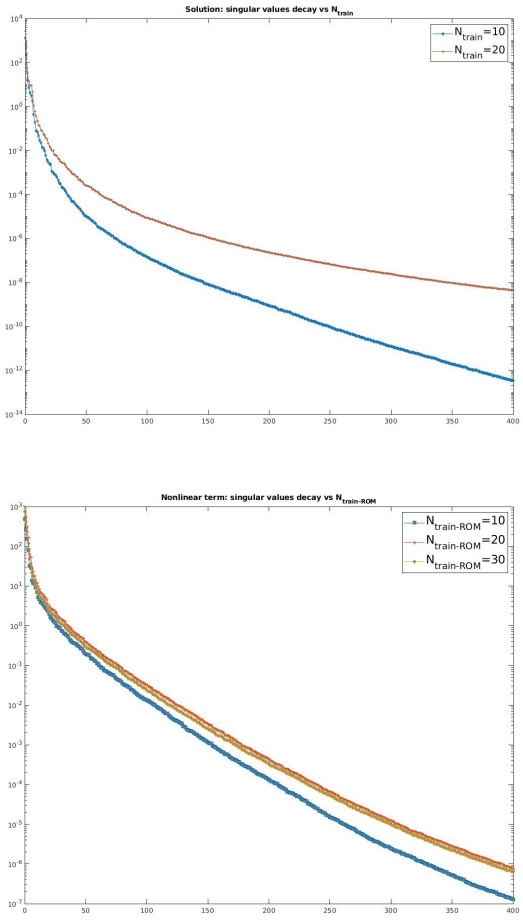

Figure 5.2: Singular values decay of the displacement (top) and the nonlinear term (bottom).

5.2.2. Test case 1: influences of the calcium ROM approximation's accuracy on the displacement

As anticipated in the previous subsection, for the mechanical activation, we consider the calcium obtained by Gappy POD reconstruction in the third test of chapter 4, a non-parametrized electrical ROM, presented in section 4.4, varying the number of basis functions employed, i.e. the POD tolerance adopted. In this first test case we evaluate the overall efficiency and accuracy of the electromechanical reduced-order model varying the accuracy in the approximation of calcium computed by the ROM for cardiac electrophysiology. This comparison can be a relevant explorative analysis before considering a parametrization of the cardiac electrophysiology ROM subproblem, since, in the latter case, the level of accuracy highly impact on the training and the efficiency of the model.
From the results displayed in table 5.1, the mechanical *hyper*-ROM that we consider for the numerical simulations in the *online* phase is the one trained on $N_{train} = 20$ and $N_{train-ROM} = 30$ parameters for the displacement and the nonlinear term, respectively, which leads to $n_d = 31$ basis functions for the displacement and $m_d = 519$ interpolation points for the DEIM.
The results are shown for the parameter $\boldsymbol{\mu} = [B = 3.5 \cdot 10^4, R = 3.5 \cdot 10^7]$, however, similar observations have been derived for other instances of the parameter $\boldsymbol{\mu} \in \mathcal{P}$.
Specifically, in table 5.2 we show the relative errors for the two electromechanical ROM built, namely coming from the two different POD tolerance considered in the construction of the cardiac electrophysiology ROM. In particular, we can see how the level of accuracy in the reconstruction of the calcium just slightly affects the accuracy of the approximation of the displacement field by the cardiac mechanics ROM, in fact both the displacement approximations in the *online mechanical ROM* show a mean relative error of order 10^{-3}.
This is furthermore shown in figures 5.3, 5.4, 5.5 and 5.6, where we display the solutions at time $35ms$, $70ms$, $140ms$ and $210ms$, respectively. In fact, in the figures, there are no differences in the evolution of the two solutions, considering the two approximations of the calcium concentration. Thus, an accuracy of order $\approx 10^{-2}$ in the ROM approximation of the ionic variable w_3 is sufficient to show the effects of the intracellular calcium concentration in the cardiac deformation.

Relative errors	POD tolerance electrophysiology	
	10^{-2}	10^{-3}
$\text{err}_{w3-Gappy}$	$5.31 \cdot 10^{-2}$	$4.03 \cdot 10^{-3}$
$\text{err}_{\mathbf{d}-online}$	$3.1 \cdot 10^{-3}$	$2.89 \cdot 10^{-3}$

Table 5.2: Relative errors of the calcium concentration, varying the POD tolerance for the cardiac electrophysiology ROM, and of the corresponding displacement.

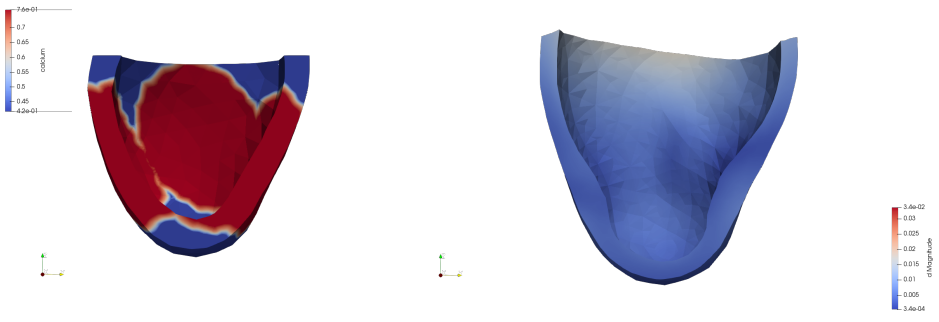

(a) ROM, $tol_{POD} = 10^{-2}$ (b) ROM mechanics

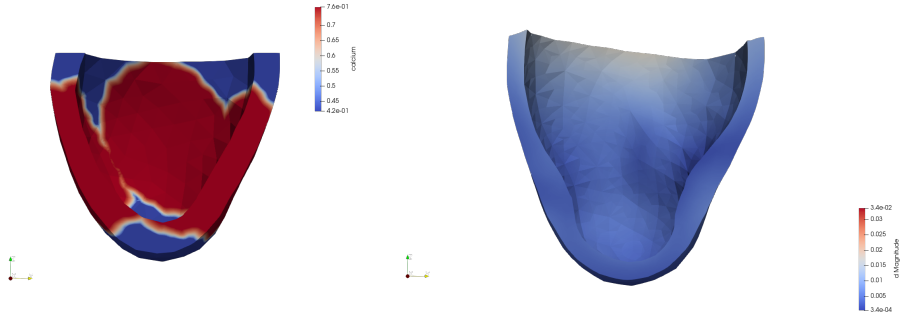

(c) ROM, $tol_{POD} = 10^{-3}$ (d) ROM mechanics

Figure 5.3: Comparison between the electromechanical *hyper*-ROM built with a $tol_{POD} = 10^{-2}$ (first row) and with a $tol_{POD} = 10^{-2}$ (second row) for the cardiac electrophysiology subproblem. The calcium (left) and the corresponding cardiac mechanical deformation (right) are snapshots taken at t=35ms.

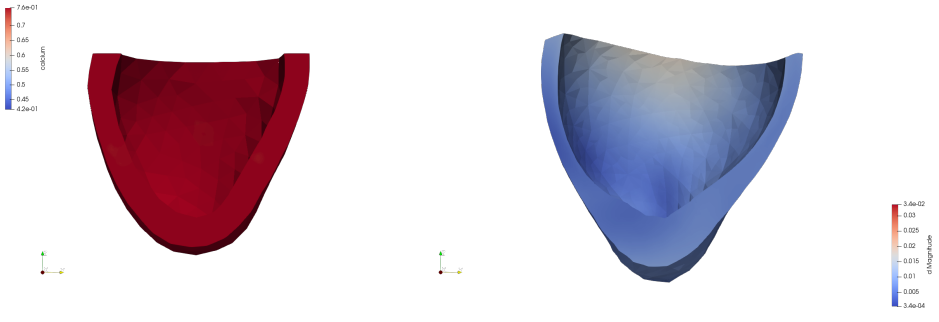

(a) ROM, $tol_{POD} = 10^{-2}$ (b) ROM mechanics

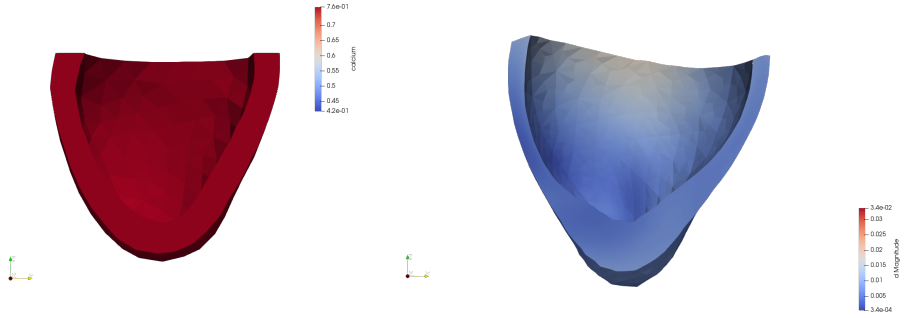

(c) ROM, $tol_{POD} = 10^{-3}$ (d) ROM mechanics

Figure 5.4: Comparison between the electromechanical *hyper*-ROM built with a $tol_{POD} = 10^{-2}$ (first row) and with a $tol_{POD} = 10^{-2}$ (second row) for the cardiac electrophysiology subproblem. The calcium (left) and the corresponding cardiac mechanical deformation (right) are snapshots taken at t=70ms.

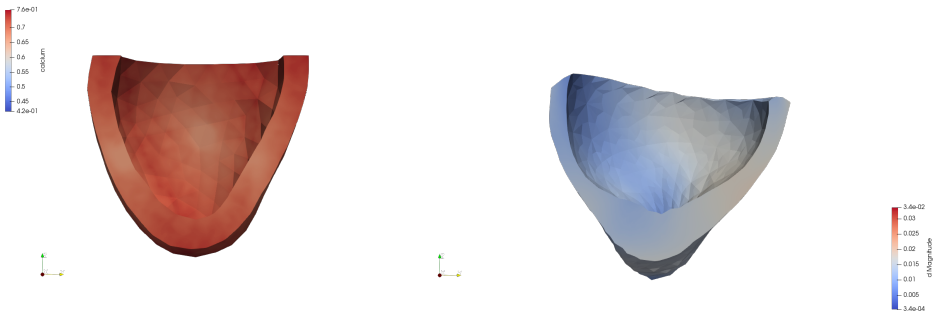

(a) ROM, $tol_{POD} = 10^{-2}$ (b) ROM mechanics

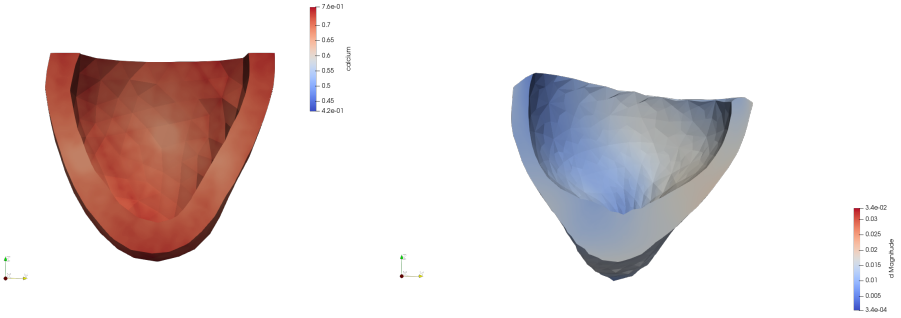

(c) ROM, $tol_{POD} = 10^{-3}$ (d) ROM mechanics

Figure 5.5: Comparison between the electromechanical *hyper*-ROM built with a $tol_{POD} = 10^{-2}$ (first row) and with a $tol_{POD} = 10^{-2}$ (second row) for the cardiac electrophysiology subproblem. The calcium (left) and the corresponding cardiac mechanical deformation (right) are snapshots taken at t=140ms.

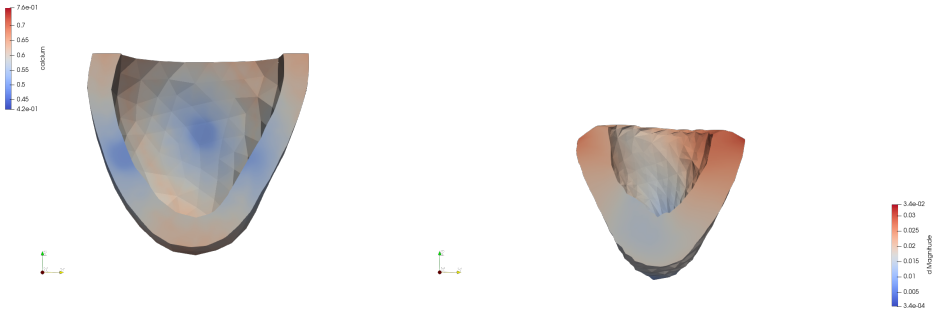

(a) ROM, $tol_{POD} = 10^{-2}$ (b) ROM mechanics

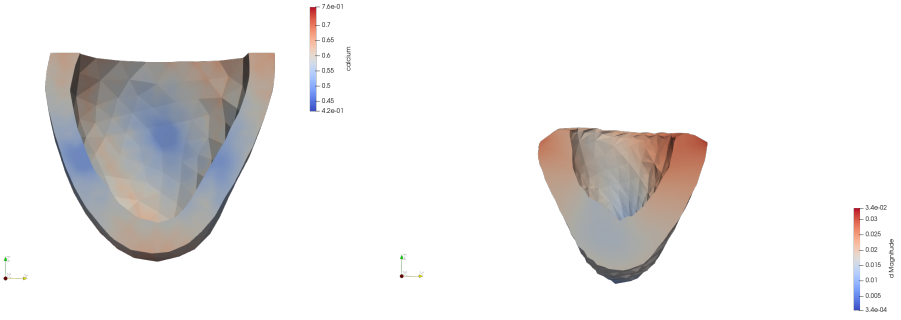

(c) ROM, $tol_{POD} = 10^{-3}$ (d) ROM mechanics

Figure 5.6: Comparison between the electromechanical *hyper*-ROM built with a $tol_{POD} = 10^{-2}$ (first row) and with a $tol_{POD} = 10^{-2}$ (second row) for the cardiac electrophysiology subproblem. The calcium (left) and the corresponding cardiac mechanical deformation (right) are snapshots taken at t=210ms.

CPU time and *hyper-reduction* speed up	POD tolerance electrophysiology	
	10^{-2}	10^{-3}
Electrophysiology:		
FOM	16878.27s	17203.32s
hyper-ROM	5464.27s	5918.24s
Speed up	3.09	2.91
Mechanics:		
FOM	1588.43s	1631.2s
hyper-ROM	777.26s	821.35s
Speed up	2.04	1.99
Electromechanics:		
FOM	18466.7s	18834.52s
hyper-ROM	6241.53s	6739.59s
Overall speed up	2.96	2.79

Table 5.3: CPU time of the full-order models and the reduced-order models, and speed up of the *online* ROM with respect to the FOM in the electromechanics simulation, varying the POD tolerance adopted to build the cardiac electrophysiology ROM subproblem.

In table 5.3, we instead compare the overall efficiency of the electromechanical ROM in the two different cases considered. In particular, since the accuracy of the solutions is high for both the two ROM approximations, it is important to address to the overall efficiency of the models.
In order to evaluate the speedup for the mechanical problem, we just relied on the time related to the assembling of the systems and to their resolution, removing the CPU time concerning everything not related to the order reduction, such as the computation of the left ventricle volume, about $16s$ in total, and the solution of the activation model, about $60s$ in total, which are comparable for the FOM and the *hyper*-ROM simulations. The results show that the speedup for the mechanical *hyper*-ROM is similar, around $2x$ in the two cases considered. However, the difference is particularly relevant in the cardiac electrophysiology *online* phase. In fact, the dimension of the POD spaces obtained by varying the POD tolerance in the construction of the electrophysiology ROM, see table 4.6, highly influence the speedup of the electrical *hyper*-ROM simulation with respect to the FOM simulation, as we have seen in figure 4.15. This also affects, as a consequence, the overall speedup of the one-way coupled electromechanical ROM, yielding to prefer the most efficient reduced-order model for both the subproblems, when the accuracy can be considered comparable. Namely, the case of intracellular calcium concentration obtained with a $tol_{POD} = 10^{-2}$ brings an overall speedup of the electromechanical ROM of almost $3x$ with respect to the FOM, while the case of intracellular calcium concentration obtained with a $tol_{POD} = 10^{-3}$ brings a speedup of $2.79x$ with respect to FOM.

5.2.3. Second test: Efficient evaluation of the cardiac deformation under parameter variations

From the results obtained in the previous subsection, we develop the one-way parametrized electromechanical ROM considering, for the mechanical activation, a calcium obtained with a $tol_{POD} = 10^{-2}$ in the electrophysiology *hyper*-ROM. Then, the mechanical *hyper*-ROM is the one obtained in the *offline* phase with $N_{train} = 20$ and $N_{train-ROM} = 30$ parameters for the solution and the nonlinear term, respectively. Namely, as seen in table 5.1, we use $n_d = 31$ basis functions to approximate the displacement and $m_d = 519$ interpolation points to assemble the Jacobian $J_{\mathbf{d},\mathbf{d}}$ and the residual $r_{\mathbf{d}}$ at each iteration of the Newton method, at each time-step.
The test has been performed over $N_{test} = 15$ new, different parameters than the one considered for the train. In particular, we want to show the high quality approximations of the parametrized electromechanical ROM in terms of efficiency and accuracy with respect to the high fidelity solutions, under the variation of parameters coming from the mechanical subproblem, remarking the importance of efficient numerical approximations in the cardiac electromechanics framework.
In table 5.4 we present the mean of the relative error in the approximation of the displacement field over the $N_{test} = 15$ parameters tested, namely we define it as

$$\overline{err}_{\mathbf{d}-online} = \frac{1}{N_{test}} \sum_{i=1}^{N_{test}} err_{\mathbf{d}-online}(\boldsymbol{\mu}_i).$$

Moreover, we also show the mean computational time for the FOM simulation and the ROM simulation of the mechanical subproblem. In terms of efficiency, with the ROM setup presented in the subsection 5.2.1, we gain a mean speedup of $2x$ with respect of the cardiac mechanics FOM.

Mean relative error over the $N_{test} = 15$ parameters	
$\overline{err}_{\mathbf{d}-online}$	$4.02{\cdot}10^{-3}$
Mean CPU time mechanical subproblem:	
CPU time FOM	1628.74s
CPU time *hyper*-ROM	812.01s
Speed up	2.01

Table 5.4: Mean of the relative error for the displacement field ROM approximation and the CPU time of the FOM and *hyper*-ROM simulations over the $N_{test} = 15$ parameters.

Mean CPU time at each Newton iteration	FOM	*hyper*-ROM
Assembling system	2.73s	1.42s
Solving Newton step	$3.51 \cdot 10^{-1} s$	$2.69 \cdot 10^{-3} s$

Table 5.5: Mean CPU time costs of assembling and solving the algebraic mechanical system at each Newton interation, comparison between FOM and *hyper*-ROM.

In particular, the speedup is mainly related to the assembling of the nonlinear terms and to the solution of the Newton step at each iteration of the method; in fact, the algebraic system assembled and solved in the *hyper*-ROM, Eq. (3.18) or (3.19), is of low-dimension with respect to FOM, Eq. (3.12) or (3.13). This is shown in table 5.5, where we report the mean CPU time costs of assembling and solving the system at each Newton iteration, comparing the two numerical approximations approaches.

On the other hand, in terms of accuracy, we obtain high-quality approximations for each new instance of the parameter $\boldsymbol{\mu} \in \mathcal{P}$, with a mean relative error over the different parameters tested of the order of 10^{-3}.
In figures 5.7, 5.8, 5.9, 5.10 we show a comparison between the FOM solution and the ROM solution for two different parameters $\boldsymbol{\mu}_{10}$ and $\boldsymbol{\mu}_{14}$, at $35ms$, $70ms$, $140ms$, $210ms$, respectively. The two parameters are $\boldsymbol{\mu}_{10} = [6.67 \cdot 10^4, 3.1 \cdot 10^7]$, where we consider an higher Bulk modulus than the one shown in the previous section, and $\boldsymbol{\mu}_{14} = [3 \cdot 10^4, 4.43 \cdot 10^7]$, where, on the other hand, we consider an higher peripheral resistence.
The accuracy of the solution of the mechanical ROM subproblem in the *online* phase for the two different new instances of the parameter $\boldsymbol{\mu}$ is furthermore shown in figure 5.11, where we display the relative error in space, at each time-step, for the displacement field ROM approximation. In particular, the relative error in space for the solution obtained with the parameter $\boldsymbol{\mu}_{10}$ is of the order 10^{-3} at almost all the time-steps, while the one related to the solution obtained with the parameter $\boldsymbol{\mu}_{14}$ is at least of the order 10^{-2}, remarking the highly accurate approximations for the solutions under parameter variations.

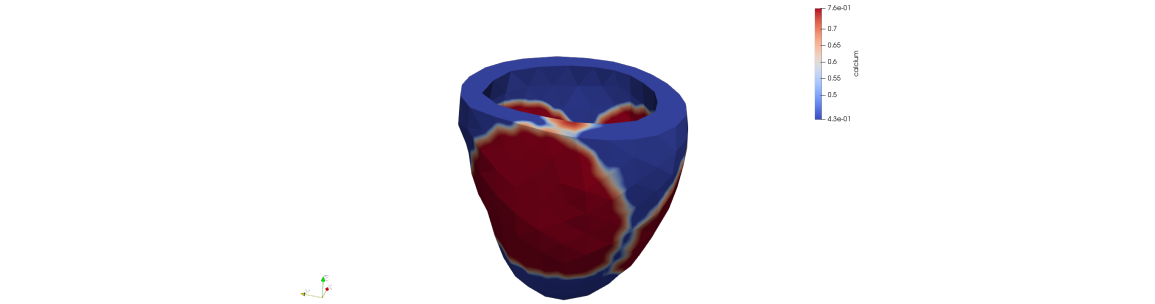

(a) ROM electrophysiology

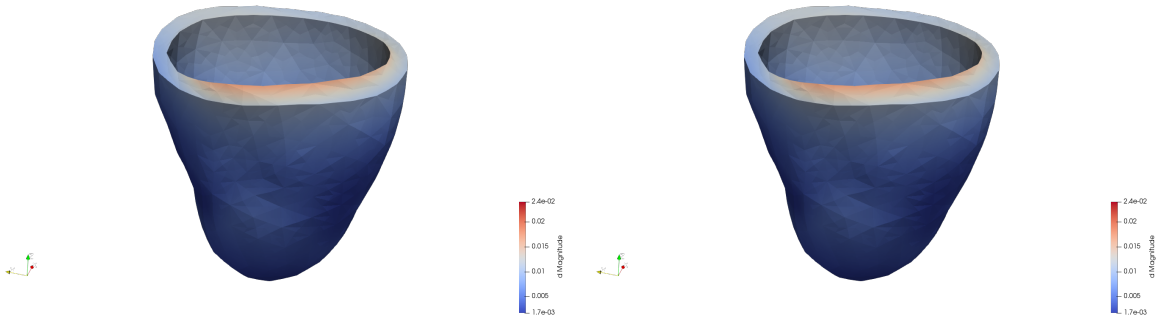

(b) $\boldsymbol{\mu}_{10}$-FOM mechanics

(c) $\boldsymbol{\mu}_{10}$-ROM mechanics

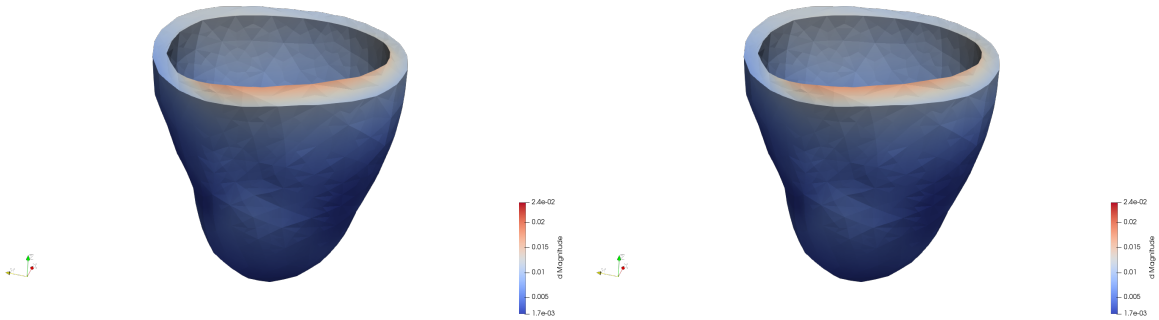

(d) $\boldsymbol{\mu}_{14}$-FOM mechanics

(e) $\boldsymbol{\mu}_{14}$-ROM mechanics

Figure 5.7: Comparison between the displacement field magnitude obtained by the FOM (left) and obtained by the ROM *online* phase (right) for the two parameters $\boldsymbol{\mu}_{10}$ (center) and $\boldsymbol{\mu}_{14}$ (bottom), at time 35ms. The calcium (on the top) , displayed in the reference configuration Ω_0, is the one adopted for the computation of the active tension in the cardiac mechanics subproblem.

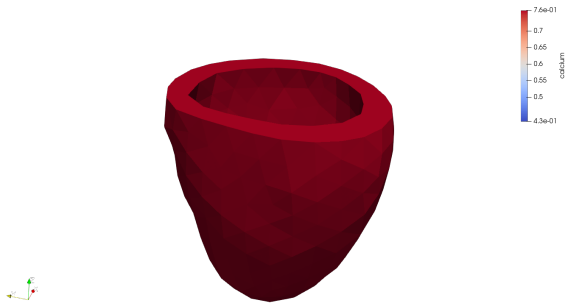

(a) ROM electrophysiology

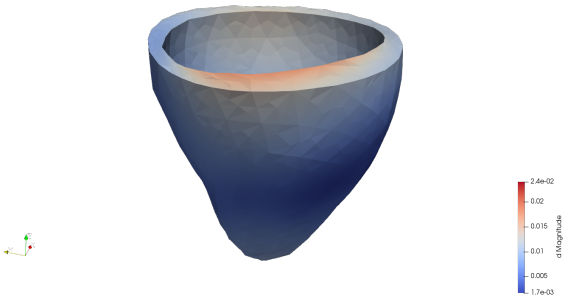

(b) $\boldsymbol{\mu}_{10}$-FOM mechanics

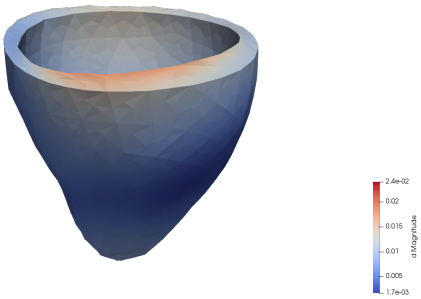

(c) $\boldsymbol{\mu}_{10}$-ROM mechanics

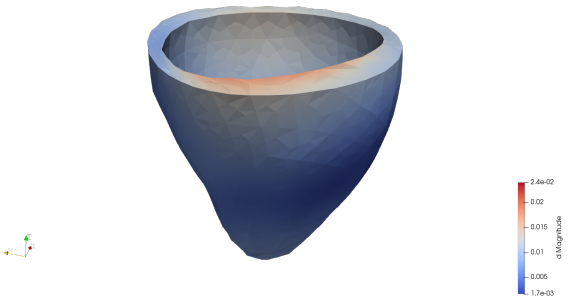

(d) $\boldsymbol{\mu}_{14}$-FOM mechanics

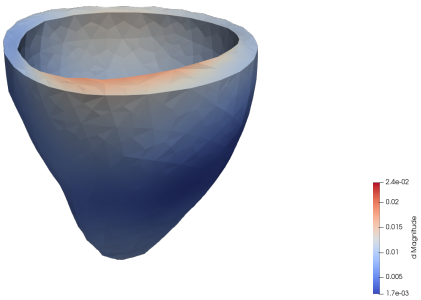

(e) $\boldsymbol{\mu}_{14}$-ROM mechanics

Figure 5.8: Comparison between the displacement field magnitude obtained by the FOM (left) and obtained by the ROM *online* phase (right) for the two parameters $\boldsymbol{\mu}_{10}$ (center) and $\boldsymbol{\mu}_{14}$ (bottom), at time 70ms. The calcium (on the top) , displayed in the reference configuration Ω_0, is the one adopted for the computation of the active tension in the cardiac mechanics subproblem.

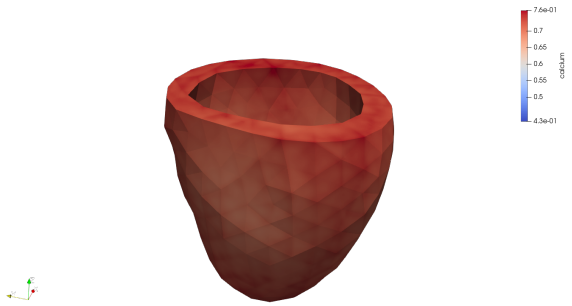

(a) ROM electrophysiology

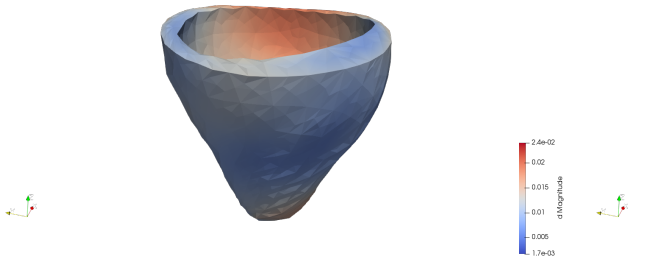

(b) $\boldsymbol{\mu}_{10}$-FOM mechanics

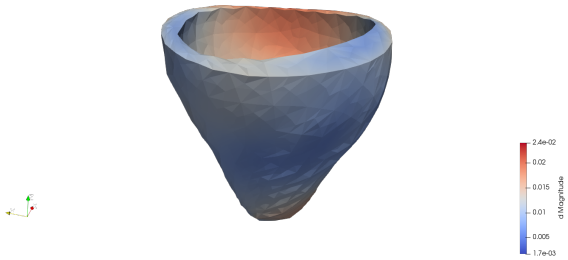

(c) $\boldsymbol{\mu}_{10}$-ROM mechanics

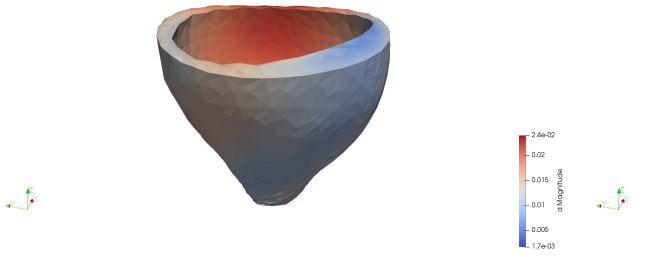

(d) $\boldsymbol{\mu}_{14}$-FOM mechanics

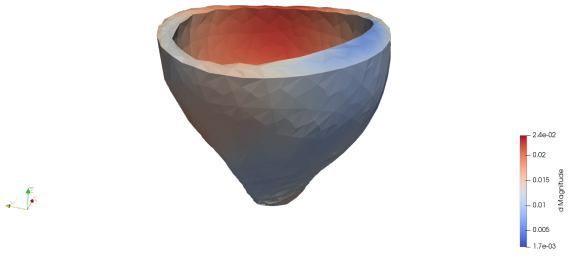

(e) $\boldsymbol{\mu}_{14}$-ROM mechanics

Figure 5.9: Comparison between the displacement field magnitude obtained by the FOM (left) and obtained by the ROM *online* phase (right) for the two parameters $\boldsymbol{\mu}_{10}$ (center) and $\boldsymbol{\mu}_{14}$ (bottom), at time 140ms. The calcium (on the top) , displayed in the reference configuration Ω_0, is the one adopted for the computation of the active tension in the cardiac mechanics subproblem.

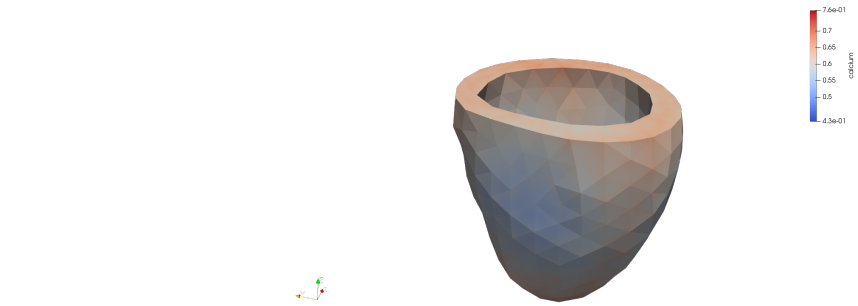

(a) ROM electrophysiology

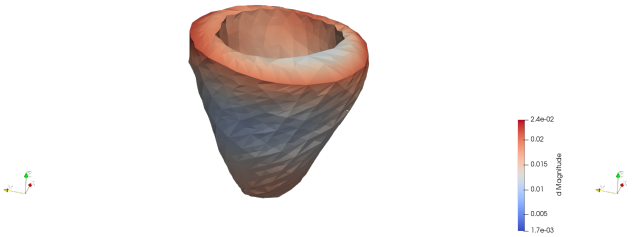

(b) $\boldsymbol{\mu}_{10}$-FOM mechanics

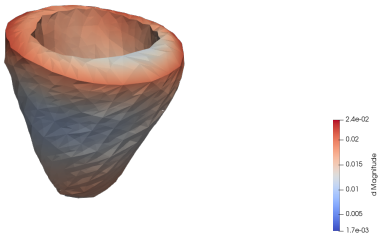

(c) $\boldsymbol{\mu}_{10}$-ROM mechanics

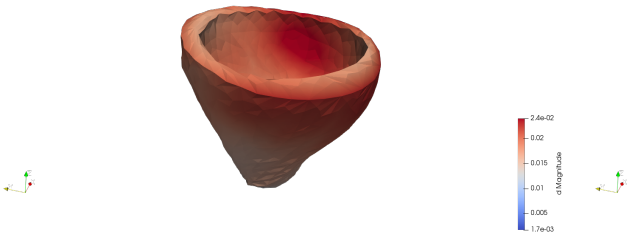

(d) $\boldsymbol{\mu}_{14}$-FOM mechanics

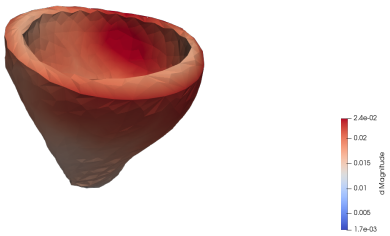

(e) $\boldsymbol{\mu}_{14}$-ROM mechanics

Figure 5.10: Comparison between the displacement field magnitude obtained by the FOM (left) and obtained by the ROM *online* phase (right) for the two parameters $\boldsymbol{\mu}_{10}$ (center) and $\boldsymbol{\mu}_{14}$ (bottom), at time 210ms. The calcium (on the top) , displayed in the reference configuration Ω_0, is the one adopted for the computation of the active tension in the cardiac mechanics subproblem.

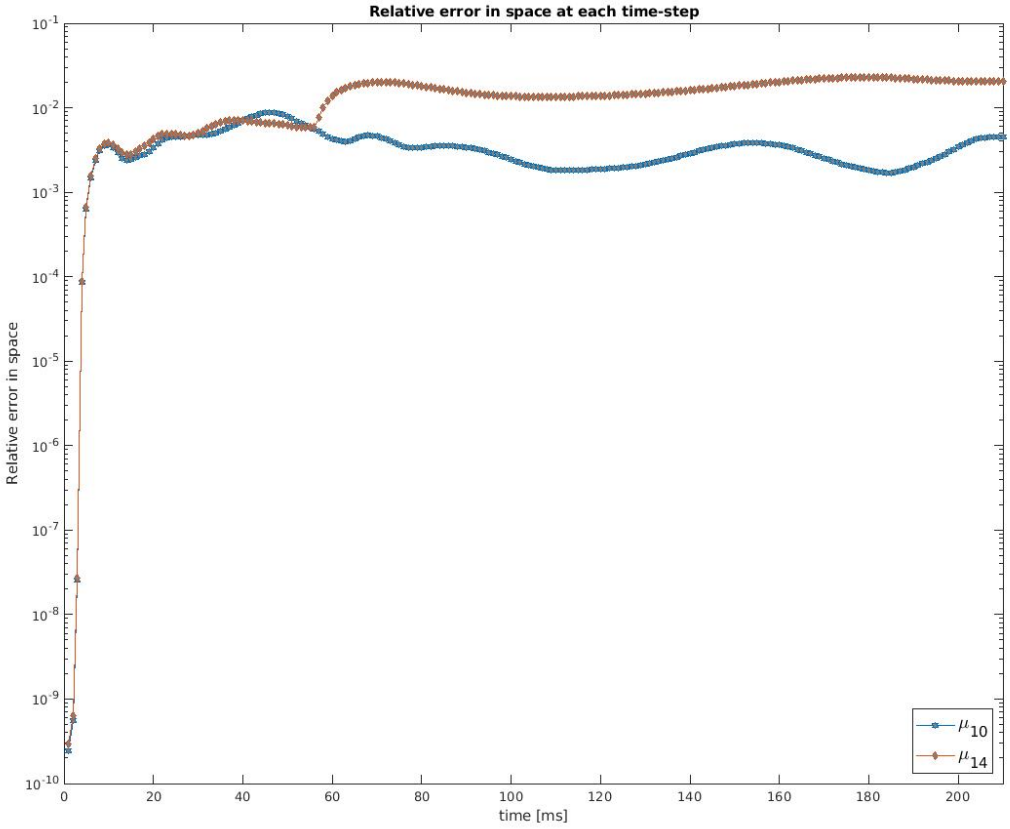

Figure 5.11: Relative error in space at each time-step of the displacement field varying the parameter $\boldsymbol{\mu}$

Conclusions

In this work we presented an efficient numerical approximation, by reduced-order modeling, of parametrized problems in cardiac electromechanics. In particular, for what concerns cardiac electrophysiology, we developed an efficient evaluation of the ionic variables in the monodomain problem. This has been possible by means of the gappy proper orthogonal decomposition method, which is able to accurately reconstruct the ionic variables in the original domain at each time-step, for each parameter considered, from their reduced-order gappy approximations computed in the *online* phase of the electrical parametrized ROM. Specifically, in chapter 4 we showed how the accuracy in the reconstruction of the the ionic variables is characterized by a mean relative error of order at least of 10^{-2}, with a proper tuning of the reduced-order model. Moreover, in terms of efficiency, we gained a speedup in the *online* phase of 1.52 with respect to FOM in the case of a slab domain, while even more relevant results have been achieved for the more complex domain represented by the left ventricle, where the *hyper-reduced* ROM simulation was 3 times faster than the full order one. The cost-effective evaluation of the ionic variables introduced, in particular of the intracellular calcium concentration, has been an extremely important result in the development of a parametrized one-way coupled electromechanical reduced-order model.
In fact, the tests presented in chapter 5 show how the latter is capable to find accurate solutions under parameters variations affecting the cardiac mechanics at reduced computational costs. Namely, the mean relative error for the displacement approximation found is of the order of 10^{-3} for all the parameters tested in the mechanical *online* phase, while the total speedup in the simulations related to the coupling of the two *hyper-reduced*-order models has been of $3x$ with respect to the coupling of the respective full order models.

The achievements of this work represent a preliminary investigation of efficient numerical approximations for parametrized problems in cardiac electromechanics. In particular, the model introduced allows to consider parametrizations coming both from cardiac electrophysiology and cardiac mechanics, in order to also understand how variations of the electrical propagation influence the mechanical activation in each heartbeat. However, as we have seen in section 4.3, the construction of an efficient parametrized electrophysiology reduced-order model represented a challenging task when relying on a global ROM strategy, as we did in this work. This is mainly due to the nature of the electrophysiology

problem, which is characterized by the propagation of a very steep wave, that requires the assembling of huge matrices when considering the full order modeling and large sets of basis functions to approximate the solutions when relying on a global reduced-order modeling strategy. Thus, a possible development of this work can be to adopt different strategies in the construction of the ROM for cardiac electrophysiology, such as, e.g., a local ROM strategy, where the solution can be better approximated in a lower-dimensional subspace generated by local basis vectors, rather than in a unique subspace spanned by global basis vectors, enhancing the efficiency of reduced-order modeling.
Moreover, another relevant development can be related to the inclusion of more complete activation models as well as to the introduction of a *mechano-electrical feedback* in order to develop a fully coupled, and even more reliable, electromechanical ROM for real cases simulating physiological and pathological scenarios of real life interest.

Bibliography

[1] Pagani S., Manzoni A., Quarteroni A. (2018). *Numerical approximation of parametrized problems in cardiac electrophysiology by a local reduced basis method.* Computer Methods in Applied Mechanics and Engineering, 340, 530-558.

[2] Bueno-Orovio A., Cherry E., Fenton F. (2008). *Minimal model for human ventricular action potentials in tissue.* J. Theor. Biol. 253(3), 544–560.

[3] Manzoni A., Bonomi D., Quarteroni A. (2018). *Reduced Order Modeling for Cardiac Electrophysiology and Mechanics: New Methodologies, Challenges and Perspectives.* In Mathematical and Numerical Modeling of the Cardiovascular System and Applications (pp. 115-166). Springer, Cham.

[4] Carlberg K., Bou-Mosleh C., Farhat C. (2011). *Efficient non-linear model reduction via a least-squares Petrov–Galerkin projection and compressive tensor approximations.* Int. J. Numer. Meth. Engng., 86: 155-181.

[5] Colli Franzone P., Pavarino L.F., Scacchi S. (2018). *Electro-Mechanical Modeling and Simulation of Reentry Phenomena in the Presence of Myocardial Infarction.* In: Boffi D., Pavarino L., Rozza G., Scacchi S., Vergara C. (eds) Mathematical and Numerical Modeling of the Cardiovascular System and Applications. SEMA SIMAI Springer Series, vol 16. Springer, Cham.

[6] Quarteroni A., Dede' L., Manzoni A., Vergara C. (2019). *Mathematical Modelling of the Human Cardiovascular System: Data, Numerical Approximation, Clinical Applications.* Cambridge: Cambridge University Press.

[7] Sirovich L., (1987). *Method of snapshots.* Quarterly of applied mathematical, Vol. 45, No. 3, pp. 561–571.

[8] Peherstorfer B., Drmac Z., Gugercin S. (2020). *Stability of discrete empirical interpolation and gappy proper orthogonal decomposition with randomized and deterministic sampling points.* SIAM Journal on Scientific Computing, 42(5), A2837-A2864.

[9] Choi Y., Carlberg K. (2019). *Space-time least-squares Petrov-Galerkin projection for nonlinear model reduction.* SIAM Journal on Scientific Computing, 41(1), A26-A58.

[10] Amsallem D., Zahr M.J., Farhat C. (2012). *Nonlinear model order reduction based on local reduced-order bases.* Internat. J. Numer. Methods Engrg. 92 (10) 891–916.

[11] Washabaugh K., Amsallem D., Zahr M., Farhat C. (2012). *Nonlinear model reduction for cfd problems using local reduced order bases.* AIAA Paper 2012–2686, 2012, pp. 1–16.

[12] Pathmanathan P., Mirams G.R., Southern J. and Whiteley J.P. (2011). *The significant effect of the choice of ionic current integration method in cardiac electro-physiological simulations.* Int. J. Numer. Meth. Biomed. Engng., 27: 1751-1770.

[13] Willcox K. (2006). *Unsteady flow sensing and estimation via the gappy proper orthogonal decomposition.* Computers fluids, 35(2), 208-226.

[14] Carlberg K., Farhat C., Cortial J., Amsallem D. (2013). *The GNAT method for nonlinear model reduction: effective implementation and application to computational fluid dynamics and turbulent flows.* Journal of Computational Physics, 242, 623-647.

[15] Abgrall R., Amsallem D. (2015). *Robust Model Reduction by L^1-norm Minimization and Approximation via Dictionaries: Application to Linear and Nonlinear Hyperbolic Problems.* Advanced Modeling and Simulation in Engineering Sciences. 3. 10.1186/s40323-015-0055-3.

[16] Quarteroni A, Manzoni A, Negri F. (2015) *Reduced basis methods for partial differential equations: an introduction.* Vol. 92. Springer.

[17] Guccione J. M., McCulloch A. D., Waldman L. K. (1991). *Passive material properties of intact ventricular myocardium determined from a cylindrical model.* J Biomech Eng. 1991 Feb;113(1):42-55.

[18] Guccione J. M., McCulloch A. D. (1991). *Finite element modeling of ventricular mechanics.* In: Theory of Heart. Springer, pp. 121–144.

[19] Ogden R. W. (1997). *Non-linear elastic deformations.* Courier Corporation.

[20] Ambrosi D., Pezzuto S.(2012) *Active stress vs. active strain in mechanobiology: constitutive issues.* J. Elast. 107(2), 199–212

[21] Regazzoni F., Dedè L., Quarteroni A. (2020). *Machine learning of multiscale active force generation models for the efficient simulation of cardiac electromechanics".* In: Computer Methods in Applied Mechanics and Engineering 370 (2020), p. 113268.

[22] Ruiz-Baier R., Gizzi A., Rossi S., et al. (2014). *Mathematical modelling of active contraction in isolated cardiomyocytes.* In: Mathematical Medicine and Biology: a Journal of the IMA 31, pp. 259–283.

[23] Rossi S., Lassila T., Ruiz-Baier R., et al. (2014). *Thermodynamically consistent orthotropic activation model capturing ventricular systolic wall thickening in cardiac electromechanics.* In: European Journal of Mechanics - A/Solids 48, pp. 129–142.

[24] Barbarotta L., Dede L., Rossi S., Quarteroni A. (2018) *A Transmurally Heterogeneous Orthotropic Activation Model for Ventricular Contraction and its Numerical Validation.* International journal for numerical methods in biomedical engineering. 34. 10.1002/cnm.3137.

[25] Regazzoni F., Salvador M., Africa P.c., Fedele M., Dede' L., Quarteroni A. (2020). *A cardiac electromechanics model coupled with a lumped parameters model for closed-loop blood circulation. Part I: model derivation.* ArXiv preprint arXiv:2011.15040

[26] Regazzoni F., Salvador M., Africa P.c., Fedele M., Dede' L., Quarteroni, A. (2020). *A cardiac electromechanics model coupled with a lumped parameters model for closed-loop blood circulation. Part II: numerical approximation.* ArXiv preprint arXiv:2011.15051

[27] Colli Franzone P., Pavarino L.F., Scacchi S. (2015). *Parallel multilevel solvers for the cardiac electromechanical coupling.* Appl. Numer. Math. 95, 140–153.

[28] Göktepe S., Kuhl E. (2010). *Electromechanics of the heart: a unified approach to the strongly coupled excitation–contraction problem.* Comput. Mech. 45(2–3), 227–243.

[29] Rossi S. (2014). *Anisotropic modeling of cardiac mechanical activation.* Ph.D. thesis, Ecole Polytechnique Fédérale de Lausanne.

[30] Holzapfel G., Ogden R. (2009). *Constitutive modelling of passive myocardium: a structurally based framework for material characterization.* Philos. Trans. A Math. Phys. Eng. Sci. 367, 3445–3475.

[31] Regazzoni F., Dedè L., Quarteroni A. (2020). *Biophysically detailed mathematical models of multiscale cardiac active mechanics.* PLOS Computational Biology 16(10): e1008294.

[32] Kentish J.C., ter Keurs H.E., Ricciardi L., Bucx J.J., Noble M.I. (1986). *Comparison between the sarcomere length-force relations of intact and skinned trabeculae from rat right ventricle. Influence of calcium concentrations on these relations.* Circulation Research. 58(6):755–768. pmid:371992.

[33] Walker J.S., Li X., Buttrick P.M. (2010). *Analysing force-pCa curves.* J Muscle Res Cell Motil. 2010 Jul;31(1):59-69. Epub 2010 May 20.

[34] Sun, Y. B., Irving, M. (2010). *The molecular basis of the steep force-calcium relation in heart muscle.* Journal of molecular and cellular cardiology, 48(5), 859–865. https://doi.org/10.1016/j.yjmcc.2009.11.019.

[35] Quarteroni A., Manzoni A., Vergara C. (2017). *The cardiovascular system: mathematical modeling, numerical algorithms, clinical applications.* Acta Numer. 26, 365–590.

[36] Geselowitz D.B., Miller W.T. (1983). *A bidomain model for anisotropic cardiac muscle. Ann. Biomed.* Eng. 11, 191–206.

[37] Pennacchio M., Savaré G., Colli Franzone P. (2006). *Multiscale modeling for the bioelectric activity of the heart.* SIAM J. Math. Anal. 37, 1333–1370.

[38] Colli Franzone P., Pavarino, B. Taccardi L. (2005). *Simulating patterns of excitation, repolarization and action potential duration with cardiac bidomain and monodomain models* Math. Biosci. 197 (1) 35–66.

[39] Clayton R., Panfilov A. (2008). *A guide to modelling cardiac electrical activity in anatomically detailed ventricles.* Prog. Biophys. Mol. Biol. 96(1), 19–43.

[40] Potse M., Dubé B., Vinet A., Cardinal R. (2006). *A comparison of monodomain and bidomain propagation models for the human heart.* Conf. Proc. IEEE Eng. Med. Biol. Soc. 53(12), 3895–3898.

[41] Tagliabue A., Dedè L., Quarteroni A. (2017). *Fluid dynamics of an idealized left ventricle: the extended Nitsche's method for the treatment of heart valves as mixed time varying boundary conditions.* Int. J. Numer. Methods Fluids 85(3), 135–164.

[42] Tagliabue A., Dedè L., Quarteroni A. (2017). *Complex blood flow patterns in an idealized left ventricle: A numerical study.* Chaos 27(9), 093939.

[43] Gerbi A., Dedè L., Quarteroni A. (2019). *A monolithic algorithm for the simulation of cardiac electromechanics in the human left ventricle.* Mathematics in Engineering, 1(1): 1-37.

[44] Westerhof N., Lankhaar J.W., Westerhof B.E. (2009). *The arterial Windkessel.* Med. Biol. Eng. Comput. 47 (2) 131–141.

[45] Z. M. G. Inc. (2014) *Zygote Solid 3D heart Generation II Development Report.* Technical Report.

[46] Eriksson T., Prassl A.J., Plank G., Holzapfel G. (2013). *Influence of myocardial fiber/sheet orientations on left ventricular mechanical contraction.* Mathematics and Mechanics of Solids. 18:592-606.

[47] Chabiniok R., Wang V., Hadjicharalambous M., Asner L., Lee J., Sermesant M., Kuhl E., Young A., Moireau P., Nash M., Chapelle D., and Nordsletten D. (2016). *Multiphysics and multiscale modelling, data–model fusion and integration of organ physiology in the clinic: ventricular cardiac mechanics.* In: Interface Focus 6.2 , p. 20150083.

[48] Colli Franzone P., Pavarino L.F., and Scacchi S. (2018). *A Numerical Study of Scalable Cardiac Electro-Mechanical Solvers on HPC Architectures.* In: Frontiers in Physiology 9, p. 268.

[49] Colli Franzone P., Pavarino L.F., and Scacchi S. (2016). *Bioelectrical effects of mechanical feedbacks in a strongly coupled cardiac electro-mechanical model.* Mathematical Models and Methods in Applied SciencesVol. 26, No. 01, pp. 27-57

[50] Colli Franzone P., Pavarino L. F., Scacchi, S. (2016). *Joint influence of transmural heterogeneities and wall deformation on cardiac bioelectrical activity: A simulation study.* Mathematical biosciences, 280, 71-86.

[51] Bayer J.D., Blake R.C., Plank G., et al. (2012) *A Novel Rule-Based Algorithm for Assigning Myocardial Fiber Orientation to Computational Heart Models.* Ann Biomed Eng 40, 2243–2254. https://doi.org/10.1007/s10439-012-0593-5

A | Models parameters

Here we present further details on the parameters of the models presented in chapter 1. In table A.1 we report the parameters considered for the Bueno-Orovio model (1.2).

Parameter	value	Parameter	value
C_m	1	$\tau_{w_3,1}$	$2.7342{\cdot}10^{-3}s^{-1}$
θ_{w_1}	0.3	$\tau_{w_3,2}$	0.003 s^{-1}
$\theta^-_{w_1}$	0.015	$\tau_{0,1}$	$6{\cdot}10^{-3}s^{-1}$
$\tau^+_{w_1}$	$1.4506{\cdot}10^{-3}s^{-1}$	$\tau_{0,2}$	$6{\cdot}10^{-3}s^{-1}$
$\tau^-_{w_1,1}$	0.06 s^{-1}	$\tau^-_{w_1,2}$	1.15 s^{-1}
θ_{w_2}	0.015	u_{w_3}	0.9087
$\tau^+_{w_2}$	0.28 s^{-1}	k_{w_3}	2.0994
$\tau^-_{w_2,1}$	0.07 s^{-1}	$u^-_{w_2}$	0.03
$\tau^-_{w_2,2}$	0.02 s^{-1}	$k^-_{w_2}$	65
u_{so}	0.65	θ_0	0.006
c_u	1.58	$w^*_{2,\infty}$	0.94
τ_{fi}	$1.1{\cdot}10^{-4}s^{-1}$	$\tau_{w_2,\infty}$	0.07 s^{-1}
$\tau_{so,1}$	$4.3{\cdot}10^{-2}s^{-1}$	τ_{si}	$2.8723{\cdot}10^{-3}s^{-1}$
$\tau_{so,2}$	$2{\cdot}10^{-4}s^{-1}$	k_{so}	2.0

Table A.1: Bueno-Orovio model parameters

In table A.2 we report the parameters of the Guccione strain energy function (1.7) adopted for the passive mechanics (1.6).

Parameter	value
b_{ff}	8
b_{ss}	6
b_{nn}	3
b_{fs}	12
b_{fn}	3
b_{sn}	3
B (bulk)	$[2.5{\cdot}10^4, 7.5 \cdot 10^4]Pa$
c	$8.8{\cdot}10^2 Pa$
ρ $(tissue\ density)$	$10^3 kg/m^3$
$K_{\perp}^{epi}$	$2{\cdot}10^5 Pa/m$
$K_{\parallel}^{epi}$	$2{\cdot}10^4 Pa/m$
$C_{\perp}^{epi}$	$2{\cdot}10^4 Pa/m$
$C_{\parallel}^{epi}$	$2{\cdot}10^2 Pa/m$

Table A.2: Guccione strain energy function and mechanical model parameters

In table A.3 we report the parameters of the activation model (1.10) adopted for the active mechanics.

Parameter	value
τ	0.05
T_a^{max}	10000 Pa
EC_{50}	0.8 μM
n_H	5

Table A.3: Activation model parameters

Finally, in table A.4 we report the parameters of the lumped parameter model and the values of the pressure in the different phases of the blood circulation closed-loop 1.2.3.

Pressure		
	Variable	value
Phase 0 initial pressure (end-diastolic pressure LV)	p_{ED}	1333 Pa
Phase 1 initial pressure (aortic valve opening pressure LV)	p_{AVO}	11000 Pa
Phase 3 initial pressure (mitral valve opening pressure LV)	p_{MVO}	667 Pa
Two-elements Windkessel model parameters		
Parameter		Value
C (arterial compliance)		$4.5 \cdot 10^{-9} m^3/Pa$
R (peripheral resistance)		$[2.5 \cdot 10^7, 4.5 \cdot 10^7] Pa \cdot s/m^3$

Table A.4: Blood circulation closed-loop parameters and thresholds

List of Figures

List of Tables